2-1-2012

Integrated cellular systems

Jason Carl Harper

Jason C. Harper
Candidate

Department of Chemical & Nuclear Engineering
Department

This dissertation is approved, and it is acceptable in quality and form for publication:

Approved by the Dissertation Committee:

Dr. C. Jeffrey Brinker, Chairperson

Dr. Susan M. Brozik

Dr. Gabriel P. Lopez

Dr. Margaret Werner-Washburne

Dr. Plamen Atanassov

INTEGRATED CELLULAR SYSTEMS

BY

JASON C. HARPER

B.S., Chemical Engineering, New Mexico Institute of Mining and Technology, 2002
M.S., Chemical Engineering, Purdue University, 2004

DISSERTATION

Submitted in Partial Fulfillment of the
Requirements for the Degree of

Doctor of Philosophy
Engineering

The University of New Mexico
Albuquerque, New Mexico

December, 2011

ACKNOWLEDGMENTS

I sincerely thank my advisors, C. Jeffrey Brinker and Susan M. Brozik, and the members of my dissertation committee, Gabriel P. Lopez, Margaret Werner-Washburne and Plamen Atanassov for their time, guidance, and encouragement.

Contributions to this work by Constantine Y. Khripin, Bryan Kaehr, Thayne L. Edwards, Eric C. Carnes, Carlee E. Ashley, DeAnna M. Lopez, Travis Savage, Elizabeth C. Larkin, Megan K. Economides, Sarah K. McIntyre, Todd M. Alam, Michaelann S. Tartis, Howland D. T. Jones, Ryan W. Davis, Dominique E. Nunez, Lina M. Brinker, Juewen Liu, Seema Singh, Margaret Werner-Washburne, David R. Wheeler, Susan M. Brozik, and C. Jeffrey Brinker are all deeply appreciated.

Funding for this work from the Defense Treat Reduction Agency (DTRA) Chemical and Biological Basic Research Program (grant B084467I) and the Sandia National Laboratories Lab Directed Research and Development (LDRD) Program are gratefully acknowledged.

INTEGRATED CELLULAR SYSTEMS

Jason C. Harper

B.S., Chemical Engineering, New Mexico Institute of Mining and Technology, 2002
M.S., Chemical Engineering, Purdue University, 2004
PH.D., Engineering, University of New Mexico, 2011

ABSTRACT

The generation of new three-dimensional (3D) matrices that enable integration of biomolecular components and whole cells into device architectures, without adversely altering their morphology or activity, continues to be an expanding and challenging field of research. This research is driven by the promise that encapsulated biomolecules and cells can significantly impact areas as diverse as biocatalysis, controlled delivery of therapeutics, environmental and industrial process monitoring, early warning of warfare agents, bioelectronics, photonics, smart prosthetics, advanced physiological sensors, portable medical diagnostic devices, and tissue/organ replacement.

This work focuses on the development of a fundamental understanding of the biochemical and nanomaterial mechanisms that govern the cell directed assembly and integration process. It was shown that this integration process relies on the ability of cells to actively develop a pH gradient in response to evaporation induced osmotic stress, which catalyzes silica condensation within a thin 3D volume surrounding the cells,

creating a functional bio/nano interface. The mechanism responsible for introducing functional foreign membrane-bound proteins *via* proteoliposome addition to the silica-lipid-cell matrix was also determined. Utilizing this new understanding, 3D cellular immobilization capabilities were extended using sol-gel matrices endowed with glycerol, trehalose, and media components. The effects of these additives, and the metabolic phase of encapsulated *S. cerivisiase* cells, on long-term viability and the rate of inducible gene expression was studied. This enabled the entrapment of cells within a novel microfluidic platform capable of simultaneous colorimetric, fluorescent, and electrochemical detection of a single analyte, significantly improving confidence in the biosensor output. As a complementary approach, multiphoton protein lithography was utilized to engineer 3D protein matrices in which to integrate cells and direct their behaviors. This process permits, for the first time, the selection and *in situ* isolation of a single target cell from a population of cells with mixed phenotypes, and the subsequent monitoring of its behavior, and that of its progeny, under well defined conditions.

These techniques promise a new means to integrate biomolecules with nanostructures and macroscale systems, and to manipulate cellular behavior at the individual cell level, having significant implications towards development of practical and robust integrated cellular systems.

TABLE OF CONTENTS

INTRODUCTION…….**1**

CHAPTER 1: Cell-Directed Integration into 3D Lipid-Silica Nanostructured Matrices……**12**

CHAPTER 2: Cell-Directed Localization and Orientation of a Functional Foreign Transmembrane Protein within a Silica Nanostructure……**57**

CHAPTER 3: Encapsulation of *S. cerevisiae* in Poly(glycerol) Silicate Derived Matrices: Effect of Matrix Additives and Cell Metabolic Phase on Long–Term Viability and Rate of Gene Expression...…….……**75**

CHAPTER 4: Orthogonal Cell-Based Biosensing: Fluorescent, Electrochemical, and Colorimetric Detection from Silica Matrix Encapsulated Cells in an ITO/Plastic Laminate Cartridge.…….……**117**

CHAPTER 5: Biocompatible Microfabrication for Targeted Confinement of Single Cells and Their Progeny..…….**146**

SUMMARY AND FUTURE OUTLOOK...……**172**

INTRODUCTION

Defense of the warfighter and personnel in structures against hazardous agents remains a significant challenge. Despite significant progress made in the last two decades towards portable and robust detection systems, biological detection devices face major limitations. They still require multiple reagents, have high power consumption, require significant skill to use, and are not yet available as handheld devices.[1] As most portable devices perform DNA or antibody-based assays for detection, the sensor may fail to detect near-neighbor or unknown agents for which the detector is not specifically designed. Further, these devices are incapable of real-time detection due to the requirement of subsequent washing and labeling steps.

Living cell–based sensors, often described as the equivalent of canaries used to detect toxic gases in mines,[2] have proven effective in addressing the latter two important issues. Cell lines have been engineered to respond to stress, toxicity, DNA damage, or death by rapidly producing, or decreasing production of bioluminescent, fluorescent, or electrochemical molecules, thereby providing real-time detection with built-in amplification.[3-5] A specific example is the development of the CANARY cell line by Lincoln Labs at MIT. Lymphocyte B-cells were engineered to produce a bioluminescent signal *via* a calcium-sensitive bioluminescent protein within seconds of pathogen binding to membrane-bound antibodies.[6] However, this and similar living cell–based sensors require frequent replenishment with new cells (every two days for CANARY) due to the sensitivity of the cells to their *ex-vivo* environment. This requirement has limited the use

of these more widely applicable sensors to high priority buildings in developed and stable regions.

To be practical for the warfighter, and for defense of structures in less developed regions, cell-based sensors require a biocompatible interface between the living cells and the macro world. Specifically, cells require a functional bio-inorganic interface that can interact at the nanoscale while maintaining cell viability. This encapsulating matrix must protect the cells from mechanical and chemical stresses, provide access to oxygen, nutrients, and molecules of interest, and allow the expulsion of metabolic wastes.[7]

Biomolecule Stabilization: Hybrid Living Materials

The generation of novel matrices that can encapsulate biomolecules without adversely altering their morphology or activity continues to be a bourgeoning and challenging field of research.[8-12] This research is driven by the promise that hybrid living materials can significantly impact areas as diverse as biocatalysis, controlled delivery of therapeutics, environmental and industrial process monitoring, early warning of warfare agents, bioelectronics, and tissue/organ replacement.[13-17] Numerous researchers have reported the generation of novel hybrid living materials that confer protection to the encapsulated cells, enhance long-term viability, and provide control over bio/nano interfacial properties and the environment local to the cells.[10,12,18-22] Such control can provide an instructive background needed to achieve specific functionalities and guide cellular behavior.[23-27]

The overwhelming majority of cell encapsulation studies have utilized the naturally occurring polysaccharide, sodium alginate, as the immobilization matrix.[7,28,29]

These generally interconnected microporous (~100 μm diameter) systems act as external cellular matrices allowing cells to divide and grow. Although useful for tissue and organ replacement or regeneration, these systems are less ideal for sensing applications due to the difficulty of monitoring and transducing information regarding the state of the encapsulated cells. They also suffer from biodegradation, and low stability in calcium poor solutions and in the presence of calcium chelates.[30,31] Addition of a polycation layer, typically poly-L-lysine (PLL), has been shown to increase alginate stability. However, PLL is toxic towards various cell lines, and is known to activate interleukin-1 production in macrophages and induce fibrosis.[32-34]

Silica Matrices for Cellular Encapsulation

Encapsulation of cells in inorganic materials has also been of interest as these structures are typically bioinactive and more easily tailored to provide desired material and chemical properties. Silica materials have been successfully employed for cellular encapsulation, beginning with the pioneering work of Carturan who encapsulated *Saccharomyces cerivisiase* (*S. cerivisiase*) in a tetraethylorthosilicate (TEOS) derived silica gel.[35] Advantages of silica for entrapment of biomolecules include the ability of sol-gel systems to retain water with negligible swelling, chemical and biological inertness, mechanical stability, controlled porosity, resistance to microbial attack, room temperature processing, optical transparency, and the ability to tailor the matrix to provide desired material and chemical properties.[16,36] Indeed, silica is an ideal cell-protectant in nature. Diatoms, radiolarians, and sponges have evolved to fix silica onto

their cell surfaces, forming silicon exoskeletons which can provide mechanical protection without adversely effecting nutrient and waste exchange required for growth.[37]

Initial attempts to immobilize living cells in sol-gel host matrices encountered barriers resulting in cytotoxicity during processing. Typically, the synthetic protocol consists of adding cells in buffer to acidic silicate sols formed by the acid-catalyzed hydrolysis of TEOS, or tetramethyl orthosilicate (TMOS), or ion exchange of sodium silicate. Buffered to physiological pH, gelation occurs rapidly, entrapping the cells within a randomly structured 3D siloxane matrix maintained in buffer to avoid drying. As gelation results in only a minor change in chemical composition and no dimensional change at the gel point, it was anticipated that there would be no detrimental effect on the encapsulated cells. However, monolithic biocomposites were limited by low porosity and poor structural integrity of the host matrix, inactivation of guest biological species through pore collapse, dehydration of the cells, low reproducibility, and cell leakage.[38-42]

These issues arise from material characteristics inherent to sol-gel processing. At neutral pH and without evaporation, the gel syneresis rate is maximized, leading to continued siloxane condensation reactions that in turn cause gel contraction and expulsion of pore fluid. Associated compressive stresses are presumably imposed on the entrapped cells. Drying further reduces the viability of cells immobilized within sol-gel matrices.[43-45] Evaporation causes the development of tensile capillary stresses in the pore fluid and concomitant shrinkage of the gel. Such drying stresses can range from a few to over a hundred MPa and are observed to damage the cell/gel interface, cause cell lysis, and result in rapid cell death. Finally, differential molecular and ionic diffusion through the contracting gel, which acts as a semi-permeable membrane, may result in the

development of localized osmotic stresses. These factors, combined with the possible presence of alcohol solvent or by-products, and contact of the cell membrane with polar chemical groups at the silica matrix surface (i.e. silanols), have a negative effect on cell viability. For example, in studies of *Escherichia coli* (*E. coli*) immobilization, Livage and coworkers observed a 40% reduction in viability within an hour after gelation—even under conditions where alcohol was avoided and the system pH, ionic strength, and temperature were optimal.[43]

Advances in Sol-Gel Processing and Cellular Encapsulation

Recent successes reported for sol-gel matrix encapsulated living cells address these issues by reducing the contact time between cells and the sol-gel precursor solution,[46,47] incorporating ameliorants (i.e. gelatin, polyvinyl alcohol, glycersol) into the silica gel,[43,45,48] developing silicates with non-cytotoxic hydrolysis and condensation byproducts (i.e. poly(glyceryl) silicate),[49] utilizing alternative precursors such as sodium silicate or colloidal silica,[44,50,51] depositing thin silica films over cells via exposure to gas phase silica alkoxides,[15,52,53] or stabilization of supramolecular assemblies and biological materials in silica thin films by chemical vapor deposition.[54,55]

Exploiting these advances, the high chemical and biological stability, and excellent transparency inherent to sol-gel derived silica materials, effective silica matrix entrapped whole cell-based biosensors have been reported. For example, Premkumar *et al*.[56,57] encapsulated *E. coli* strains engineered to respond to general toxicity, genotoxicity, and oxidative stress, in TMOS derived silicate films. Exposure to various toxins was monitored by production of an exogenous bioluminescence. Production of

fluorescent proteins by silica entrapped *E. coli* has also been employed for sensing,[58] and a careful study of the advantages/disadvantages of both luminescent and fluorescent systems has been reported.[59] Silica entrapped living cell-based sensors for biochemical oxygen demand (BOD),[60] naphthalene and salicylate,[61] anti-photo system II herbicides,[62] organophosphates,[63] dicyclopropyl ketone,[64] and other physiological stresses[65,66] have been reported.

Despite these many successes, long-term viability and activity remains a significant obstacle in producing practical and robust living cell-based hybrid composite materials. Herein we describe alternative approaches for developing integrated cellular systems. These approaches initially focus on recently reported work from the Brinker lab detailing a unique cell-directed assembly process that allows integration of living cells into nominally solid-state 3D devices.[22] Interestingly, it was found that cells actively organize around themselves a unique bio/nano interface comprised of a multilayered lipid membrane that interfaces coherently with the 3D lipid-templated silica matrix while maintaining accessibility of the encapsulated cells to the external environment and molecules introduced into the 3D silica host.[67]

Statement of Work

The work presented within this dissertation focuses on determining a fundamental understanding of the biochemical and nanomaterial mechanisms which govern the cell directed assembly and integration process. We show that this integration process selects exclusively for living cells over the corresponding apoptotic cells *via* the development of a pH gradient, which leads to cell-catalyzed silica deposition in close proximity to the

cell surface, resulting in the formation of a coherent interface between the cell and the surrounding silica matrix. We also demonstrate the introduction of multiple functional components to this system, including foreign membrane-bound proteins *via* proteoliposome addition, and propose a mechanism responsible for these observations.

Utilizing this new understanding, we extended our 3D cellular immobilization capabilities using sol-gel matrices endowed with glycerol, trehalose, and various media components. The effects of these additives, and the metabolic phase of silica matrix encapsulated *S. cerivisiase* cells, on long-term viability and the rate of inducible gene expression was carefully studied. This has enabled the entrapment and stabilization of more fragile and relevant cell lines for chemical and biological agent detection. Silica matrix thin film entrapment of 'Riboswitch' *E. coli* cells from our collaborators at the U.S. Air Force Research Laboratories[68] and yellow fluorescent protein (YFP) expressing *S. cerevisiae* cells, within a novel microfluidic platform prepared from plastic laminates machined by laser ablation allowed for simultaneous orthogonal mode biodetection *via* colorimetric, fluorescent, and electrochemical means, significantly improving confidence in the output of the living cell-based biosensor.

In parallel we have utilized multiphoton protein lithography as a complementary approach to engineer three-dimensional matrices in which to integrate cells and direct their behaviors. We demonstrate the selection of a single target cell followed by its *in situ* isolation in a porous 3D protein microchamber. This process permits, for the first time, the selection and isolation of a target cell (+ phenotype) from a population of cells with mixed phenotypes, and the subsequent monitoring of its behavior, and that of its progeny,

under well defined conditions. We further show the ability to impact cell growth and cell-to-cell signaling by tuning the physical properties of the protein microchamber.

These techniques promise a new means to integrate biomolecules with nanostructures and macroscale systems and manipulate cellular behavior at the individual cell level. These integrated cellular systems have implications towards development of bioelectronics, photonics, microfluidics, smart prosthetics, advanced physiological sensors, portable medical diagnostic devices, platforms for fundamental cell studies, and the development of practical and robust devices that can sense the presence of harmful agents in real-time.

References

1. Teles, F. S. R. R.; Tavira, L. A. P. de T.; de Fonseca, L. J. P. *Crit. Rev. Clin. Lab. Sci.* **2010,** *47*, 139-169.
2. Stenger, D. A.; Gross, G. W.; Keefer, E. W.; Shaffer, K. M.; Andreadis, J. D.; Ma, W.; Pancrazio, J. J. *Trends Biotech.* **2001**, *19*, 304-309.
3. Lei, Y.; Chen, W.; Mulchandani, A., *Anal. Chem. Acta* **2006**, *568*, 200-210.
4. Baeumner, A. J., *Anal. Bioanal. Chem.* **2003**, *377*, 434-445.
5. Kohler, S.; Belkin, S.; Schmid, R. D., *Fresenius J. Anal. Chem.* **2000**, *366*, 769-779.
6. Rider, T. H.; Petrovick, M. S.; Nargi, F. E.; Harper, J. D.; Schwoebel, E. D.; Mathews, R. H.; Blanchard, D. J.; Bortolin, L. T.; Young, A. M.; Chen, J.; Hollis, M. A. *Science* **2003**, *301*, 213-215.
7. Murua, A.; Portero, A.; Orive, G.; Hernández, R. M.; de Castro, M.; Pedraz, J. L. *J. Control. Release* **2008**, *132*, 76-83.
8. Kandimalla, V. B.; Tripathi, V. S.; Ju, H. *Crit. Rev. Anal. Chem.* **2006,** *36*, 73-106.
9. Salaita, K.; Wang, Y.; Mirkin, C. A. *Nat. Nanotech.* **2007**, *2*, 145-155.
10. Dave, B. C.; Dunn, B.; Valentine, J. S.; Zink, J. I. *Anal. Chem.* **1994**, *66*, 1120A-1127A.
11. Carballeria, J. D.; Quezada, M. A.; Hoyos, P.; Simeó, Y.; Hernaiz, M. J.; Alcantara, A. R.; Sinisterra, J. V. *Biotechnol. Adv.* **2009**, *27*, 686-714.
12. Yap, F. L.; Zhang, Y. *Biosens. Bioelectron.* **2007**, *22*, 775-788.
13. Ispas, C.; Sokolov, I.; Andreescu, S. *Anal. Bioanal. Chem.* **2009**, *393*, 543-554.
14. Gupta, R.; Chaudhury, N. K. *Biosens. Bioelectron.* **2007**, *22*, 2387-2399.
15. Carturan, G.; Toso, R. B.; Boninsegna, S.; Monte, R. D. *J. Mater. Chem.* **2004**, *14*, 2087-2098.
16. Ellerby, L. M.; Nishida, C. R.; Nishida, F.; Yamanaka, S.; Dunn, B.; Valentine, J. S.; Zink, J. I. *Science* **1992**, *255*, 1113-1115.
17. Meunier, C. F.; Rooke, J. C.; Leonard, A.; Xie, H.; Su, B. L. *Chem. Commun.* **2010,** *46*, 3843-3859.
18. Coradin, T.; Livage, J. *Acc. Chem. Res.* **2007,** *40*, 819-826.
19. Harper, J. C.; Khirpin, C. Y.; Carnes, E. C.; Ashley, C. E.; Lopez, D. M.; Savage, T.; Jones, H. D. T.; Davis, R. W.; Nunez, D. E.; Brinker, L. M.; Kaehr, B.; Brozik, S. M.; Brinker, C. J. *ACS Nano* **2010**, *4*, 5539-5550.
20. Bjerketorp, J.; Hakansson, S.; Belkin, S.; Jansson, J. K. *Curr. Opin. Biotech.* **2006,** *17*, 43-49.
21. Meunier, C. F.; Dandoy, P.; Su, B. L. *J. Colloid Interf. Sci.* **2010,** *342*, 211-224.
22. Baca, H. K.; Ashley, C.; Carnes, E.; Lopez, D.; Flemming, J.; Dunphy, D.; Singh, S.; Chen, Z.; Liu, N. G.; Fan, H. Y.; Lopez, G. P.; Brozik, S. M.; Werner-Washburne, M.; Brinker, C. J. *Science* **2006,** *313*, 337-341.
23. Carnes, E. C.; Harper, J. C.; Ashley, C. E.; Lopez, D. M.; Brinker, L. M.; Liu, J. W.; Singh, S.; Brozik, S. M.; Brinker, C. J. *J. Am. Chem. Soc.* **2009,** *131*, 14255-14257.
24. Carnes, E. C.; Lopez, D. M.; Donegan, N. P.; Cheung, A.; Gresham, H.; Timmins, G. S.; Brinker, C. J. *Nat. Chem. Biol.* **2010,** *6*, 41-45.
25. Raghavan, S.; Chen, C. S. *Adv. Mater.* **2004,** *16*, 1303-1313.
26. Stevens, M. M.; George, J. H. *Science* **2005,** *310*, 1135-1138.
27. Zhang, S. G. *Nat. Biotech.* **2004,** *22*, 151-152.
28. Mann, B. K.; West J. L. *Anat. Rec.* **2001**, *263*, 367-371.

29. Shea, L. D.; Wang, D.; Franceschi, R. T.; Mooney, D. J. *Tissue Eng.* **2000,** *6*, 605-617.
30. Premkumar, J. R.; Sagi, E.; Rozen, R.; Belkin, S.; Modestov, A. D.; Lev, O. *Chem. Mater*. **2002**, *14*, 2676-2686.
31. Rokstad, A. M.; Donati, I.; Borgogna, M.; Oberholzer, J.; Strand, B. L.; Espevik, T.; Skjåk-Bræk, G. *Biomater*. **2006**, *27*, 4726-4737.
32. Strand, B. L.; Ryan, L.; Veld, P. I.; Kulseng, B.; Rokstad, A. M.; Skjåk-Bræk, G.; Espevik, T. *Cell Transplant* **2001**, *10*, 263-275.
33. Darquy, S.; Pueyo, M. E.; Capron, F.; Reach, G. *Artif. Organs* **1994**, *18*, 898-903.
34. Pueyo, M. E.; Darguy, S.; Capron, F.; Reach, G. *J. Biometer. Sci. Polym. Ed.* **1993**, *5*, 197-203.
35. Carturan, G.; Campostrini, R.; Dirè, S.; Scardi, V.; de Alteriis, E. *J. Mol. Catal.* **1989**, *57*, L13-L16.
36. Avnir, D.; Coradin, T.; Lev, O.; Livage, J. *J. Mater. Chem.* **2006**, *16*, 1013-1030.
37. Hamm, C. E.; Merkel, R.; Springer, O.; Jurkojc, P.; Maier, C.; Prechtel, K.; Smetacek, V. *Nature* **2003,** *421*, 841-843.
38. Bousse, L., *Sensor Actuat. B-Chem.* **1996**, *34*, 270-275.
39. Ziegler, C., *Fresen. J. Anal. Chem.* **2000,** *366*, 552-559.
40. Curtis, A.; Wilkinson, C., *Biomaterials* **1997**, *18*, 1573-1583.
41. Koh, W. G.; Revzin, A.; Pishko, M. V., *Langmuir* **2002**, *18*, 2459-2462.
42. Assender, H.; Bliznyuk, V.; Porfyrakis, K., *Science* **2002**, *297*, 973-976.
43. Nassif, N.; Roux, C.; Coradin, T.; Rager, M. N.; Bouvet, O. M. M.; Livage, J. A. *J. Mater. Chem.* **2003**, *13*, 203-208.
44. Coiffier, A.; Coradin, T.; Roux, C.; Bouvet, O. M. M.; Livage, J. *J. Mater. Chem.* **2001**, *11*, 2039-2044.
45. Nassif, N.; Bouvet, O.; Rager, M. N.; Roux, C.; Coradin, T.; Livage, J. *Nat. Mater*. **2002**, *1*, 42-44.
46. Pope, E. J. A.; Braun, K.; Peterson, C. M. *J. Sol-Gel Sci. Technol.* **1997**, *8*, 635-639.
47. Chia, S.; Urano, J.; Tamanoi, F.; Dunn, B.; Zink, J. I. *J. Am. Chem. Soc.* **2000**, *122*, 6488-6489.
48. Conroy, J. F. T.; Power, M. E.; Martin, J.; Earp, B.; Hosticka, B.; Daitch, C. E.; Norris, P. M. *J. Sol-Gel. Sci. Technol.* **2000**, *18*, 269-283.
49. Gill, I.; Ballesteros, A. *J. Am. Chem. Soc.* **1998**, *120*, 8587-8598.
50. Yu, D.; Volponi, J.; Chhabra, S.; Brinker, C. J.; Mulchandani, A.; Singh, A. K. *Biosens. Bioelection.* **2005**, *20*, 1433-1437.
51. Finnie, K. S.; Bartlett, J. R.; Woolfrey, J. L. *J. Mater. Chem.* **2000**, *10*, 1099-1101.
52. Campostrini, R.; Carturan, G.; Caniato, R.; Piovan, R.; Filippini, G.; Innocenti, G.; Cappelletti, E. M. Immobilization *J. Sol-Gel Sci. Technol.* **1996**, *7*, 87-97.
53. Muraca, M.; Vilei, M. T.; Zanusso, G. E.; Ferraresso, C.; Boninsegna, S.; Monte, R. D.; Carraro, P.; Carturan, G. *Artif. Organs* **2002**, *26*, 664-669.
54. Gupta, G.; Rathod, S. B.; Staggs, K. W.; Ista, L. K.; Oucherif, K. A.; Atanassov, P. B.; Tartis, M. S.; Montaño, G. A.; López, G. P. *Langmuir* **2009**, *25*, 13322-13327.
55. Gupta, G.; Atanassov, P.; López, G. P. *Biointerphases* **2006**, *1*, 6-10.
56. Premkumar, J. R.; Lev, O.; Rosen, R.; Belkin, S. *Adv. Mater.* **2001,** *13*, 1773-1775.
57. Premkumar, J. R.; Rosen, R.; Belkin, S.; Lev, O. *Anal. Chim. Acta* **2002,** *462*, 11-23.

58. Premkumar, J. R.; Sagi, E.; Rozen, R.; Belkin, S.; Modestov, A. D.; Lev, O. *Chem. Mater*. **2002,** *14*, 2676-2686.
59. Sagi, E.; Hever, N.; Rosen, R.; Bartolome, A. J.; Premkumar, J. R.; Ulber, R.; Lev, O.; Scheper, T.; Belkin, S. *Sens. Actuat. B-Chem.* **2003,** *90*, 2-8.
60. Jia, J. B.; Tang, M. Y.; Chen, X.; Li, Q.; Dong, S. J. *Biosens. Bioelectron.* **2003,** *18*, 1023-1029.
61. Trogl, J.; Ripp, S.; Kuncova, G.; Sayler, G. S.; Churava, A.; Parik, P.; Demnerova, K.; Halova, J.; Kubicova, L. *Sens. Actuat. B-Chem.* **2005,** *107*, 98-103.
62. Nguyen-Ngoc, H.; Tran-Minh, C. *Anal. Chim. Acta* **2007,** *583*, 161-165.
63. Yu, D.; Volponi, J.; Chhabra, S.; Brinker, C. J.; Mulchandani, A.; Singh, A. K. *Biosens. Bioelectron.* **2005,** *20*, 1433-1437.
64. Ferrer, M. L.; Yuste, L.; Rojo, F.; del Monte, F. *Chem. Mater.* **2003,** *15*, 3614-3618.
65. Perullini, M.; Jobbagy, M.; Moretti, M. B.; Garcia, S. C.; Bilmes, S. A. *Chem. Mater.* **2008,** *20*, 3015-3021.
66. Kuncova, G.; Podrazky, O.; Ripp, S.; Trogl, J.; Sayler, G. S.; Demnerova, K.; Vankova, R. *J. Sol-Gel Sci. Technol.* **2004,** *31*, 335-342.
67. Baca, H. K.; Carnes, E.; Singh, S.; Ashley, C.; Lopez, D.; Brinker, C. J. *Acc. Chem. Res.* **2007**, *40*, 836-845.
68. Harbaugh, S.; Kelley-Loughnane, N.; Davidson, M.; Narayana, L.; Trott, S.; Chushak, Y. G.; Stone, M. O. *Biomacromol.* **2009**, *10*, 1055-1060.

CHAPTER 1

Cell-Directed Integration into 3D Lipid-Silica Nanostructured Matrices

Harper, J. C., Khripin, C. Y. Carnes, E. C., Ashley, C. E,
Lopez, D. M., Savage, T., Jones, H. D. T., Davis, R. W., Nunez, D. E.,
Brinker, L. M., Kaehr, B., Brozik, S. M., Brinker, C. J.

ACN Nano **2010**, *4*, 5539-5550.

Abstract

We report a unique approach in which living cells direct their integration into 3D solid state nanostructures. Yeast cells deposited on a weakly condensed lipid/silica thin film mesophase actively reconstruct the surface to create a fully 3D bio/nano interface, composed of localized lipid bilayers enveloped by a lipid/silica mesophase, through a self-catalyzed silica condensation process. Remarkably, this integration process selects exclusively for living cells over the corresponding apoptotic cells (those undergoing programmed cell death), *via* the development of a pH gradient, which catalyzes silica deposition and the formation of a coherent interface between the cell and surrounding silica matrix. Added long chain lipids or auxiliary nanocomponents are localized within the pH gradient, allowing the development of complex active and accessible bio/nano interfaces not achievable by other synthetic methods. Overall this approach provides the first demonstration of active cell-directed integration into a nominally solid state three dimensional architecture. It promises a new means to integrate ‘bio’ with ‘nano’ into

platforms useful to study and manipulate cellular behavior at the individual cell level and to interface living organisms with electronics, photonics, and fluidics.

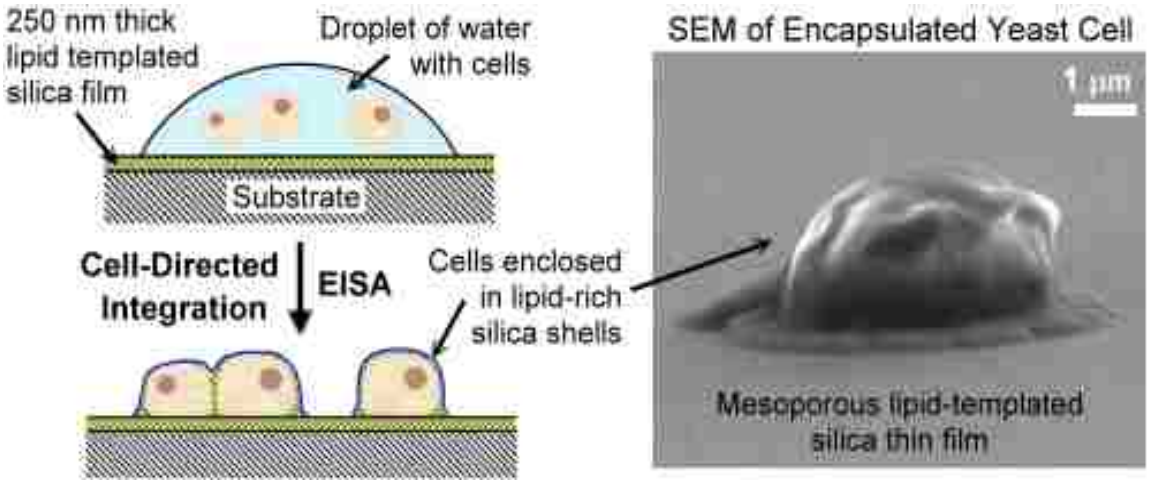

Abstract Figure 1

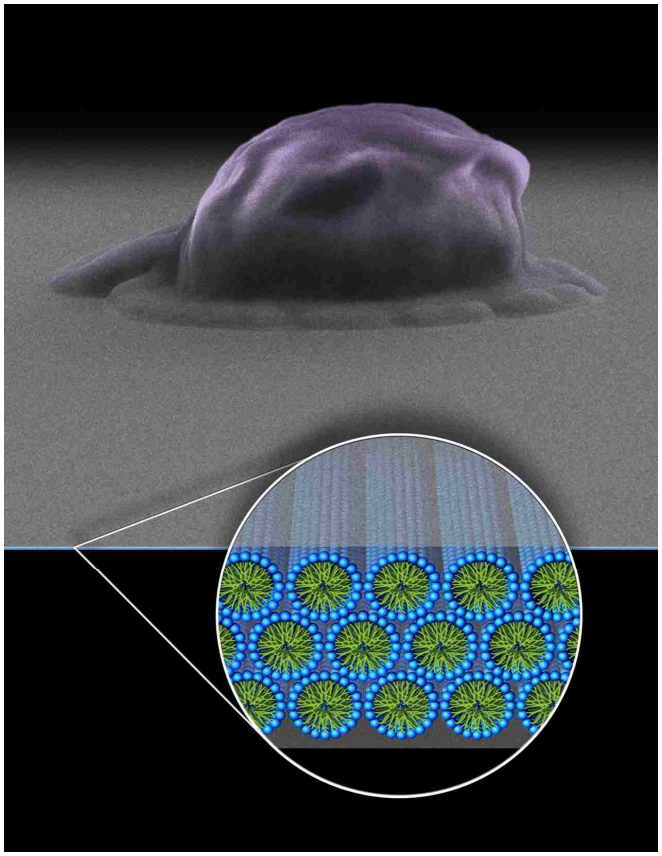

Abstract Figure 2

INTRODUCTION

The generation of new 3D matrices that enable integration of biomolecular components and whole cells into device architectures, without adversely altering their morphology or activity, continues to be an expanding and challenging field of research.[1-5] This research is driven by the promise that encapsulated biomolecules and cells can significantly impact areas as diverse as biocatalysis, controlled delivery of therapeutics, environmental and industrial process monitoring, early warning of warfare agents, bioelectronics, and tissue/organ replacement.[6-9] To date, extensive techniques have been developed for biomolecule encapsulation generally relying on adsorption, covalent binding, or entrapment of biomolecules in polymeric materials.[10] Successful strategies for protein and enzyme entrapment are widely reported; however, encapsulation of living cells is significantly more challenging.[11,12] This is due to the more stringent requirements for the encapsulation matrix which must provide a functional bio/nano interface between the cells and the macro environment, protecting the cells from mechanical and chemical stresses, providing access to oxygen, nutrients and target molecules of interest, and allowing for the expulsion of metabolic wastes.[13]

Silica matrices formed by sol-gel processing have been employed for cellular encapsulation beginning with the pioneering work of Carturan, who encapsulated *Saccharomyces cerivisiae* (*S. cerivisiae*) in a tetraethylorthosilicate (TEOS) derived silica gel.[14] Advantages of physical entrapment of biomolecules and cells within wet (water or buffer filled) silica gels include the ability of sol-gel systems to retain water with negligible swelling, biological inertness, mechanical stability, simple room temperature

processing, and 3D confinement within a matrix that maintains accessibility of the cell.[7,15] Traditional sol-gel processing techniques, however, can be cytotoxic to cells. Exposure to alcohol solvents and byproducts, contact with polar chemical groups at the silica surface (i.e. silanols), compressive stresses resulting from gel syneresis at neutral pH, and drying-induced tensile capillary stresses can damage the cell/gel interface, and induce cell lysis. Therefore, strategies have been developed to mitigate these issues including reducing the contact time between cells and the sol-gel precursor solution,[16,17] incorporating ameliorants (i.e. gelatin, polyvinyl alcohol, glycersol) into the silica gel,[18-20] developing silicates with non-cytotoxic hydrolysis and condensation byproducts (i.e. poly(glyceryl) silicate),[21] using all aqueous precursors such as sodium silicate or colloidal silica,[22-24] or depositing thin silica films over cells *via* exposure to gas phase silicon alkoxides.[8,25,26]

All of the sol-gel encapsulation strategies listed above result in the physical entrapment of cells with no evidence of cellular influence on the development of the matrix or bio/nano interface. As an alternative approach, we recently reported the cell-directed encapsulation of yeast and bacterial cells within a self-assembled biocompatible silica matrix.[27,28] Incorporation of short-chained phospholipids, in lieu of traditionally used surfactants which are cytotoxic to cells, during evaporation-induced self-assembly (EISA),[29] yielded an ordered silica mesophase within which incorporated cells actively organized a unique bio/nano interface and globally altered the matrix nanostructure. The bio/nano interface is composed of a multilayered lipid membrane that interfaces coherently with a 3D lipid-templated silica matrix, which provides accessibility of the encapsulated cells to molecules introduced into the 3D silica host.[28,30] Importantly, a

localized nanostructured microenvironment was created in which 3D chemical gradients were established. Such gradients can provide an instructive background needed to achieve proper functionality and guide cellular behavior.[31,32] Examples include cell-differentiation, biofilm formation, and quorum sensing, which all rely on the development of spatiotemporal gradients of signaling molecules.[30,33,34]

Herein we describe an extension of this original cell directed assembly approach in which introduction of cells onto a pre-formed lipid-templated silica film leads to partial dissolution of matrix components, and active cellular reconstruction of a 3D bio/nano interface composed of lipid-rich silica shells that interface the cells with the nanostructured inorganic matrix. Advantages to this new approach include (i) reduced stresses exerted on the cells due to avoidance of cellular contact with alcoholic solvents, byproducts, and catalysts, (ii) maintenance of the original nanostructure of the bulk film, providing greater control over the properties of host matrix, (iii) accessibility to the external environment *via* rapid transport through the thin film encapsulating the cells, (iv) improved optical accessibility through the thin film to interrogate the integrated cells, and (v) greater control over location of cells in the thin film. To our knowledge, this is the first example of active cell-directed integration into a nominally solid state three-dimensional architecture. This report focuses on the general properties of the encapsulation matrix and the fundamental nanomaterial and biochemical mechanisms that govern this self-integration process.

RESULTS AND DISCUSSION

The living cell directed integration process is depicted in Scheme 1. Upon introduction of an aqueous suspension of *S. cerevisiae* cells (*via* pipette or aerosol) onto a weakly condensed lipid-silica mesophase film, components of the film are solubilized by the droplet (Scheme 1a). Upon evaporation, gradients in temperature, concentration and viscosity lead to circulating Marangoni flows driven by surface-tension gradients. Fluorescent microscopy video imaging of initial droplet evaporation using fluorescently stained cells shows flow near the liquid-solid interface was driven towards the circumferential three phase boundary, while flow near the liquid-gas interface was directed radially toward the droplet center in a circulating fashion (Scheme 1a).[35-38] The three phase boundary was observed to de-pin immediately upon droplet deposition due to concentration of solubilized lipid, which presumably formed a Gibb's monolayer, while reducing the droplet surface tension (and contact angle) to below the receding angle value.

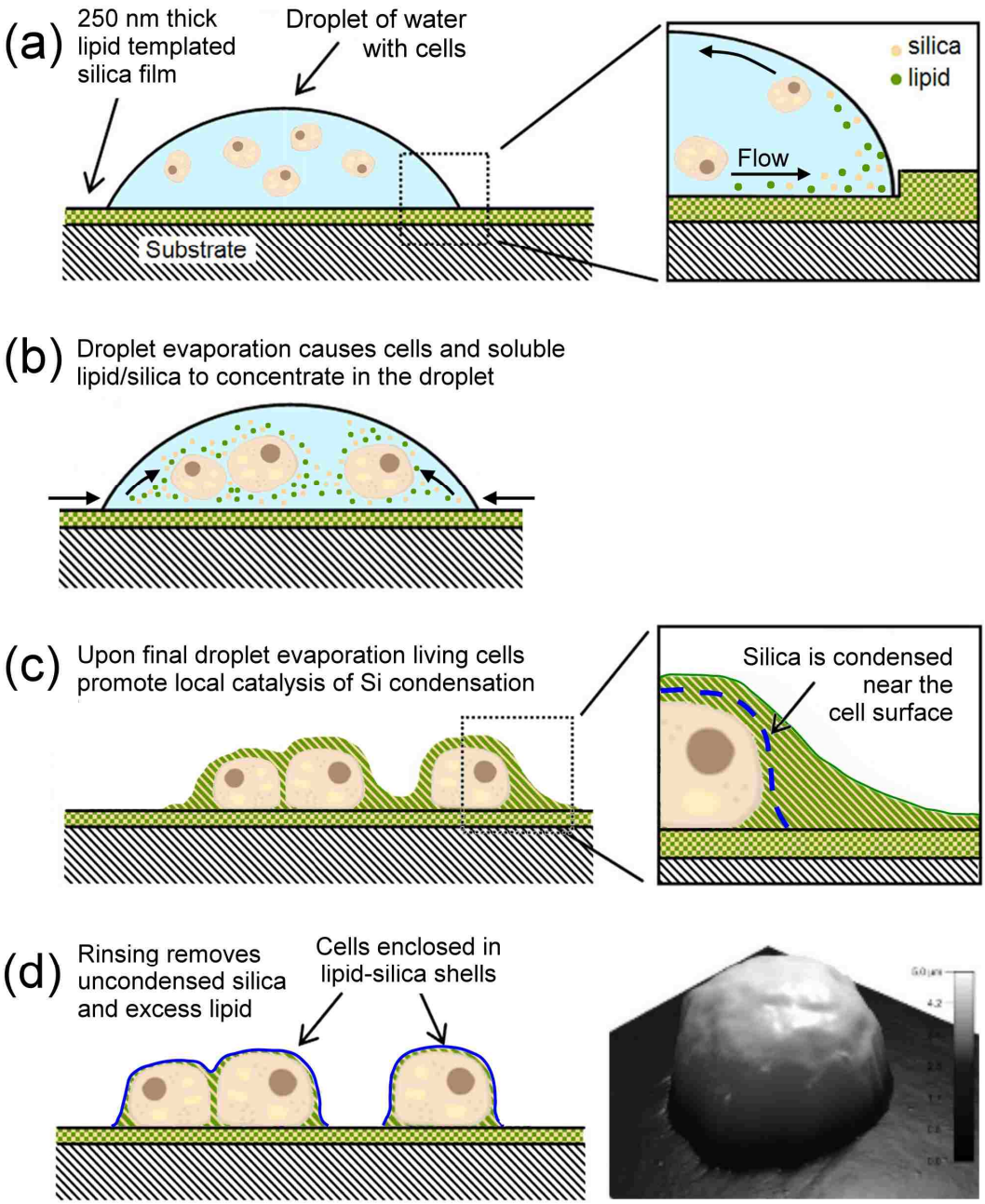

Scheme 1. Cell directed integration of microorganisms in pre-formed lipid-templated silica thin films occurs *via* (a) initial solubilization of the slowly condensing film components (lipid and silica) upon introduction of an aqueous suspension of cells. Droplet evaporation leads to capillary and Marangoni flow which concentrates cells and soluble components (b). Viable cells create a locally high pH catalyzing silica condensation and their self-integration into a 3D lipid silica nanostructure (c). Rinsing the substrate following droplet evaporation removes excess lipid and non-condensed silica yielding cells encapsulated in a lipid-rich silica shell (d). The inset image was generated *via* atomic force microscopy of a single *S. cerevisiae* cell encapsulated in a lipid-silica shell following substrate rinsing. Scale bar: 0 to 5 μm.

As evaporation proceeded, the three phase boundary continued to recede with decreased contact area and nearly constant contact angle, while cells, lipid, and soluble silica were progressively concentrated within the droplet (Scheme 1b). Upon final droplet evaporation, as the film thickness became commensurate with the cell diameter, the slowly receding three phase boundary was violently retracted by the meniscus curvature. This left clusters or single cells at the center of multiple droplets, containing high concentrations of lipid and soluble silica. Additionally, 'coffee-stain rings'[36,38] of cells, lipid, and silica were often produced at the retracted droplet periphery, far within the original droplet edge. At this stage, viable cells develop a localized three dimensional (3D) gradient in pH, catalyzing silica condensation, and their self-integration into a 3D lipid-silica nanostructure (Scheme 1c). Rinsing the substrate shortly after droplet evaporation removes uncondensed silica and lipid concentrate, leaving cells encapsulated in a coherent and conformal lipid-rich silica shell bound to the underlying film (Scheme 1d, and inset AFM image). In the following, we provide further detail and discussion of the successive stages of the cell integration process.

Lipid-Silica Matrix Solubilization and Reconstruction

Dissolution of lipid from the film following droplet introduction (Scheme 1a) was monitored by incorporation of 0.1% fluorescently labeled NBD-*di*C_6 PC lipid molecules (green emission) into the film, and observing the fluorescence intensity upon exposure to water. The fluorescence microscopy image shown in Figure 1A contains three regions of interest: (i) pristine film, (ii) an area exposed to a water droplet for 10 min (water droplet is present in Figure 1A), and (iii) a scratched area where the film was entirely removed.

Brief exposure of the weakly condensed lipid-silica film to the water droplet resulted in nearly complete loss of fluorescence intensity, as shown in region (ii). This loss of fluorescence is attributed to rapid lipid dissolution, and to a lesser extent, silica dissolution, which occurs more slowly and depends on film aging time (see following discussion). If left to evaporate, substantial fluorescence emission was recovered; however, in this case, the observed fluorescence in the water exposed and evaporated region was no longer homogenous. Restoration of fluorescence in this non-homogenous manner is characteristic of lipid and silica deposits following diffusion fronts during droplet evaporation. The solubility of the film components was further characterized by AFM imaging (Figure 1B) which shows film areas exposed to water are reduced in thickness during contact with water and subsequent drying of the drop. The film thickness decrease is attributed to silica dissolution along with possible capillary stress induced shrinkage or collapse of the mesoporous film during drying. In-situ AFM imaging (Figure 3C) shows that for films aged 30 min prior to introduction of water, the film thickness decreases upon water exposure, and further upon drying. The latter shrinkage is attributed to capillary stresses imposed during drying of the porous lipid-depleted film.

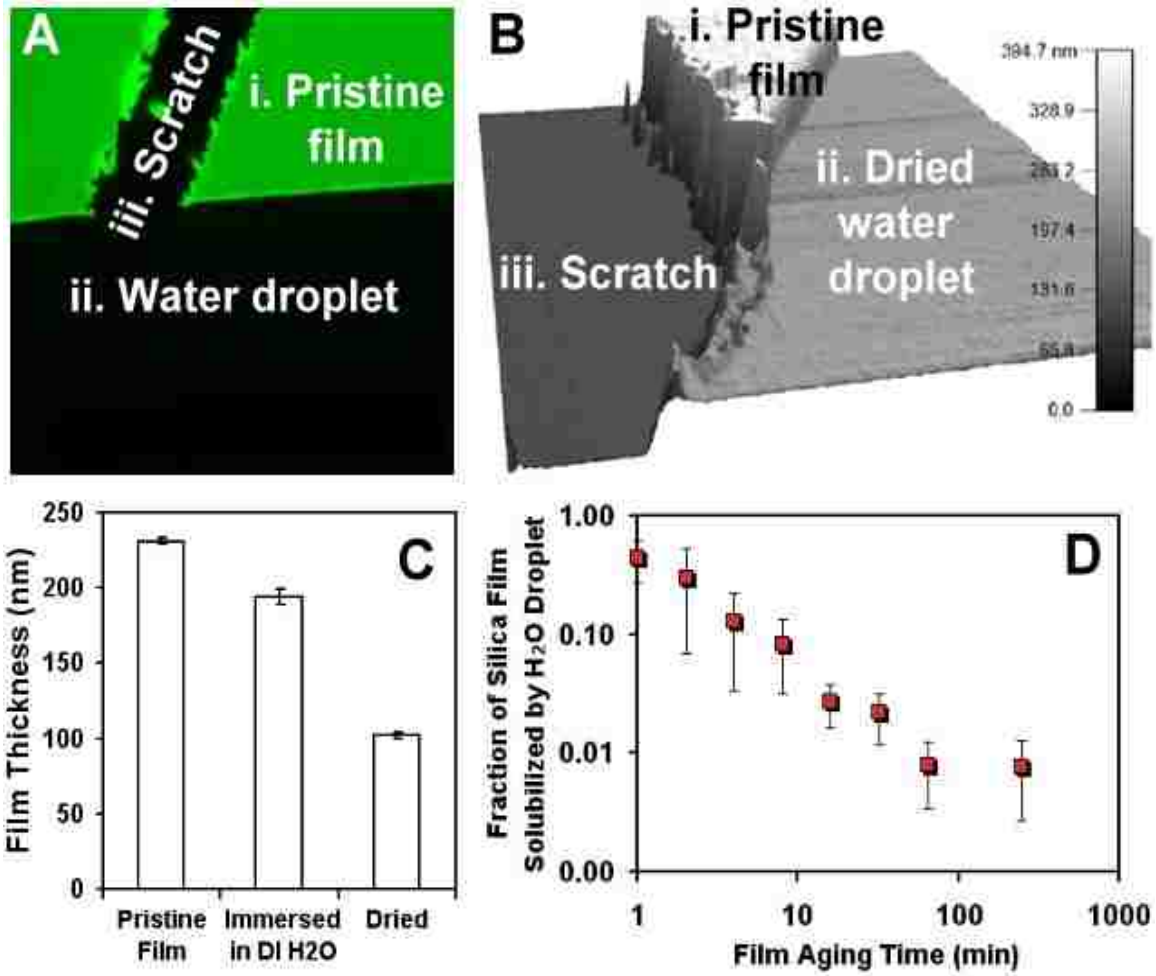

Figure 1. (A) Fluorescence microscopy image of a lipid-templated (0.1% NBD labeled *di*C_6 PC, green emission) mesoporous silica film (i), upon introduction of a 0.5 μL water droplet (ii), near a scratch (iii) to expose the underlying substrate. (B) AFM measurement of the region imaged in (A). Scale bar: 0 to 395 nm. (C) AFM measured thickness of lipid-templated mesoporous silica films under various conditions. (D) Fraction of silica film solubilized vs. age of the slowly condensing film as determined by molybdic acid assay.

Silica dissolution depends strongly on the aging time of the film, and thereby, its extent of condensation, prior to introduction of the water drop. This is shown in Figure 1D, which plots the fraction of the film solubilized (determined by the molybdic blue assay of soluble silica, see Experimental Methods) as a function of film aging time.

Between 10-45% of the total film silica can be solubilized if water is introduced to the film during the first 10 minutes following film formation. Dissolution of this substantial portion of silica had a detrimental affect on the film morphology and uniformity. The fraction of silica solubilized from the film continued to decrease with film age, stabilizing near 1% at 30 minutes following film formation. These observations indicate that silica precursors in the prepared films continue to condense over time, reducing solubility.[39,40] Films aged for at least 30 minutes were structurally stable, maintaining uniformity and nanostructure following introduction of water droplets. Based on these results, lipid-templated mesoporous silica films were aged between 30 and 120 minutes prior to the introducion of an aqueous suspensions of cells.

Grazing-incidence small-angle X-ray scattering (GISAXS) and scanning electron microscopy (SEM) were used to characterize the lipid-templated silica matrix. The GISAXS pattern in Figure 2A, obtained for the as-deposited film, is consistent with a hexagonally ordered lipid-silica mesophase composed of lipid-filled cylindrical pores ~2.3 nm in diameter, with repeat distances (d_y) of ~3.0 nm perpendicular to the substrate, and d_x of ~3.5 nm in the plane of the substrate. Figure 2B shows the GISAXS pattern recorded from a film in which yeast cells were introduced across the entire substrate *via* aerosol deposition. In contrast to our previous report in which cells and lipids were mixed directly with silica sols, resulting in a cell-directed hexagonal to lamellar phase transformation upon spin-coating,[27] the bulk hexagonal nanostructure of the pre-formed silica film was largely retained following introduction of the cells. This is not surprising as film dissolution and reorganization occurs only in the areas (~1% of total film area) exposed to the aerosol of the aqueous cell suspension. A slight loss of order of the

primary hexagonal structure in the GISAXS pattern was accompanied by the development of a minor lamellar structure, similar to that observed in our previous work.[27] This suggests that the matrix is reorganized to form a lamellar structure local to the encapsulated cells, while the nanostructure of the bulk film remains unchanged. We have previously shown that self-assembly of amphiphilic template molecules occurs in the aqueous phase.[41] In that work, we showed for systems initially formed from a binary solvent (water and alcohol), that the alcohol co-solvent evaporates in the first stage of EISA, leaving self-assembly in the final stages of EISA to occur under completely aqueous conditions. In the case of a purely aqueous droplet extracting lipid and silica from the film, we also expect EISA to yield an ordered nanostructure. The formation of a lamellar phase is consistent with the higher concentration of lipid in the aqueous droplet, versus the lipid concentration in the initial sol precursor solution.

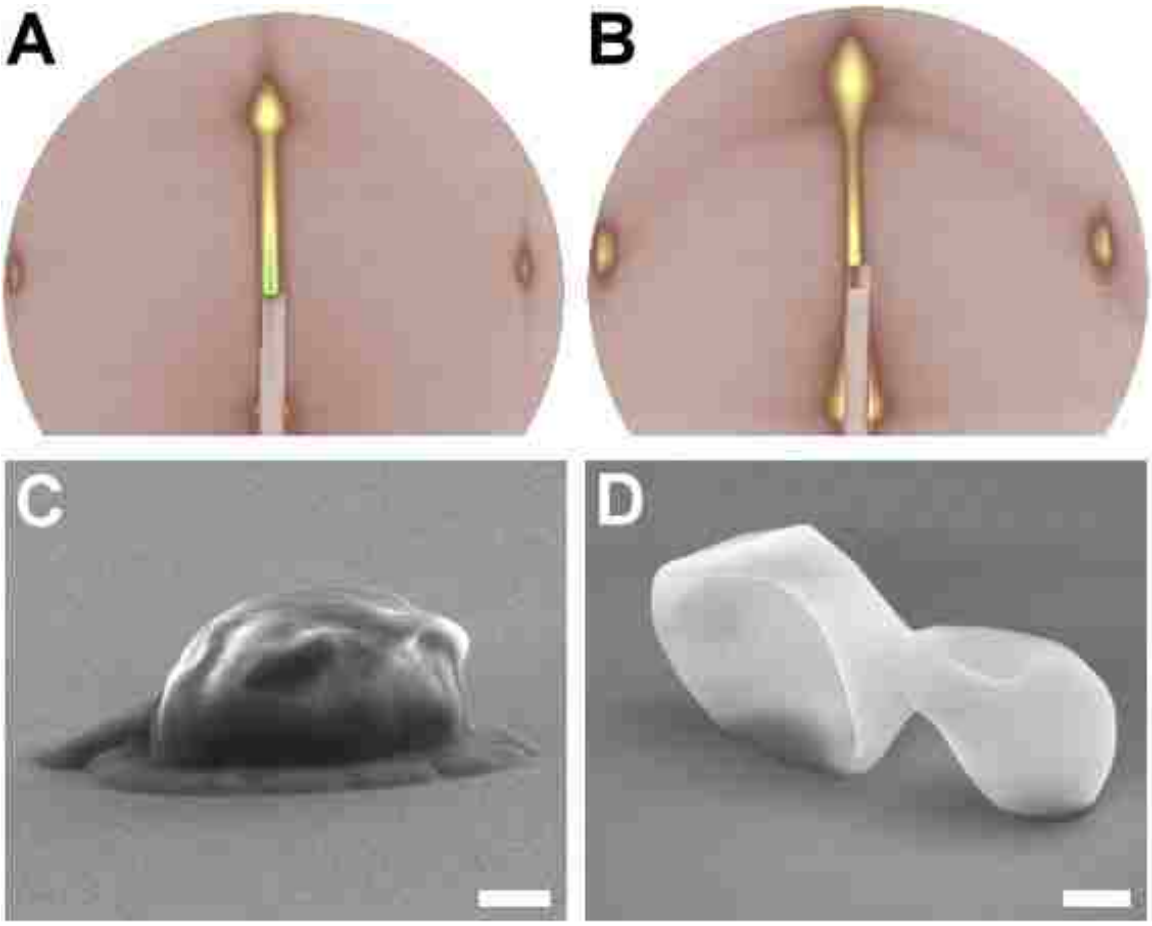

Figure 2. Grazing-incidence small-angle X-ray scattering (GISAXS) patterns of lipid-templated mesoporous silica films: (A) Pristine film, (B) film following self-encapsulation of *S. cerevisiae* cells. (C) SEM image of a single yeast cell encapsulated into the lipid-templated silica matrix. (D) SEM image of two yeast cells introduced to a clean silicon substrate without a lipid-templated mesoporous silica thin film. Scale bars = 1 μm.

SEM imaging was performed directly (without fixation or supercritical drying) on silicon substrates coated with lipid-templated silica films onto which *S. cerevisiae* cells were deposited *via* aerosol deposition, as in Figure 2B. Figure 2C shows a coherent interface between the integrated cell and the underlying (featureless) lipid silica thin film mesophase, and a smooth conformal coating overtop the cell. At the base of the

encapsulated cell, a raised region is observed corresponding to deposition of silica and lipid concentrate driven towards the cells during droplet evaporation, as described previously (Scheme 1c). Interestingly, the shape of integrated cells investigated using SEM appeared relatively spherical, indicating that the native morphology of the yeast cells, in large part, was retained during the encapsulation process. Additionally, the encapsulated cell morphology was maintained under continuous exposure to vacuum and electron beam irradiation over the course of SEM imaging (without any additional sample preparation). This is in contrast to SEM images of *S. cerevisiae* cells introduced onto bare silicon substrates without lipid-silica thin films. As shown in Figure 2D, cells appear non-adherent and exhibit signs of severe desiccation with significantly collapsed morphologies. Preservation of cell morphology through silica encapsulation bears some analogy to certain marine organisms (e.g. diatoms, radiolarians, and sponges) that fix silica on their cell surfaces forming an artificial exoskeleton, which can preserve cell morphology and function under harsh conditions.

3D Bio/Nano Interface

Hyperspectral confocal fluorescence microscopy was used to further characterize the three-dimensional structure of the lipid/silica encapsulated *S. cerevisiae* cells. For films prepared with the pH sensitive fluorescent probe, Oregon Green (OG), multivariate curve resolution (MCR) identified two independently varying spectral components corresponding to the *S. cerevisiae* cellular autofluorescence, and to OG fluorescence. Spectral components are presented in the supplemental information, Figure S1. Although the autofluorescence and OG components are highly overlapped, the hyperspectral

imaging technique can clearly separate the fluorophores and produce cross-talk free images of the location and intensity of the fluorophores within the images. Figure 3A shows RGB images at various confocal cross-sections (red corresponding to the autofluorescence, green corresponding to OG) of a cluster of three encapsulated *S. cerevisiae* cells. The intensity of OG fluorescent emission decreases as the pH is lowered from approximately pH 6 to 3 with total quenching of fluorescence at highly acidic pH (≤ 2). Consistent with our previous results,[27,28] encapsulated cells form a three-dimensional gradient in pH from approximately pH 3 in the acidic silanol-terminated thin film silica matrix, to pH 5.5 at the encapsulated cell surface. This gradient appears to be confined to the <1µm region of reconstructed lipid/silica surrounding the encapsulated cells. The concentration of *di*C_6 PC lipid in the bulk film and near encapsulated cells was also investigated using hyperspectral imaging. Figure 3B is a false-colored image depicting the concentration of *di*C_6 PC lipid near the base of a single yeast cell. The concentration of lipid surrounding the cell was determined by calibrating TAMRA fluorescence intensities obtained from the images of solutions with known TAMRA-*di*C_6 PC concentrations at the same microscope settings. Figure 3B shows that the total lipid concentration in the bulk film was 200-250 mg/mL. This is an approximate 10-fold increase in lipid concentration compared to the initial concentration in the sol precursor solution used to produce the film. This observation is consistent with the expected increase in concentration of sol precursor solution components during EISA. Also apparent is a gradient in lipid concentration showing localization of the lipid near the encapsulated cell. Similar to the observations with OG, this gradient in lipid concentration extends below and above the cells, but also extends much further into the

bulk film. We have previously shown that lipid accumulation at the cellular surface serves to interface encapsulated *S. cerevisiae* with the inorganic silica host matrix.[27,28] Further, as film nanostructure is driven by concentration dependent lipid self-assembly, we expect this lipid gradient region to correspond to the interface between the hexagonally structured bulk film and the lamellar structure encapsulating the cells. We are currently investigating the structure of this interface region.

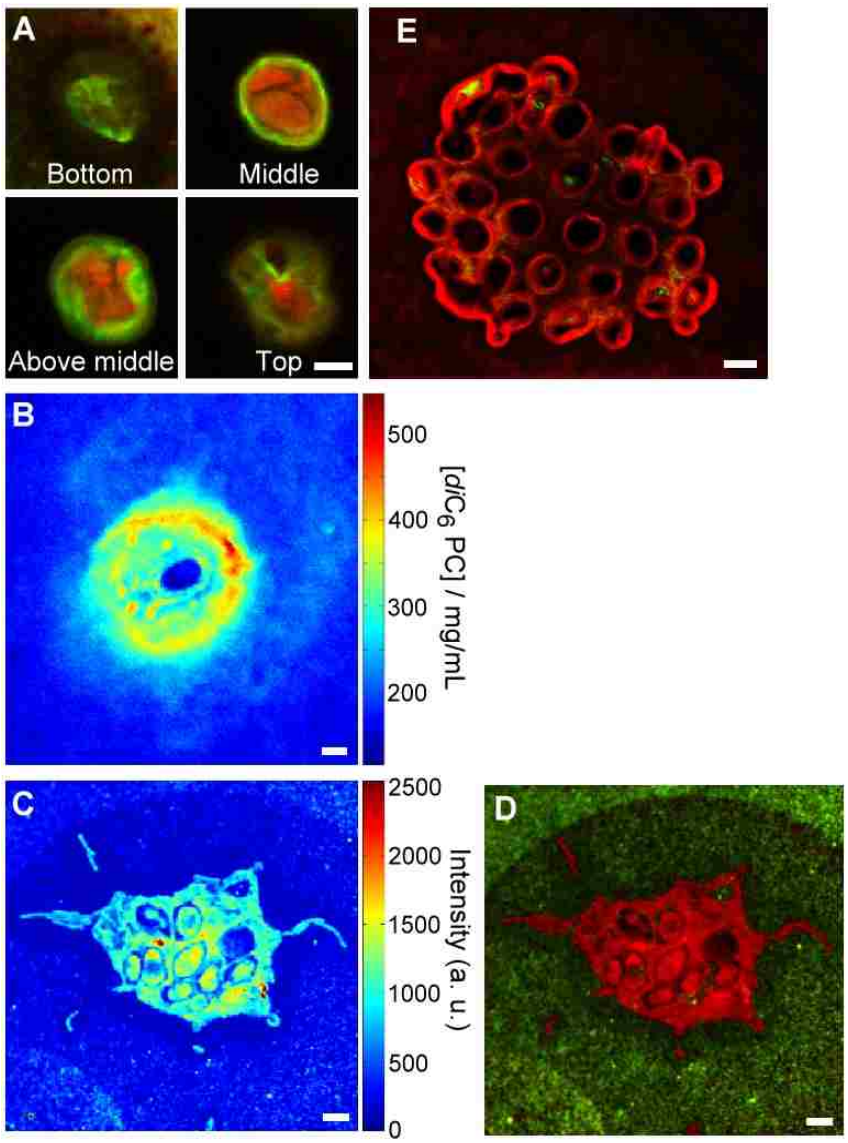

Figure 3. (A-D) False colored hyperspectral confocal fluorescence images of yeast cells encapsulated in lipid-silica matrices. (A) Confocal slices from a cluster of three *S. cerevisiae* cells (red) encapsulated in a *di*C_6 PC templated silica film containing the pH sensitive probe, Oregon Green (green). (B) Confocal slice near the base of a single yeast cell entrapped in a *di*C_6 PC templated silica film (TAMRA-*di*C_6 PC accounts for 0.1% of total lipid) showing localization of lipid near the cell. Color corresponds to lipid concentration, increasing from blue to red. (C) Confocal slice near the base of a cluster of *S. cerevisiae* cells encapsulated in a lipid-silica matrix containing 655 nm Qdots. Color corresponds to Qdot fluorescence intensity, increasing from blue to red. (D) Two distinct spectra from Qdots in the sample from panel (C) were identified: typical 655 nm Qdot spectrum (green), and Qdot spectrum red shifted by 7 nm (red). (E) Confocal florescence image showing conformal liposome fusion with yeast cells upon integration into the lipid-templated silica film. POPC liposomes (6% Texas Red-labeled DHPE) were introduced to the film with the yeast cell suspension. Scale bars = 3 μm.

The cell-directed integration process can also reorganize, three-dimensionally, nanoscale components introduced into the original lipid-silica thin film mesophase. Figure 3C and 3D show hyperspectral confocal images of a cluster of *S. cerevisiae* cells encapsulated within a film prepared with amino-derivatized polyethylene glycol coated quantum dots (655 nm emission). Figure 3C is a false-colored image depicting the fluorescence intensity of the quantum dots present in the lipid-silica matrix. Much like lipids (Figure 3B), the higher fluorescence intensity in the region local to the cells, as compared to the bulk film, shows Qdots to be localized near and around the cells during integration. It also appears that some portion of the Qdots were endocytosed by some of the *S. cerevisiae* cells, showing that the surface of the encapsulated cells remains accessible to, and interacts with the nanoparticles concentrated at their surfaces during integration.

Two distinct 655 nm Qdot spectral components were identified from the sample imaged in Figure 3C. Pure component spectra are shown in Figure S2. The red spectrum corresponds to the spectral component associated with the 655 nm Qdot spectrum. The green spectrum was obtained by removing the non-negativity constraint from the MCR analysis. This derivative looking component, when linearly combined with the quantum dot spectral component, models a shift in the quantum dot spectrum. An extensive description of this modeling approach can be reviewed in Haaland *et al*.[42] Figure 3D is a RGB image in which the two spectral components are false colored showing 655 nm Qdots (green) and 655 nm Qdots that have a red shifted spectrum (red). Interestingly, using this quantum dot spectra shift information, two different environments can be distinguished within Figure 3D. The spectrum of 655 nm Qdots localized near the yeast

cells was red shifted 7 nm, while the typical 655 nm Qdot spectrum was observed in the bulk film. To determine the source of this spectral shift, 655 nm Qdot spectra were obtained for Qdots in solutions at pH values 3-8, and in solution with *di*C_6 PC lipid. As shown in Figure S3A, no significant shift in 655 nm Qdot spectrum was observed over the studied pH range, indicating that the local gradient in pH near encapsulated cells does not contribute significantly to this shift. However, in the presence of *di*C_6 PC lipid, a red shift in the 655 nm Qdot spectrum of 2 nm was observed (Figure S3B, ~7 mg/mL lipid). From these data we conclude that the shift in 655 nm Qdot spectra in the lipid-silica-cell matrix is largely due to Qdot interactions with the lipid localized near the cells during self-encapsulation. Also, the lack of spectral shift for Qdots in the bulk film indicates that Qdots in this region have little contact with *di*C_6 PC lipid. This is consistent with observations that lipid is quickly solubilized from the film upon introduction of an aqueous droplet. It may also indicate that amino-derivatized PEG coated Qdots reconstituted near the cell surface during integration are incorporated in a more hydrophilic environment than in the original film.

Nanocomponents introduced with the aqueous cell suspension to lipid-templated films show preferential localization at the cell surface upon integration. Figure 3E shows that addition of palmitoyloleoyl phosphatidylcholine (POPC) liposomes to the yeast cell suspension, followed by deposition onto the silica film, resulted in fusion of liposome lipid (6% Texas Red-labeled DHPC, red emission) with the yeast cell surface. The thickness of liposome layer suggests that multiple fusion steps have occurred during integration, forming yeast supported multilayers. We have previously reported that liposome fusion with yeast cells in buffered solutions does not occur in the presence of

diC_6 PC lipid, nor under the pH range observed in this system.[43] These results demonstrate the importance of the cell-directed integration process, where long and short chain lipids are concentrated within a pH gradient, in forming yeast supported lipid multilayers from liposomes. This system could provide a simple means to introduce other functional components to the cell surface, including exogenous membrane bound proteins as we have previously reported utilizing our original cell-directed assembly approach.[43] In contrast to cell-directed assembly of bulk systems, when introduced with yeast cells onto a lipid-templated silica film, liposome lipid localization shows improved conformity with the cell surface. This improved conformity may result from *di*C_6 PC acting as a detergent that, upon droplet evaporation and cell-directed integration, reaches saturated concentration near the cells. This causes destabilization of the co-localized liposomes,[44] facilitating fusion of liposomes with other liposomes and formation of yeast supported multilayers with prioritized localization of longer chain lipids at the cell surface within the lipid-rich silica shell.

Living-Cell Directed Integration

The capability of viable cells to actively facilitate their integration was demonstrated by depositing an aqueous mixture of yeast cells and neutrally charged latex beads, serving as yeast cell surrogates (equivalent vol. fraction), onto a weakly condensed lipid-templated silica film (30 min aging from film formation). Following evaporation of the yeast-bead mixture, the samples were aged for an additional 1, 2, or 4 hours, and then rinsed thoroughly to remove non-integrated material. Images taken before and after rinsing (Figure 4A) show that one hour following droplet deposition nearly all yeast cells

(red emission) were retained in the film, while 95% ± 3% of latex beads (green emission) were removed by rinsing. Samples allowed to age for 2 and 4 hours also showed nearly complete integration of cells, but greater amounts of beads were retained 46% ± 7%, and 73% ± 13%, respectively. For aging times on the order of those required for complete condensation of the reconstituted lipid/silica concentrate (24-48 hours), 52% ± 12% of the beads remained post-rinsing (Figure 4B). As both *S. cerevisiae* cells and latex beads were surrounded by soluble silica and lipid concentrate during the initial stage of evaporation of the cell/bead dispersion, these data indicate that cells uniquely promote their integration. We attribute this cell-directed integration to the ability of cells to actively develop a pH gradient that catalyzes silica condensation within a thin three-dimensional volume surrounding the cells. Unlike *S. cerevisiae*, no pH gradient was observed near latex beads introduced to lipid-silica films. As the rate of silica condensation is a strong function of pH, and increases significantly between pH 3 and pH 6,[45] it is likely that the development of the localized pH gradient governs microorganism self-encapsulation within silica.

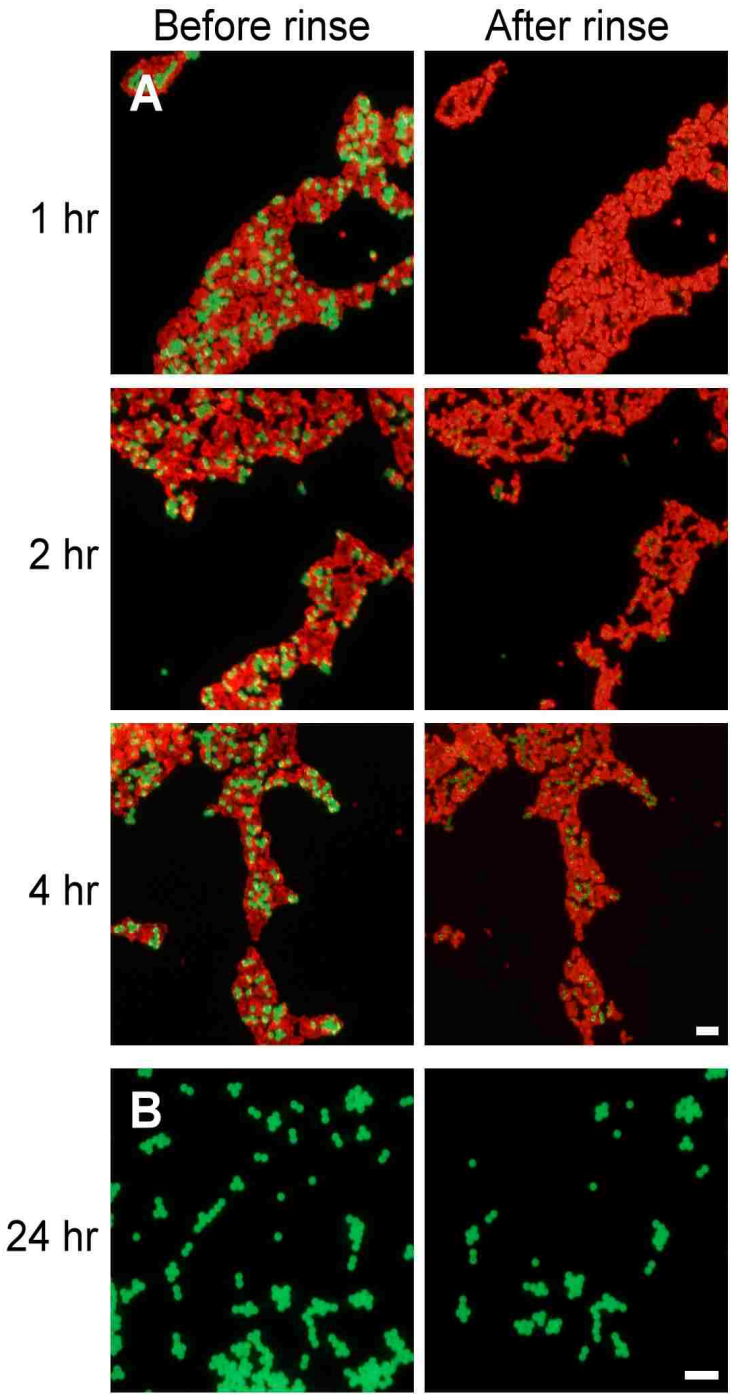

Figure 4. Fluorescence microscopy images of (A) a mixture of *S. cerevisiae* (Cyto64 stained, red emission) and cell surrogates (latex beads, green emission), and (B) latex beads in the absence of cells, that were allowed to integrate into lipid templated silica films for 1, 2, 4, or 24 hours, after which the films were rinsed to remove non-integrated material. The majority of *S. cerevisiae* cells are not removed by rinsing while beads are easily washed away under timescales shorter than that required for silica condensation. Scale bars = 25 μm.

Self-Catalyzed Silica Condensation

To further elucidate the importance of the active development of a localized pH gradient to cellular integration, we investigated integration under conditions of inhibited cellular response to osmotic stress (osmotic clamp). We have previously reported that viable cells experience osmotic stress during EISA,[27] rapidly excreting up to 35% of their cytosolic fluid volume in response to changes in turgor pressure in the cell membrane resulting from the increasing concentration of soluble silica and salts in the evaporating sol.[46] This results in an increase of water volume in the surrounding ~2 μm-thick region of the matrix by more than 60%, creating a gradient in pH in the immediate vicinity of a cell. Therefore, suppressing cellular response to osmotic stress should prevent the formation of this pH gradient, and consequently inhibit the proposed self-catalyzed cellular integration process.

Osmotic clamp was induced by adding 2% (vol.) of the osmolyte, DMSO to a split sample of yeast cells in aqueous suspension. This low concentration of DMSO has been shown to significantly inhibit osmotic equilibration due to its high osmolarity and rapid transport rate, while not significantly affecting the metabolic state of the cells.[47,48] Both the control cells (without DMSO) and cells under osmotic clamp were deposited onto weakly condensed lipid-templated silica films and allowed to age for 1 or 2 hours, after which the substrates were rinsed thoroughly to remove non-integrated material. The percentage of retained cells under both conditions is presented in Figure 5A. (Pre and post-rinsing images for control cells and cells under osmotic clamp are presented in the supplemental information, Figures S4, A and B, respectively). Control cells from the split sample showed a high degree of integration into the film for both time points (76% and

96%). In contrast, 87-96% of cells under osmotic clamp were removed from the film, indicating that they failed to integrate. Evidence that cells under this treatment are not completely precluded from responding to osmotic stress is shown by the 9% higher retention of cells between the 1 and 2 hour aging periods. Figure 5B shows *S. cerevisiae* cells under osmotic clamp introduced to lipid/silica films containing the pH sensitive probe OG. Prior to rinsing (which removes these clamped cells), we do not observe a gradient in pH (compare with Figure 3A). Rather, we find a uniform pH throughout the sample that corresponds to the pH of the bulk lipid-silica matrix (~pH 3, Figure 5B). Evidence that the integration process is actively directed by living cells is presented in Figure 5C, where we substituted apoptotic *S. cerevisiae* (i.e. those undergoing programmed cell death stimulated by rapid heating to 95˚C), for stationary phase yeast used in the previous experiments. Apoptotic yeast were introduced to a weakly condensed lipid-silica film as before, followed by two hours of aging and rinsing. As shown in Figure 5A, less than 3% of apoptotic yeast introduced to the film integrated. Figure 5C compares pH gradient development in active and apoptotic yeast introduced to OG-containing lipid-silica films prior to rinsing. We observe no pH gradient, in contrast to the active yeast (Figure 5C and 3A), and the surface of the apoptotic yeast appears collapsed because it does not catalyze 3D integration within a protective silica shell.

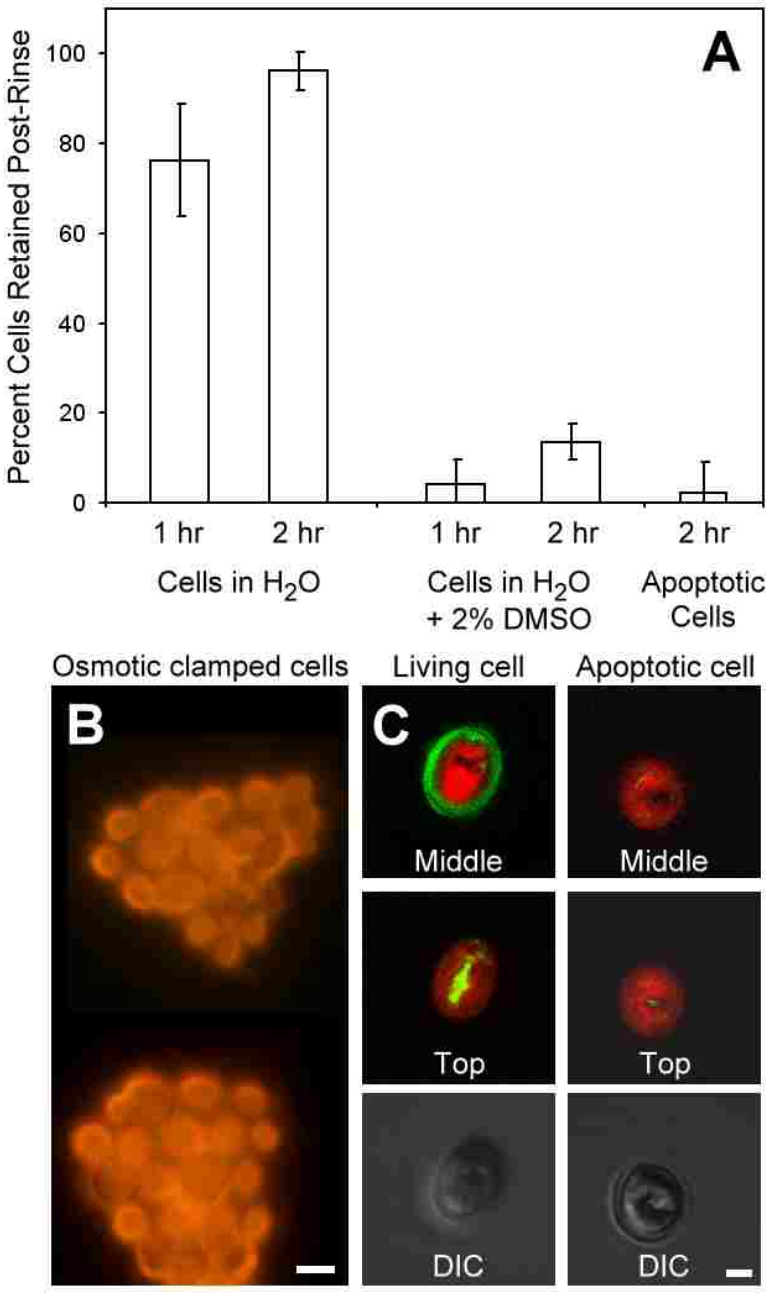

Figure 5. (A) Percent of *S. cerevisiae* cells that integrated into lipid templated silica films from samples containing cells in water only (control), cells in water with 2% DMSO (cells under osmotic clamp), and apoptotic cells in water (heat shock). Cells were allowed to integrate for 1 or 2 hours, after which samples were rinsed to remove non-integrated material. Error bars are the standard deviation of measurements obtained from 3 or more samples. (B-C) *S. cerevisiae* cells introduced to a lipid-templated mesoporous silica film containing OG prior to rinsing: (B) Fluorescence microscopy image of *S. cerevisiae* cells under osmotic clamp (Cyto64 stained, two separate fields). Scale bar = 3 μm. (C) Confocal fluorescence and DIC images of a single living or apoptotic (heat shock) *S. cerevisiae* cell (Cyto64 stained). Scale bar = 1 μm.

The ability of synthetic and natural polymers possessing amine functional groups to catalyze silica condensation has been widely studied,[49,50] and was investigated as a parallel mechanism for cell-directed silica condensation and self-integration. Strong attractive electrostatic interactions and weak hydrogen bonding between polycationic macromolecules and polysilicic acid has been shown to induce silica polymerization and precipitation.[51] As the cell wall of *S. cerevisiae* is known to display a multitude of proteins,[52] polycationic and/or amine functional regions exist on the exterior of the cell. The possible contribution of cationic protein residues to cell-directed catalysis of silica and self-encapsulation, along with electrostatic interactions between these residues and the negatively charged lipid-silica film, were examined using lysozyme protein coated beads. In the presence of soluble silica, lysozyme is known to induce local silicate condensation forming precipitated silica particles.[53]

Carboxylic acid functionalized fluorescent orange beads (5 μm diameter) were conjugated to lysozyme proteins *via* carbodiimide chemistry (see Experimental Methods). Lysozyme conjugation was verified by subsequent treatment with NHS ester Alexa Fluor 488 (green emission), which bound to free amines present on the surface of lysozyme, as shown in Figure 6A. Aqueous suspensions of lysozyme-bead conjugates were deposited onto weakly condensed lipid-templated silica films (aged 30 min prior to bead deposition) and aged for 5, 15, or 30 minutes post droplet evaporation, followed by thorough rinsing. Interestingly, nearly 50% of the lysozyme-bead conjugates under each incubation period remained in the film, as shown in Figure 6B. These results differ significantly from those obtained with latex beads which showed only ~5% integration efficiency (Figure 4A). This demonstrates that lysozyme protein significantly interacts

with the lipid-silica film. The extent of this interaction that can be attributed to electrostatic binding between the positively charged lysozyme molecules (pI ~10) and the lipid-silica film, independent of polycationic residue induced catalysis of silica condensation, was investigated by introducing lysozyme-bead conjugates to a lipid-templated mesoporous silica film that was previously allowed to fully condense. As only trace levels of silica precursors are solubilized from the fully condensed film, silica condensation cannot contribute to the population of lysozyme-bead conjugates that remain post-rinsing. As shown in Figure 6B (grey bar) approximately 10% of the lysozyme-bead conjugates remain. Retention of this lower population of lysozyme-bead conjugates is attributed to the strong electrostatic interactions between lysozyme and the silica film. Further, this result shows that the larger fraction of lysozyme-bead conjugates retained upon introduction to a weakly condensed lipid-silica film can be attributed to polycationic residue catalyzed silica condensation.

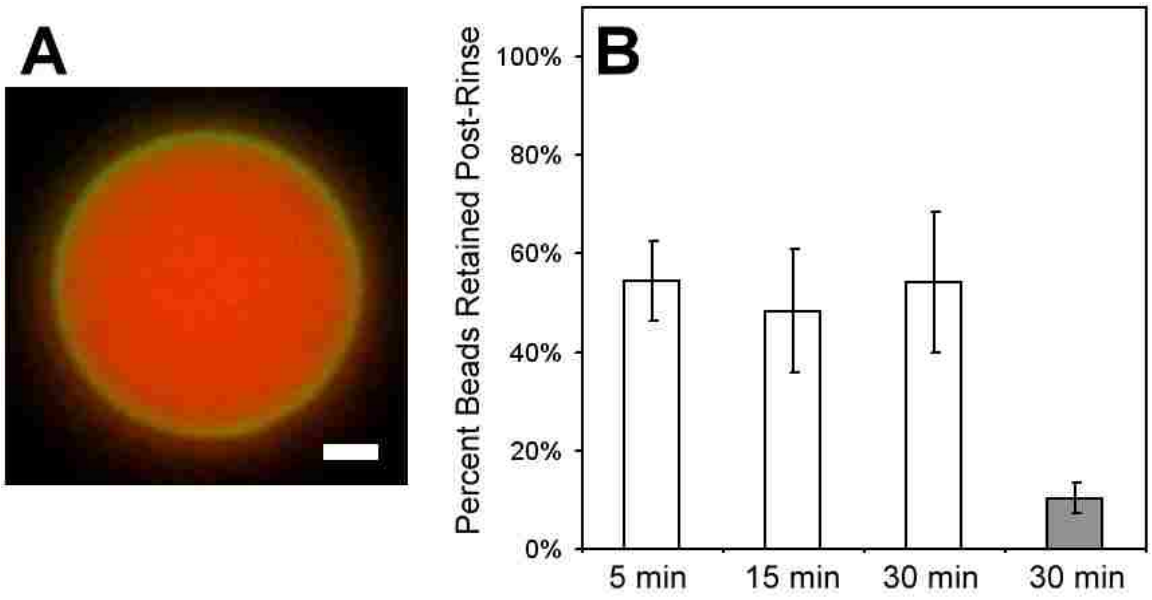

Figure 6. (A) Lysozyme protein conjugated fluorescent orange 5 μm beads. Lysozyme conjugation verified by subsequent treatment with NHS ester AlexaFluor 488 (green emission). Scale bar = 1 μm. (B) Percent of lysozyme-bead conjugates that integrated into weakly condensed (white bars) and fully condensed (grey bar) lipid-templated silica films. Lysozyme-bead conjugates were allowed to integrate for 5, 15, or 30 minutes, after which samples were rinsed to remove non-integrated material. Error bars are the standard deviation of measurements obtained from 3 or more samples.

These data provide evidence that polycationic and/or amine functional regions on the exterior of *S. cerevisiae* may contribute to self-integration. It should also be noted that in the case of living microorganism encapsulation, a neutral pH develops near the cellular surface which would increase the rate of cell wall protein/peptide induced silica condensation.[51] However, these data, combined with the poor integration of *S. cerevisiae* under osmotic clamp or apoptotic conditions, both of which still display proteins, albeit at low pH, indicate that this is a minor mechanism under the time scales investigated in this study. Finally, the localized lipid lamellar interface formed during cellular integration may serve to physically isolate the cell surface and surface proteins from silica

precursors, further reducing the impact of polycationic macromolecule induced silica condensation on cellular integration.

Integrated Cell Viability

Viability of integrated cells depended strongly on storage conditions. Substrates with integrated cells placed into buffer or media (YPD) approximately 35 minutes post droplet evaporation showed 15% ± 6.9% viability as measured by CFDA/PI assay (see Experimental Methods). If maintained under these solutions at room temperature the thin lipid-silica shell encapsulating the cells slowly dissolved freeing yeast cells between 3-5 days post integration. If under YPD medium, released cells would replicate demonstrating that the cells do remain viable and culturable following cell-directed integration into the lipid-silica mesophase film.

Substrates with integrated cells stored under dry room temperature conditions showed significant loss in viability over the first few hours post integration with less than 4% viable cells after 24 hours. However, addition of trehalose to the matrix, a disaccharide known to provide improved tolerance to desiccation, significantly improved viability of integrated cells when stored dry. If trehalose was added directly to the aqueous suspension of cells, followed by deposition onto the lipid-silica film, we found that the droplet did not completely evaporate, forming a gel phase that prevented cellular integration into the film. Alternatively, addition of trehalose to the lipid-silica precursor solution, followed by film formation, allowed for integration of cells into the trehalose containing film. We propose that trehalose was solubilized from the film by the aqueous cell suspension, and accumulated near the cells in a manner similar to that observed for

solubilized lipid and silica. The lower concentration of trehalose solublized from the film did not form a gel phase, allowing development of evaporation induced osmotic stress and pH gradients required for integration. A strong dependence of viability on trehalose film concentration was observed, and is shown in Figure S5. At 45 mg/mL trehalose in the lipid-silica precursor solution, 23% ± 10% of cells remained viable after dry storage at room temperature for 7 days. In these experiments 2×10^5 cells/cm^2 are initially integrated into the lipid-silica mesophase films, leaving approximately 4.5×10^4 viable cells/cm^2 following 7 days of dry storage. This considerable population of viable cells is sufficient for subsequent use or experimentation.

CONCLUSIONS

In summary, we have described a unique method in which cells introduced onto a solid state lipid-silica mesophase film actively reconstruct the surface to create a fully 3D bio/nano interface composed of a lipid-rich silica shell that coherently interfaces the cells with the nanostructured inorganic matrix. We attribute this cell-directed integration to the ability of cells to actively develop a pH gradient in response to evaporation induced osmotic stress, which catalyzes silica condensation within a thin three-dimensional volume surrounding the cells. Auxiliary nanocomponents added to the lipid/silica mesophase film, or introduced with the cells, were localized at the cellular surface providing a means to introduce foreign functionalities, which remained accessible to and interacted with the cellular surface. This process is simple and does not expose cells to toxic solvents, chemical byproducts or drying stresses, preserving the original cell

morphology. We expect this method to be general and adaptable to other bacterial and fungal cells, and even mammalian cells. It promises to be useful as a new technique for integrating bio with nano, impacting fundamental studies in nanoparticle toxicology, cell-cell signaling, and development of bioelectronics and cell-based biosensors.

EXPERIMENTAL METHODS

Materials. Aqueous solutions were prepared with 18 MΩ water using a Barnstead Nanopure water purifier (Boston, MA). Tetraethylorthosilicate (TEOS), Tetramethylorthosilicate (TMOS), sodium molybdate, ascorbic acid, lysozyme (from chicken egg white) and hydrochloric acid (HCl) were purchased from Sigma-Aldrich (St. Louis, MO). 2-[4-(2-Hydroxyethyl)-1-piperazine]ethanesulfonic acid (HEPES), 1-Ethyl-3-[3-dimethylaminopropyl]carbodiimide hydrochloride (EDC), 4-aminobenzoic acid and N-hydroxysuccinimide (NHS), and ethanol (absolute) were obtained from Acros Organics (Beel, Belgium). Phosphate buffer saline (PBS) solution, pH 7.4 (11.9 mM phosphates, 137 mM NaCl, and 2.7 mM KCl), sodium hydroxide (NaOH), potassium hydroxide (KOH), and dimethyl sulfoxide (DMSO) were purchased from Fischer Scientific (Pittsburgh, PA). 1,2-Dihexanoyl-*sn*-glycero-3-phosphocholine (*di*C_6 PC), 1-hexanoyl-2-{6-[(7-nitro-2-1,3-benzoxadiazol-4-yl)amino]hexanoyl}-*sn*-glycero-3-phosphocholine (NBD-*di*C_6 PC), 1-hexanoyl-2-{6-[(5-(and-6)-carboxytetramethylrhodamine)amino]hexanoyl-*sn*-glycero-3-phosphocholine (TAMRA-*di*C_6 PC), and Palmitoyloleoyl phosphatidylcholine (POPC) were obtained from Avanti Polar Lipids (Alabaster, AL). 2', 7'-difluorofluorescein Oregon Green 488 (OG), Alexa

Fluor 488 carboxylic acid succinimidyl ester (NHS-Alexa Fluor 488), amino-derivatized polyethylene glycol (PEG) coated 655 nm quantum dots (655 nm Qdots), Texas Red labeled DHPE, and *Funga* Light^{TM} CFDA/PI yeast viability kit were from Invitrogen (Carlsbad, CA). Latex beads (5 μm, fluorescent green) were from Duke Laboratories (now part of Thermo Scientific). Carboxyl functionalized Suncoast Yellow beads (5 μm, fluorescent orange) were from Bangs Laboratories (Fishers, IN).

Lipid-Templated Silica Film Formation. Pre-hydrolyzed TEOS stock solutions (A2**) were prepared by refluxing 61 mL TEOS, 61 mL ethanol (absolute), 4.9 mL nanopure water, and 0.2 mL of 0.07N HCl (molar ratio 1: 4: 1: 5×10^{-5}) for 90 minutes at 60°C. Stock solutions were stored at -20°C. A2** stock was used to prepare the precursor sol solution by adding 0.25 mL A2**, 0.20 mL ethanol (absolute), 0.16 mL of 0.05N HCl, and 0.40 mL nanopure water (molar ratio of 1 TEOS: 4.0 ethanol: 2.0 water: 0.005 HCl) to 30 mg of *di*C_6 PC. This solution was allowed to age at room temperature for 20 minutes. Following aging the solution was spin coated onto 25 mm No. 1.5 round glass coverslips which had been pretreated in 0.1 M KOH for at least 2 hours, washed with 1% Alconox in nanopure water, and rinsed with nanopure water and ethanol, and then cleaned in a UVO cleaner (Jelight model 342) for 5 minutes. Spin coating occurred at 1500 rpm for 30 seconds (Laurell model WS-400B) at <20% relative humidity. Films containing fluorescently labeled lipid (0.1% of total lipid) were prepared as described above with the addition of 0.03 mg of either NBD- or TAMRA- *di*C_6 PC to the sol precursor solution prior to the 20 min room temperature incubation. Films containing OG or 655 nm Qdots were prepared as described above with the addition of 20 μL OG

solution (13.5 mM), or 10 μL 655 nm Qdot solution (8 μM), to 1 mL of the sol precursor solution prior to the 20 minute room temperature incubation.

Cell Self-Integration. *S. cerevisiae* (strain S288C, Invitrogen) was grown in glucose-based rich medium (YPD) to G0 or stationary phase. Cells were collected by centrifugation, washed 3 times in nanopure water, and resuspended in nanopure water. Aqueous suspensions of yeast were introduced onto preformed lipid-templated mesoporous silica films 30 to 120 minutes after formation in 0.5 μL droplets (10^5-10^6 cells/mL) and allowed to dry. Once dry, substrates were allowed to rest for given periods of time and then rinsed thoroughly with nanopure water (10 second exposure to water stream, followed by drying with N_2 stream) to remove non-integrated material.

Reduced Molybdic Acid Assay for Soluble Silica Content. The amount of silica removed from the film by a drop of water residing on the film surface was quantified by the reduced molybdic acid assay method.[40,45] This assay is more sensitive then the molybdic acid (MA) test, allowing calibration down to 2 μM of silicic acid. 10 mM sodium molybdate was prepared in DI water and pH was adjusted to 1.2 with HCl. Plastic vessels were used to avoid silica contamination. The sample was collected by placing a drop of DI water on the silica-lipid film for 10 minutes followed by careful removal of 80% of the drop without scratching the film. This sample was incubated overnight after adding 40 μL of 5 mM NaOH to dissolve any silica aggregates. The sample was placed into a 1 mL cuvette, along with 0.8 mL of the sodium molybdate solution and allowed to incubate for 30 minutes. Following incubation 40 μL of 0.5 M ascorbic acid was added to

the cuvette. Immediately the previously clear assay solution started turning blue. Exactly 60 seconds after ascorbic acid addition, the sample was scanned with the UV-Vis spectrophotometer. The scan (500-700 nm) took 12 seconds. Timing is important as the color intensity of reduced molybdic acid is unstable. Satisfactory linear calibration curves based on hydrolysed TMOS were obtained with every experiment. Silica concentration in film dissolution samples was determined by least-squares fit to an absorbance curve derived from the calibration data.

Fluorescently Labeled Liposome Formation. Palmitoyloleoyl phosphatidylcholine (POPC) was dissolved in chloroform, dried, and maintained overnight under vacuum to remove residual solvent. 2.5 mg of lipid (including Texas Red labeled DHPE at 6 wt%) was dissolved in 0.5× PBS, sonicated briefly, and extruded through a 100 nm filter (Millipore) ten times.

Lysozyme-Bead Conjugation. Carboxyl functionalized 5 μm diameter beads were diluted 10 fold from stock solution into 1 mL of 10 mM HEPES buffer solution, pH 7.5, containing 10 mM EDC. Following a 20 minute incubation, the beads were pelletted by centrifugation and resuspended in 1 mL of 10 mM HEPES buffer, pH 7.5, containing 1.5 mg of lysozyme protein, and incubated for 2-4 hours at room temperature. Following conjugation the beads were washed 3x with HEPES solution and stored at 4 ºC until use. To verify lysozyme conjugation onto the beads, 10 μL of stock NHS-Alexa Fluor 488 solution was added to 1 mL of the lysozyme conjugated beads in 10 mM HEPES buffer,

pH 7.5, for 2-4 hours at room temperature. Following incubation the beads were washed 3x with HEPES solution and then imaged.

Atomic Force, Fluorescence, and Scanning Electron Microscopy. Atomic Force microcopy was carried out on a MFP-3B Bio AFM (Asylum Research, Santa Barbara, CA) operated in tapping mode in air and in liquid. For imaging in air AC240 TS cantilevers were used (Olympus, k = 2 N/m). For imaging in water TR400 PB cantilevers (Olympus, k = 0.09 N/m) were used. For applications where film thickness was determined by AFM, an image at least 20 × 20 μm in size was acquired and analyzed. Fluorescence microscopy imaging was performed on an Olympus IX70 microscope and recorded using an Olympus DP71 camera. A JEOL 6701F scanning electron microscope (SEM) operating at 5kV was used to directly image cells integrated into lipid-silica films without further preparation.

Hyperspectral Confocal Fluorescence Microscopy. A hyperspectral confocal fluorescence microscope was used to image the yeast cells encapsulated in the lipid-silica matrices. This unique microscope, which was designed and built at Sandia,[54] is a fully confocal design capable of collecting 8300 pixels per second. Each pixel consists of 512 emission wavelengths spanning the spectral region of 490 – 800 nm when the sample is excited using a solid state 488 nm laser (Coherent, Incorporated). These emission wavelengths are dispersed onto a electron multiplying charge coupled device (EMCCD) detector using a custom built high throughput prism spectrometer. The resolution of this microscope consists of a lateral (x,y) spatial resolution of 0.25 μm, an axial (z) resolution

is 0.6 μm and a spectral resolution of better than 3 nm. For the collection of the encapsulated yeast cell samples, a oil immersion 60x objective with a numerical aperature of 1.4 was used to collect the images.

Once the hyperspectral images have been collected, the images are preprocessed to remove unwanted spectral artifacts and then the images are analyzed using Multivariate Curve Resolution (MCR).[55] The preprocessing consisted of the following steps: 1) detection and removal of cosmic spikes collected on the EMCCD, 2) subtraction of the dark image to remove the effects of a structured noise source from the spectral data, and 3) removal of the spectral offset arising from the electronics of the EMCCD. A more detailed description of the preprocessing steps can be found in the experimental section in Jones *et al*.[55] Following these preprocessing steps, MCR analyses of the spectral image data sets were conducted. MCR is a powerful multivariate analysis technique in which the associated algorithms can extract the pure spectral emission and the corresponding intensities of each spectral component for each pixel in the image. In addition, MCR can discover all emitting fluorphores that are above the noise floor without any *a-priori* information regarding the sample being imaged (i.e., no information is needed to discover and quantify the fluorophores present in the sample images). Therefore, both known and unknown spectral emissions can be discovered and quantified within the images. Also, unlike most filter-based fluorescence microscopes, it not necessary to have well separated fluorophores to obtain quantitative images since the MCR algorithms can significantly reduce the amount of cross-talk between fluorophores. Further information on MCR implementation, and decriptions of the MCR software written in Matlab and C code, are detailed elsewhere.[42,55-59]

Integrated Yeast Viability Assay. Integrated yeast viability was measured using the *Funga* Light™ assay (Invitrogen) containing a cell permeable non-specific esterase substrate (acetoxymethyl ester 5-carboxyfluorescein diacetate, CFDA) and a cell membrane integrity indicator (propidium iodide, PI). Viability assay was performed using the manufacturer's protocol with slight modifications. 1 μL of CFDA solution (1 mg in 100 μL DMSO) and 1 μL of PI solution (20 mM in H_2O) were added to 1 mL of 1× PBS, pH 7.4. This solution was carefully pipetted onto substrates containing cells integrated in a lipid-silica film and incubated at room temperature for 45-60min. Following incubation cells, still under CDFA/PI assay solution, were imaged with an inverted fluorescence microscope. Cells with esterase activity and intact membranes fluoresced green and were counted as viable. Cells without esterase activity and damaged membranes fluoresced red and were not counted as viable. Cells with residual esterase activity and damaged membranes fluoresced yellow and were not counted as viable.

References

1. Kandimalla, V. B.; Tripathi, V. S.; Ju, H. Immobilization of Biomolecules in Sol–Gels: Biological and Analytical Applications. *Crit. Rev. Anal. Chem.* **2006,** *36*, 73-106.
2. Salaita, K.; Wang, Y.; Mirkin, C. A. Applications of Dip-Pen Nanolithography. *Nat. Nanotech.* **2007**, *2*, 145-155.
3. Dave, B. C.; Dunn, B.; Valentine, J. S.; Zink, J. I. Sol-Gel Encapsulation Methods for Biosensors. *Anal. Chem.* **1994**, *66*, 1120A-1127A.
4. Carballeria, J. D.; Quezada, M. A.; Hoyos, P.; Simeó, Y.; Hernaiz, M. J.; Alcantara, A. R.; Sinisterra, J. V. Microbial Cells As Catalysts for Stereoselective Red-Ox Reactions. *Biotechnol. Adv.* **2009**, *27*, 686-714.
5. Yap, F. L.; Zhang, Y. Proteins and Cell Micropatterning and its Integration with Micro/Nanoparticles Assembly. *Biosens. Bioelectron.* **2007**, *22*, 775-788.

6. Ispas, C.; Sokolov, I.; Andreescu, S. Enzyme-Functionalized Mesoporous Silica for Bioanalytical Applications. *Anal. Bioanal. Chem.* **2009**, *393*, 543-554.
7. Gupta, R.; Chaudhury, N. K. Entrapment of Biomolecules in Sol–Gel Matrix for Applications in Biosensors: Problems and Future Prospects. *Biosens. Bioelectron.* **2007**, *22*, 2387-2399.
8. Carturan, G.; Toso, R. B.; Boninsegna, S.; Monte, R. D. Encapsulation of Functional Cells by Sol–Gel Silica: Actual Progress and Perspectives for Cell Therapy. *J. Mater. Chem.* 2004, *14*, 2087-2098.
9. Ellerby, L. M.; Nishida, C. R.; Nishida, F.; Yamanaka, S.; Dunn, B.; Valentine, J. S.; Zink, J. I. Encapsulation of Proteins in Transparent Porous Silicate Glasses Prepared by the Sol-Gel Method. *Science* **1992**, *255*, 1113-1115.
10. Sheldon, R. A. Enzyme Immobilization: The Quest for Optimum Performance. *Adv. Synth. Catal.* **2007**, *349*, 1289-1307.
11. Orive, G.; Hernández, R. M.; Gascón, A. R.; Calafiore, R.; Chang, T. M. S.; de Vos, P.; Hortelano, G.; Hunkeler, D.; Lacík, I.; Pedraz, J. L. History, Challenges and Perspectives of Cell Microencapsulation. *Trends Biotech.* **2004**, *22*, 87-92.
12. Orive, G.; Hernández, R. M.; Gascón, A. R.; Calafiore, R.; Chang, T. M. S.; de Vos, P.; Hortelano, G.; Hunkeler, D.; Lacík, I.; Shapiro, A. M. J.; Pedraz, J. L. Cell Encapsulation: Promise and Progress. *Nat. Med.* **2003**, *9*, 104-107.
13. Murua, A.; Portero, A.; Orive, G.; Hernández, R. M.; de Castro, M.; Pedraz, J. L. Cell Microencapsulation Technology: Towards Clinical Application. *J. Control. Release* **2008**, *132*, 76-83.
14. Carturan, G.; Campostrini, R.; Dirè, S.; Scardi, V.; de Alteriis, E. Inorganic Gels for Immobilization of Biocatalysts: Inclusion of Invertase-Active Whole Cells of Yeast (*Saccharomyces cerevisiae*) into Thin Layers of SiO_2 Gel Deposited on Glass Sheets. *J. Mol. Catal.* **1989**, *57*, L13-L16.
15. Avnir, D.; Coradin, T.; Lev, O.; Livage, J. Recent Bio-Applications of Sol–Gel Materials. *J. Mater. Chem.* **2006**, *16*, 1013-1030.
16. Pope, E. J. A.; Braun, K.; Peterson, C. M. Bioartificial Organs I: Silica Gel Encapsulated Pancreatic Islets for the Treatment of Diabetes Mellitus. *J. Sol-Gel Sci. Technol.* **1997**, *8*, 635-639.
17. Chia, S.; Urano, J.; Tamanoi, F.; Dunn, B.; Zink, J. I. Patterned Hexagonal Arrays of Living Cells in Sol-Gel Silica Films. *J. Am. Chem. Soc.* **2000**, *122*, 6488-6489.
18. Nassif, N.; Roux, C.; Coradin, T.; Rager, M.-N.; Bouvet, O. M. M.; Livage, J. A Sol–Gel Matrix to Preserve the Viability of Encapsulated Bacteria. *J. Mater. Chem.* **2003**, *13*, 203-208.
19. Nassif, N.; Bouvet, O.; Rager, M. N.; Roux, C.; Coradin, T.; Livage, J. Living Bacteria in Silica Gels. *Nat. Mater.* **2002**, *1*, 42-44.
20. Conroy, J. F. T.; Power, M. E.; Martin, J.; Earp, B.; Hosticka, B.; Daitch, C. E.; Norris, P. M. Cells in Sol-Gels I: A Cytocompatible Route for the Production of Macroporous Silica Gels. *J. Sol-Gel. Sci. Technol.* **2000**, *18*, 269-283.
21. Gill, I.; Ballesteros, A. Encapsulation of Biologicals within Silicate, Siloxane, and Hybrid Sol-Gel Polymers: An Efficient and Generic Approach. *J. Am. Chem. Soc.* **1998**, *120*, 8587-8598.

22. Yu, D.; Volponi, J.; Chhabra, S.; Brinker, C. J.; Mulchandani, A.; Singh, A. K. Aqueous Sol–Gel Encapsulation of Genetically Engineered *Moraxella spp*. Cells for the Detection of Organophosphates. *Biosens. Bioelection.* **2005**, *20*, 1433-1437.
23. Coiffier, A.; Coradin, T.; Roux, C.; Bouvet, O. M. M.; Livage, J. Sol–Gel Encapsulation of Bacteria: A Comparison Between Alkoxide and Aqueous Routes. *J. Mater. Chem.* **2001**, *11*, 2039-2044.
24. Finnie, K. S.; Bartlett, J. R.; Woolfrey, J. L. Encapsulation of Sulfate-Reducing Bacteria in a Silica Host**.** *J. Mater. Chem.* **2000**, *10*, 1099-1101.
25. Campostrini, R.; Carturan, G.; Caniato, R.; Piovan, R.; Filippini, G.; Innocenti, G.; Cappelletti, E. M. Immobilization of Plant Cells in Hybrid Sol-Gel Materials. *J. Sol-Gel Sci. Technol.* **1996**, *7*, 87-97.
26. Muraca, M.; Vilei, M. T.; Zanusso, G. E.; Ferraresso, C.; Boninsegna, S.; Monte, R. D.; Carraro, P.; Carturan, G. SiO_2 Entrapment of Animal Cells: Liver-Specific Metabolic Activities in Silica-Overlaid Hepatocytes. *Artif. Organs* **2002**, *26*, 664-669.
27. Baca, H. K.; Ashley, C.; Carnes, E.; Lopez, D.; Flemming, J.; Dunphy, D.; Singh, S.; Chen, Z.; Liu, N. G.; Fan, H. Y.; Lopez, G. P.; Brozik, S. M.; Werner-Washburne, M.; Brinker, C. J. Cell–Directed Assembly of Lipid-Silica Nanostructures Providing Extended Cell Viability. *Science* **2006**, *313*, 337-341.
28. Baca, H. K.; Carnes, E.; Singh, S.; Ashley, C.; Lopez, D.; Brinker, C. J. Cell–Directed Assembly of Bio/Nano Interfaces–A New Scheme for Cell Immobilization. *Acc. Chem. Res.* **2007**, *40*, 836-845.
29. Brinker, C. J.; Lu, Y. F.; Sellinger, A.; Fan, H. Y. Evaporation-Induced Self-Assembly: Nanostructures Made Easy. *Adv. Mater.* **1999**, *11*, 579-585.
30. Carnes, E. C.; Lopez, D. M.; Donegan, N. P.; Cheung, A.; Gresham, H.; Timmins, G. S.; Brinker, C. J. Confinement-Induced Quorum Sensing of Individual *Staphylococcus aureus* Bacteria. *Nat. Chem. Biol.* **2010**, *6*, 41-45.
31. Stevens, M. M.; George, J. H. Exploring and Engineering the Cell Surface Interface. *Science* **2005**, *310*, 1135-1138.
32. Zhange, S. G. Beyond the Petri Dish. *Nat. Biotechnol.* **2004**, *22*, 151-152.
33. Stoodley, P.; Sauer, K.; Davies, D. G.; Costerton, J. W. In *AnnualReview of Microbiology*; Ornston, L. N., Balows, A., Gottesman, S., Eds.; Annual Reviews: Palo Alto, CA, 2002; Vol. 56, pp 187-209.
34. Raghavan, S.; Chen, C. S. Micropatterned Environments in Cell Biology. *Adv. Mater.* **2004**, *16*, 1303-1313.
35. Hu, H.; Larson, R. G. Analysis of the Effects of Marangoni Stresses on the Microflow in an Evaporating Sessile Droplet. *Langmuir* **2005**, *21*, 3972-3980.
36. Kuncicky, D. M.; Velev, O. D. Surface-Guided Templating of Particle Assemblies inside Drying Sessile Droplets. *Langmuir* **2008**, *24*, 1371-1380.
37. Truskett, V. N. Influence of Surfactants on an Evaporating Drop: Fluorescence Images and Particle Deposition Patterns. *Langmuir* **2003**, *19*, 8271-8279.
38. Deegan, R. D.; Bakajin, O.; Dupont, T. F.; Huber, G.; Nagel, S. N.; Witten, T. A. Capillary Flow As the Cause of Ring Stains from Dried Liquid Drops. *Nature* **1997**, *389*, 827-829.
39. Brinker, C. J.; Scherer, G. *Sol-gel Science: The Physics and Chemistry of Sol-Gel Processing*; Academic: Boston, MA **1990**.

40. Andersson, L. H. Determination of Silica. VII. Some Experiments with the Gravimetric Silica Determinations. *Arkiv för Kemi* **1962**, *19*, 223-233.
41. Doshi, D. A.; Gibaud, A.; Goletto, V.; Lu, M.; Gerung, H.; Ocko, B.; Han, S. M.; Brinker, C. J. Peering into the Self-Assembly of Surfactant Templated Thin-Film Mesophases. *J. Amer. Chem. Soc.* **2003**, *125*, 11646-11655.
42. Haaland, D. M.; Jones, H. D. T.; Van Benthem, M. H.; Sinclair, M. B.; Melgaard, D. K.; Stork, C. L.; Pedroso, M. C.; Liu, P.; Brasier, A. R.; Andrews, N. L.; Lidke, D. S. Hyperspectral Confocal Fluorescence Imaging: Exploring Alternative Multivariate Curve Resolution Approaches. *Appl. Spectrosc.* **2009**, *63*, 271-279.
43. Carnes, E. C.; Harper, J. C.; Ashley, C. E.; Lopez, D. M.; Brinker, L. M.; Liu, J.; Singh, S.; Brozik, S. M.; Brinker, C. J. Cell-Directed Localization and Orientation of a Functional Foreign Transmembrane Protein within a Silica Nanostructure. *J. Am. Chem. Soc.* **2009**, *131*, 14255-14257.
44. Rigaud, J.-L.; Paternostre, M.-T.; Bluzat, A. Mechanisms of Membrane Protein Insertion into Liposomes during Reconstitution Procedures Involving the Use of Detergents. 2. Incorporation of the Light-Driven Proton Pump Bacteriorhodopsin. *Biochemistry* **1988**, *27*, 2677-2688.
45. Iler, R. L. *The Chemistry of Silica*; John Wiley & Sons: New York, NY **1979**.
46. de Maranon, I. M.; Marechal, P.-A., Gervais, P. Passive Response of *Saccharomyces cerevisiae* to Osmotic Shifts: Cell Volume Variations Depending on the Physiological State. *Biochem. Biophys. Res. Commun.* **1996**, *227*, 519-523.
47. Yang, B.; Kim, J. K.; Verkman, A. S. Comparative Efficacy of $HgCl_2$ with Candidate Aquaporin-1 Inhibitors DMSO, Gold, TEA^+ and Acetazolamide. *FEBS Lett.* **2006**, *580*, 6679-6684.
48. de Bruijne, A. W.; van Steveninck, J. Lysis of Yeast Cells and Erythrocytes by Dimethylsulfoxide. *Biochem. Pharmacol.* **1972**, *21*, 153-162.
49. Patwardhan, S. V.; Clarson, S. J.; Perry, C. C. On the Role(s) of Additives in Bioinspired Silicification. *Chem. Commun.* **2005**, 1113-1121.
50. Lopez, P. J.; Gautier, C.; Livage, J.; Coradin, T. Mimicking Biogenic Silica Nanostructures Formation. *Curr. Nanosci.* **2005**, *1*, 73-83.
51. Coradin, T.; Livage, J. Aqueous Silicates in Biological Sol-Gel Applications: New Perspectives for Old Precursors. *Acc. Chem. Res.* **2007**, *40*, 819-826.
52. Ruiz-Herrera, J. *Fungal Cell Wall: Structure, Synthesis, and Assembly*; CRC: Boca Raton, FL **1992**.
53. Coradin, T.; Coupé, A.; Livage, J. Interactions of Bovine Serum Albumin and Lysozyme with Sodium Silicate Solutions. *Colloids Surf., B* **2003**, *29*, 189-196.
54. Sinclair, M. B.; Haaland, D. M.; Timlin, J. A.; Jones, H. D. T. Hyperspectral Confocal Microscope. *Appl. Optics*, **2006**, *45***,** 6283-6291.
55. Jones, H. D. T.; Haaland, D. M.; Sinclair, M. B.; Melgaard, D. K.; Van Benthem, M. H.; Pedroso, M. C. Weighting Hyperspectral Image Data for Improved Multivariate Curve Resolution Results. *J. Chemometr.* **2008**, *22***,** 482-490.
56. Van Benthem, M. H.; Keenan, M. R.; Haaland, D. M. Application of Equality Constraints on Variables During Alternating Least Squares Procedures. *J. Chemometr.* **2002**, *16***,** 613-622.

57. Van Benthem, M. H.; Keenan, M. R. Fast Algorithm for the Solution of Large-Scale Non-Negativity-Constrained Least Squares Problems. *J. Chemometr.* **2004**, *18,* 441-450.
58. Kotula, P. G.; Keenan, M. R.; Michael, J. R. Automated Analysis of SEM X-Ray Spectral Images: A Powerful New Microanalysis Tool. *Microsc. Microanal.* **2003**, *9,* 1-17.
59. Ohlhausen, J. A. T.; Keenan, M. R.; Kotula, P. G.; Peebles, D. E. Multivariate Statistical Analysis of Time-of-Flight Secondary Ion Mass Spectrometry Images using AXSIA. *Appl. Surf. Sci.* **2004**, *231/232,* 230-234.

SUPPORTING INFORMATION

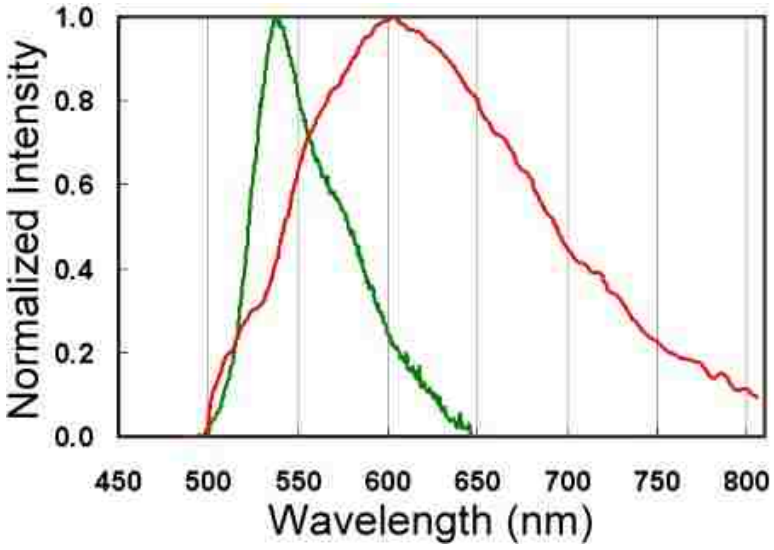

Figure S1. Pure component spectra of Oregon Green (green) and yeast autofluorescence (red) used to generate the image in Figure 3, A.

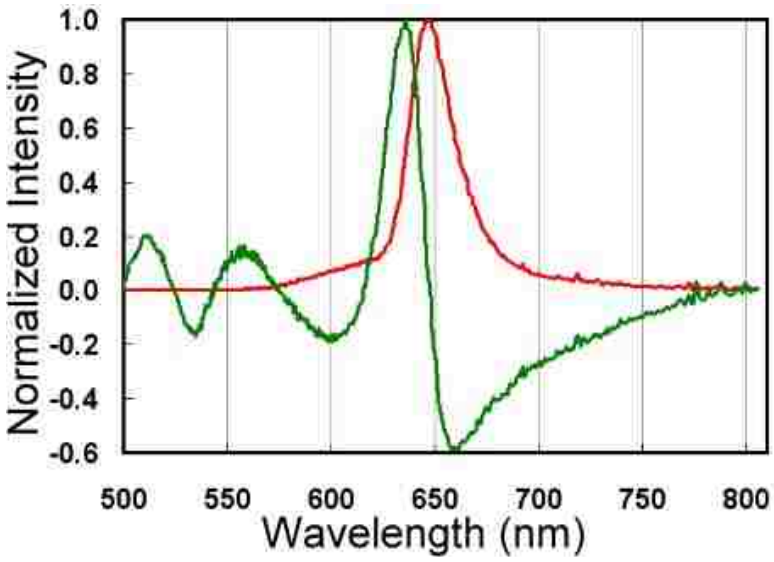

Figure S2. Pure component spectra from 655nm quantum dots used to generate the image in Figure 3, D. The red spectrum was observed for 655nm Qdots in the region near *S. cerevisiae* cells entrapped in a lipid-templated mesoporous silica film. The green spectrum corresponded to 655nm Qdots in the bulk film.

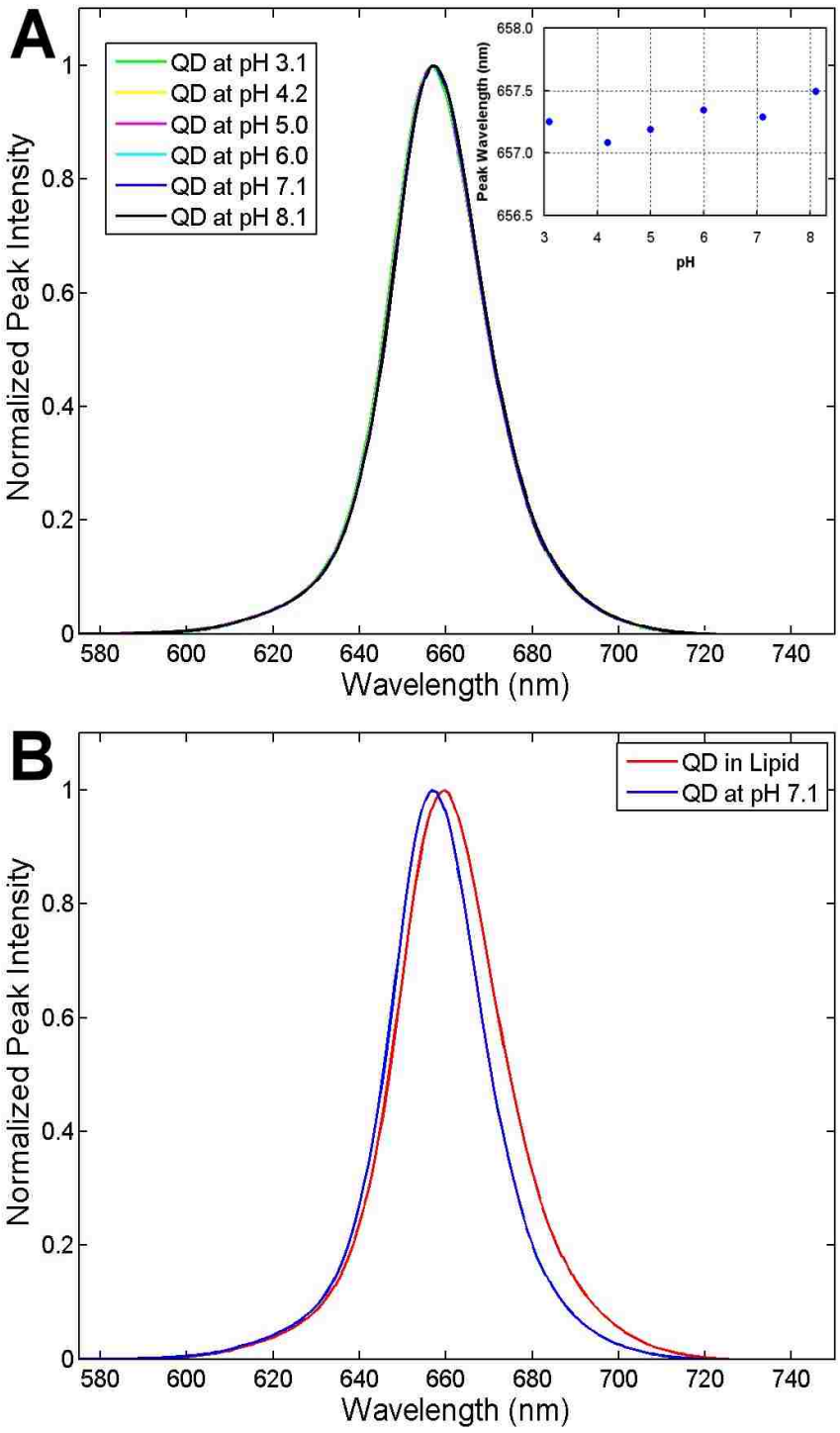

Figure S3. (A) Pure component spectra from 655 nm quantum dots in phosphate buffer solutions at various pHs. Inset: Peak wavelength vs. solution pH value. (B) Pure component spectra from 655 nm quantum dots in phosphate buffer, pH 7.1 (blue) and in phosphate buffer, pH 7.1, with ~7 mg/mL *di*C_6 PC lipid (red). Quantum dots were incubated in the given pH or lipid solution overnight at room temperature prior to imaging.

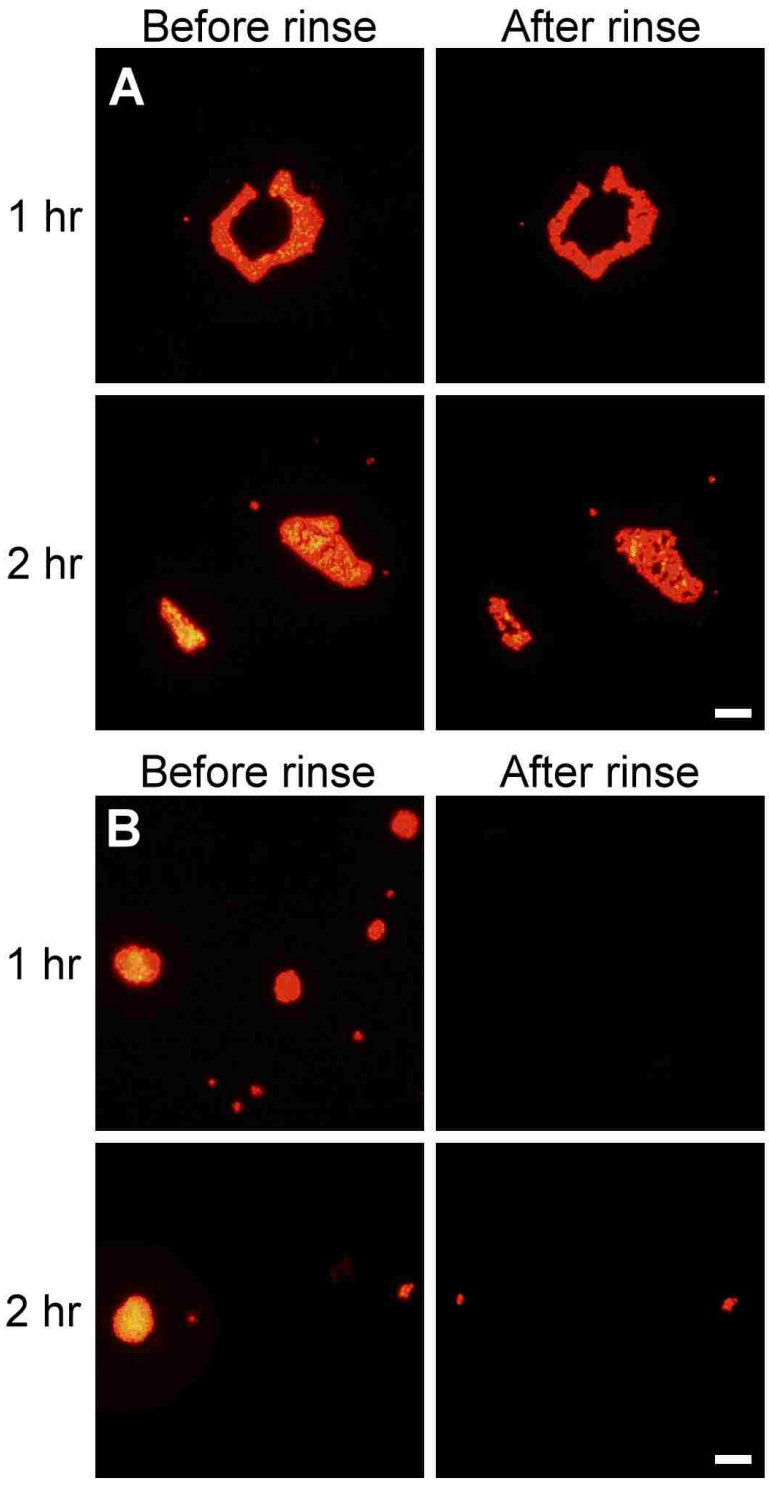

Figure S4. Fluorescence microscopy images of *S. cerevisiae* cells (Cyto64 stained, red emission) from a split sample containing (A) cells in water only (control), and (B) cells in water with 2% DMSO (cells under osmotic clamp) introduced to lipid-templated mesoporous silica films. Cells were allowed to integrate for 1 or 2 hours, after which samples were rinsed to remove non-integrated material. Scale bars = 50 μm.

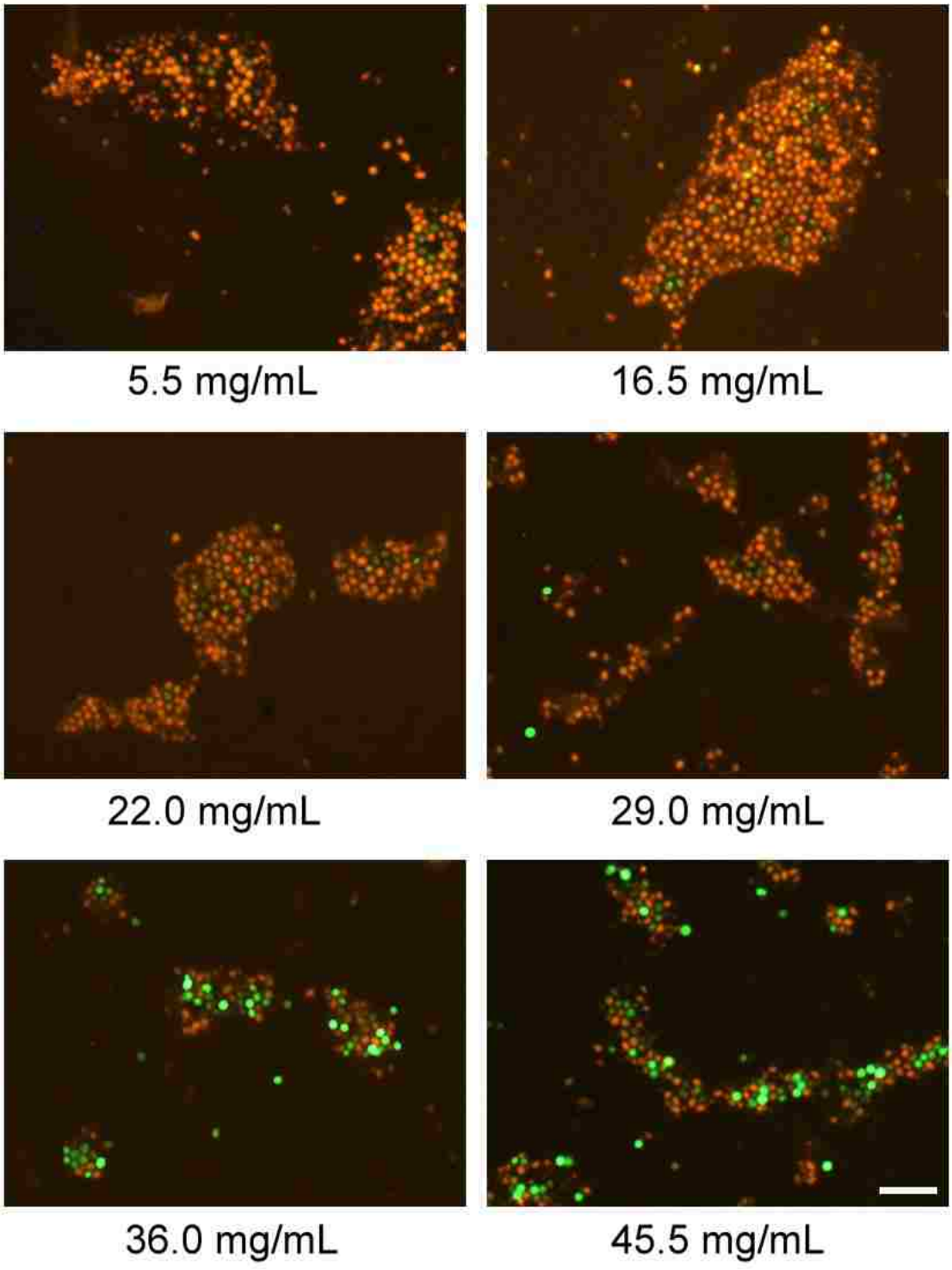

Figure S5. Fluorescence microscopy images of CFDA/PI viability assay treated *S. cerevisiae* cells introduced to trehalose containing lipid-templated mesoporous silica films and stored under dry conditions at room temperature for ~24 hours. Trehalose concentration in the sol precoursor solution used to prepare the films is presented below each image. Green cells are counted as viable. Scale bar = 25 μm.

CHAPTER 2

Cell-Directed Localization and Orientation of a Functional Foreign Transmembrane Protein within a Silica Nanostructure

Carnes, E. C., **Harper, J. C.**, Ashley, C. E., Lopez, D. M.,
Brinker, L. M., Liu, J., Singh, S., Brozik, S. M., Brinker, C. J.

J. Am. Chem. Soc. **2009**, *131*, 14255-14257.

Abstract

A simple procedure is described for introducing functional exogenous membrane bound proteins to viable cells encapsulated within a lipid templated silica nanostructure. In one method, bR was added directly to a *S. cerevisiae* solution along with short zwitterionic diacylphosphatidylcholines (*di*C_6 PC), and mixed with equal volumes of a sol precursor solution. Alternatively, bR was first incorporated into liposomes (bR-proteoliposomes) and then added to a *S. cerevisiae* solution with *di*C_6 PC, followed by mixture with sol precursor solution. Films prepared from bR added directly with *di*C_6 PC resulted in bR localization near *S. cerevisiae* cells in a disordered and diffuse fashion, while films prepared from bR-proteoliposomes added to the *di*C_6 PC/yeast solution resulted in bR preferentially localized near yeast cell surfaces forming bR containing multilayer vesicles. Importantly, bR introduced via proteoliposomes was observed to modulate pH gradients developed at the cell surface, demonstrating both retained functionality and preferential orientation. Localization of liposome lipid or bR did not

occur around neutrally charged latex beads acting as cell surrogates, demonstrating that living cells actively organize the multilayered lipid during evaporation-induced self-assembly. We expect this simple procedure for introducing functional and oriented membrane-bound proteins to the surface of cells to be general and adaptable to other membrane-bound proteins. This advance may prove useful in fundamental studies of membrane protein function, cell-cell signaling, and in imparting non-native characteristics to arbitrary cells.

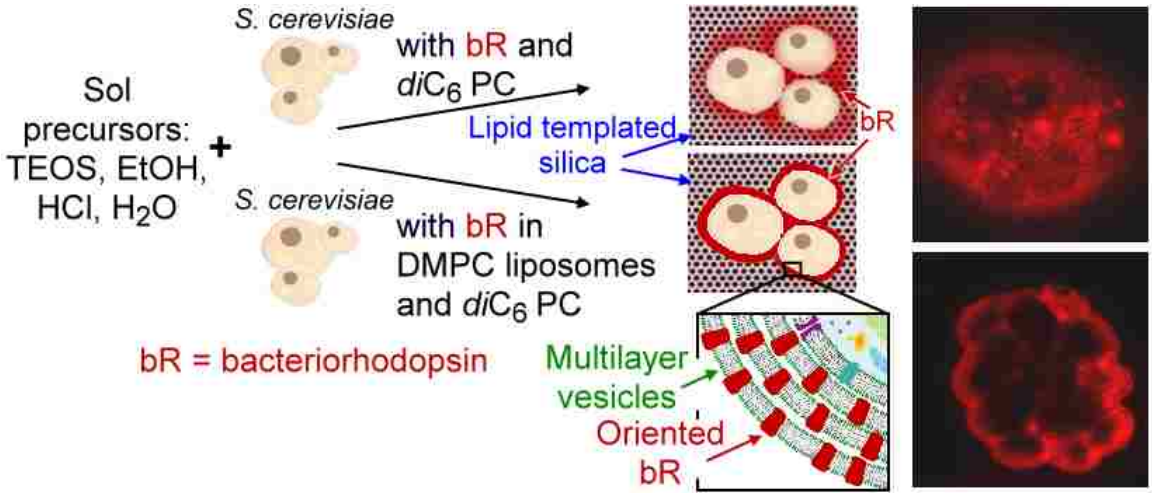

Abstract Figure

INTRODUCTION

The development of new material behaviors based on incorporation of stable and functional biomolecules has attracted considerable interest due to potential applications in biotechnology, biocatalysis, drug delivery, bio-electronic devices, and biological sensing.[1] Recently, the use of sol-gel technology for immobilization of functional soluble proteins in inorganic materials has been widely reported. This success is largely due to advances in sol-gel processing that reduce exposure of biological components to alcohol solvents, toxic by-products, and the highly acidic or basic conditions of hydrolysis.[2] Similar advances in the development of biocompatible sol-gel processes have also permitted the encapsulation of viable cells.[3] The extension of these biologically compatible sol-gel processing techniques to encapsulate more sensitive membrane-bound proteins in sol-gel matrices remains a significant challenge.[4] The relatively few successful reports of membrane protein encapsulation mostly utilize the photoactive protein-retinal complex, bacteriorhodopsin (bR). This prior work demonstrated that bR retained native photo-induced proton pumping functionality, but that this function was rather inconsequential as the proteins were randomly oriented and therefore could not yield useful ion gradients.[5] Specific orientation of bR in sol-gel matrices was recently shown, using silica entrapped bR-proteoliposomes (liposome reconstituted bR) to produce proton gradients that facilitated ATP synthesis,[6] or by intercalation of silica between oriented sheets of intact purple membrane lipid bilayers, which when integrated on an electrode, produced measurable photocurrents.[7]

We recently reported that, using short chain phospholipids to direct the formation of thin film silica nanostructures during evaporation-induced self-assembly[8] (EISA), the introduction of cells alters profoundly the inorganic self-assembly pathway. Cells actively organize around themselves an ordered, multilayered lipid-membrane that interfaces coherently with a 3D lipid-templated silica nanostructure. This bio/nano interface is unique in that it withstands drying (even evacuation) maintaining cell viability for days to years without external buffer, yet remains accessible to molecules, proteins/antibodies, plasmids, etc. introduced into the 3D silica host.[9] Herein we report an extension of this cell directed assembly approach where bR is oriented within a multilayered lipid membrane localized at the interface between *S. cerevisiae* and the surrounding lipid-templated silica matrix. To the best of our knowledge this is the first report detailing incorporation of both functional transmembrane bacterial proteins and viable cells in a sol-gel material. Importantly, the bR is observed to modulate pH gradients developed at the cell surface, demonstrating both orientation and retained functionality. Such a simple procedure for introducing functional exogenous membrane bound proteins to immobilized cells may significantly impact fundamental studies of membrane protein function and cell-cell signaling.

RESULTS AND DISCUSSION

The two methods used by us to introduce bR and yeast cells in a lipid-templated silica matrix are depicted in Figure 1 A. In both methods, equal volumes of sol precursors and yeast cells, suspended in phosphate buffer, were mixed (see Supplemental

Information). In one method, bR was added directly to the yeast solution along with short zwitterionic diacylphosphatidylcholines (*di*C_6 PC). Alternatively, bR was first incorporated into dimyristoylphosphatidylcholine (DMPC) liposomes (see Supporting Information) and then added to the yeast solution with *di*C_6 PC. Following mixture of the respective yeast solutions with sol precursors the solution was immediately spin-coated onto a glass substrate. Grazing incidence small angel x-ray scattering (GISAXS) and scanning electron microscopy (SEM) were used to characterize the cell-lipid-protein-silica matrix produced from each of the two methods shown in Figure 1 A. Consistent with our previous studies,[8] films prepared from either method exhibited lamellar structures with repeat distance (d_r) of ~31 Å as a result of the cell-directed assembly process (Figure 1 B). Also consistent with our previous reports, SEM imaging of samples prepared from either method shows *S. cerevisiae* encapsulated in a crack-free silica film with a coherent cell-matrix interface (Figure 1 C).

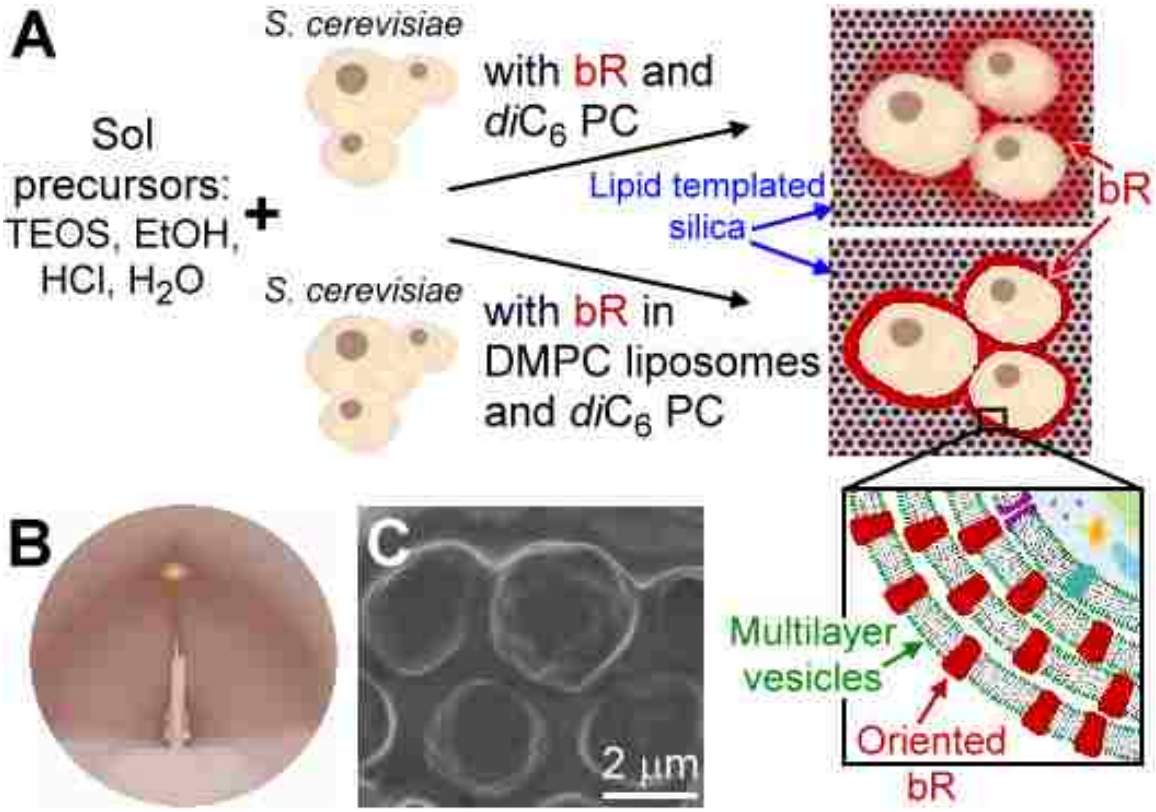

Figure 1. (A) Encapsulation of yeast and bacteriorhodopsin (bR) in mesostructured silica films by direct addition of bR, or addition of bR incorporated into DMPC liposomes, to the yeast/*di*C_6 PC lipid/sol precursor solution. bR added directly with *di*C_6 PC was localized in a disordered and diffuse fashion while bR incorporated into DMPC liposomes and added to the *di*C_6 PC/yeast solution was preferentially localized near the yeast cell surface forming conformal bR containing multilayer vesicles. (B) Grazing incidence small angle x-ray scattering (GISAXS) pattern of lipid-silica matrix encapsulated yeast-bR film showing lamellar structure. (C) SEM image of lipid-silica matrix encapsulated yeast-bR film.

Localization of the protein and various lipid components was monitored by fluorescent labeling and laser-scanning confocal fluorescence microscopy. Pronounced differences were observed in lipid and protein localization near *S. cerevisiae* cells when comparing samples prepared by direct addition of bR or addition of bR-proteoliposomes to the yeast/*di*C_6 PC solution. Figure 2 A shows that upon addition of bR directly to the yeast/*di*C_6 PC solution, bR (red panel) localized near *S. cerevisiae* cells in a diffuse

manner that corresponded closely to the region of *di*C_6 PC localization (green panel). Localization of *di*C_6 PC near yeast cells is consistent with our previous studies which show the formation of a lipid-rich region that interfaces cells with the surrounding nanostructured silica host. Figure 2 B shows that addition of bR-proteoliposomes to the yeast/*di*C_6 PC solution resulted in a more conformal localization of bR (red panel) near *S. cerevisiae* cells. The thickness of the protein layer suggests that multiple fusion steps have occurred during cell-directed assembly, forming yeast supported multilayers containing bR. Figures 2 B and 3 A show that longer chain lipids introduced as liposomes with (Fig. 2 B) or without (Fig. 3 A) bR preferentially localize at yeast cell surfaces during cell-directed assembly. In Figure 2 B preferential localization of NBD labeled longer chain palmitoyloleoyl phosphatidylcholine (POPC) (introduced as 1% of the total liposome lipid, green panel) is clearly shown by the 4-5 cells in which the confocal slice includes the top portion of the cells (peripheral cells). Based on additional cell-directed assembly experiments performed with labeled liposomes and labeled *di*C_6 PC (e.g. Fig. 3 A), we propose that bR introduced in proteoliposomes is co-localized with both the longer chain liposomal lipids and the shorter chain lipids in close proximity to the cell surface, but that the bR and liposomal lipids have higher priority to and are more conformal with the cell surface.

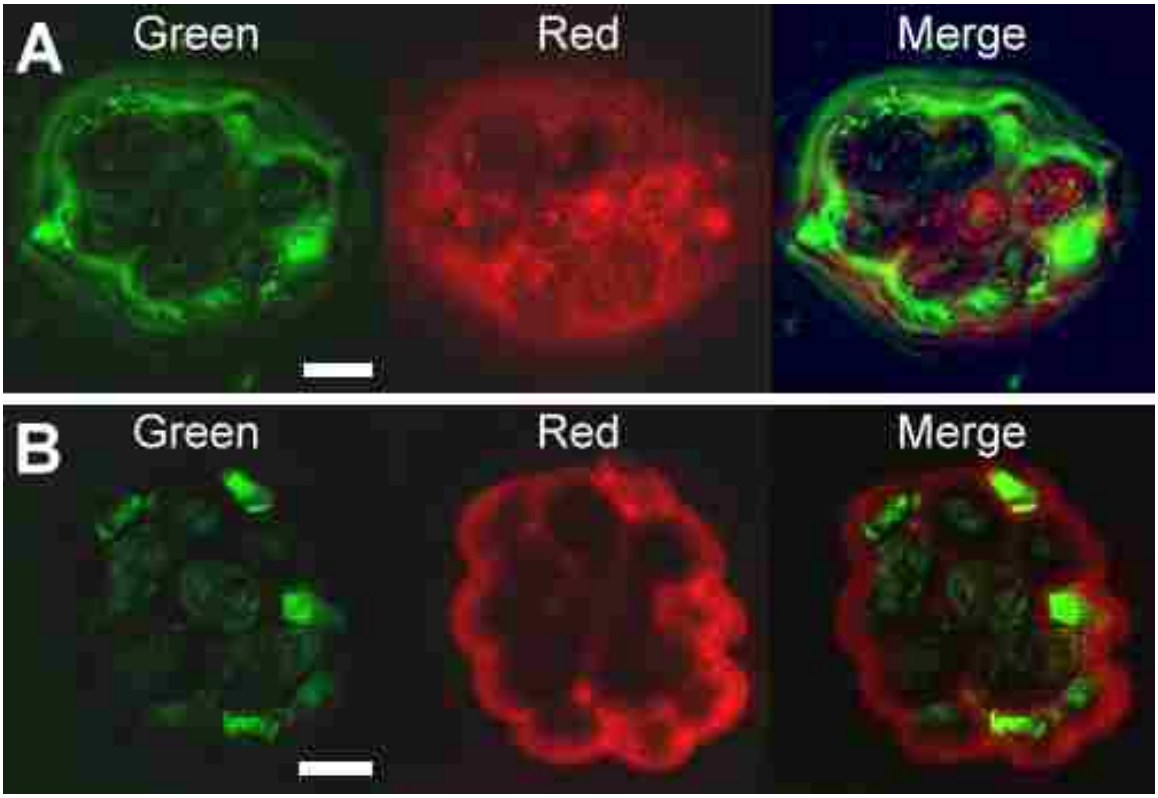

Figure 2. Confocal fluorescence images of Alexa Fluor 594 labeled bR (red emission) localized near yeast cells in the surrounding lipid-silica matrix. (A) bR added with *di*C_6 PC only (1% NBD labeled *di*C_6 PC, green emission) to yeast. (B) bR incorporated in DMPC liposomes (1% NBD labeled POPC, green emission) added with *di*C_6 PC to yeast. Scale bars = 3 μm.

The importance of evaporation-induced cell-directed assembly in forming yeast supported bR multilayers is evidenced by the lack of spontaneous liposome fusion or lipid association around yeast cells in buffered solutions. In these control experiments, yeast and POPC liposomes (6% Texas Red labeled DHPE) were mixed, with and without *di*C_6 PC, in buffered solutions prepared at various pH values: pH 7, (pH of the initial bR-proteoliposome/yeast/*di*C_6 PC solution prior to adding sol precursors), pH 2 (pH of the silica precursor solution), or pH 5 (pH obtained near the lipid/silica encapsulated cells following cell-directed assembly). In each case, no liposome fusion nor lipid association

with yeast cells was observed showing that neither electrostatic effects under the pH range studied nor the presence of *di*C_6 PC, induce liposome fusion with the yeast cells in solution. POPC liposome fusion and multilayer formation around yeast cells was observed, however, when liposomes were added to a yeast/*di*C_6 PC/sol precursor solution and spin-coated onto a cover glass. As shown in Figure 3 A, during evaporation-induced cell-directed assembly both the longer chain liposome lipid (6% Texas Red labeled DHPE, red panel) and shorter chain *di*C_6 PC lipid (1% NBD labeled, green panel) are localized at the cell surface, but the longer chain lipid is more conformal and has greater priority for the cell surface (merged image). Additionally, it is important to note that viable cells play an active role in formation of yeast supported bR multilayers. In control experiments using neutrally charged latex beads as cell surrogates, neither localization of liposome lipid (Figure 3 B) nor bR (Figure 3 C) occurred upon evaporation.

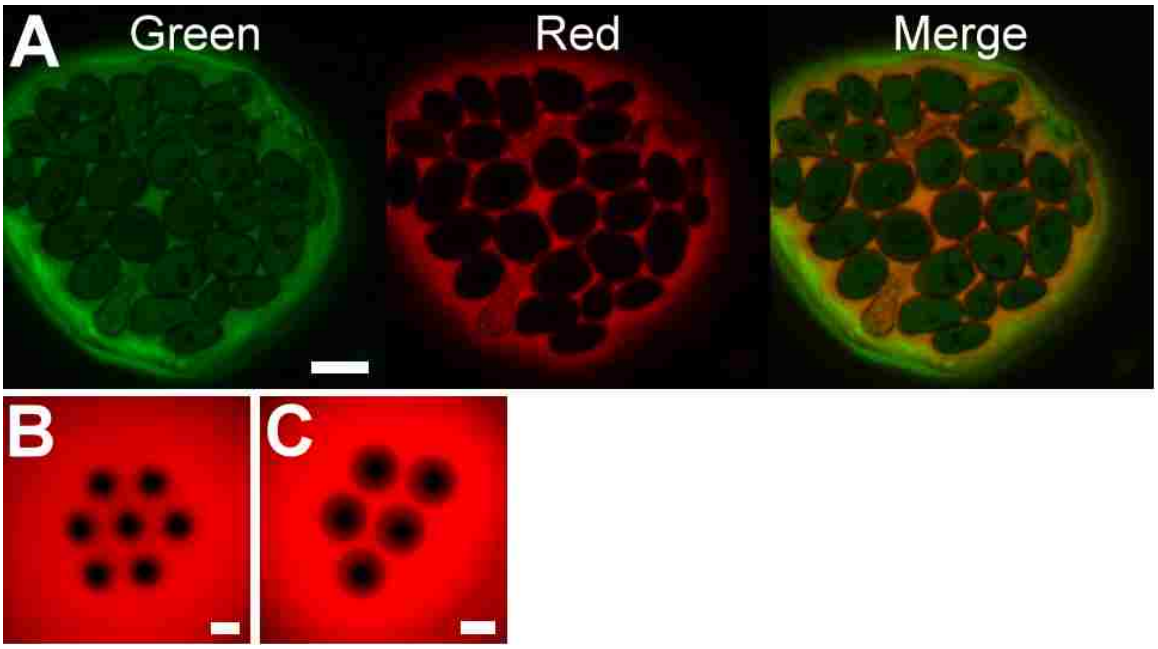

Figure 3. (A) Confocal fluorescence image showing liposome fusion and multilayer formation around yeast cells during cell-directed assembly. POPC liposomes (6% Texas Red labeled DHPE, red emission) were added to a yeast/*di*C_6 PC (1% NBD labeled, green emission)/sol precursor solution. (B-C) Confocal projections of cell surrogates (neutrally charged latex beads) added to the *di*C_6 PC/sol precursor solution showing (B) POPC liposomes (2.5% Texas Red labeled DHPE) and (C) Alexa Fluor 594 labeled bR in DMPC liposomes are not localized. Scale bars = 3 μm.

The ability to generate a photo-induced proton gradient in the lipid-protein-cell-silica matrix was investigated using the membrane impermeant pH sensitive fluorescent dye, Oregon Green. As shown in Figure 4 A, the intensity of fluorescent emission decreases as the pH is lowered from approximately pH 6 to 3 with total quenching of fluorescence at highly acidic pH (≤ 2). The pH gradient resulting from exposure of the films to green light[10] is shown using confocal z-axis projections in Figure 4, B-D. As we have previously shown, encapsulated cells form a gradient in pH from approximately pH 3 in the acidic silanol-terminated silica matrix, to pH 5.5 at the encapsulated cell surface, spanning a distance of several micrometers. Figure 4 B shows that a film prepared from

addition of DMPC liposomes (without bR) to the yeast/*di*C_6 PC lipid solution and exposure of the film to green light (see Supplemental Information) yielded similar pH gradients with pH near 5 at cell surfaces decreasing to approximately pH 3 over a few micrometers. Photo-induced proton pumping was observed in samples prepared from direct addition of bR to the yeast/*di*C_6 PC solution (Figure 4 C) which shows a slight decrease in pH to 4.5 at the cell surface, as shown by the reduced intensity of the Oregon Green dye compared to Figure 4 B. This slight decrease in pH is indicative of non-functional and/or randomly oriented bR, as functionality requires a lipid bilayer that can accommodate the hydrophobic domains of the transmembrane protein.

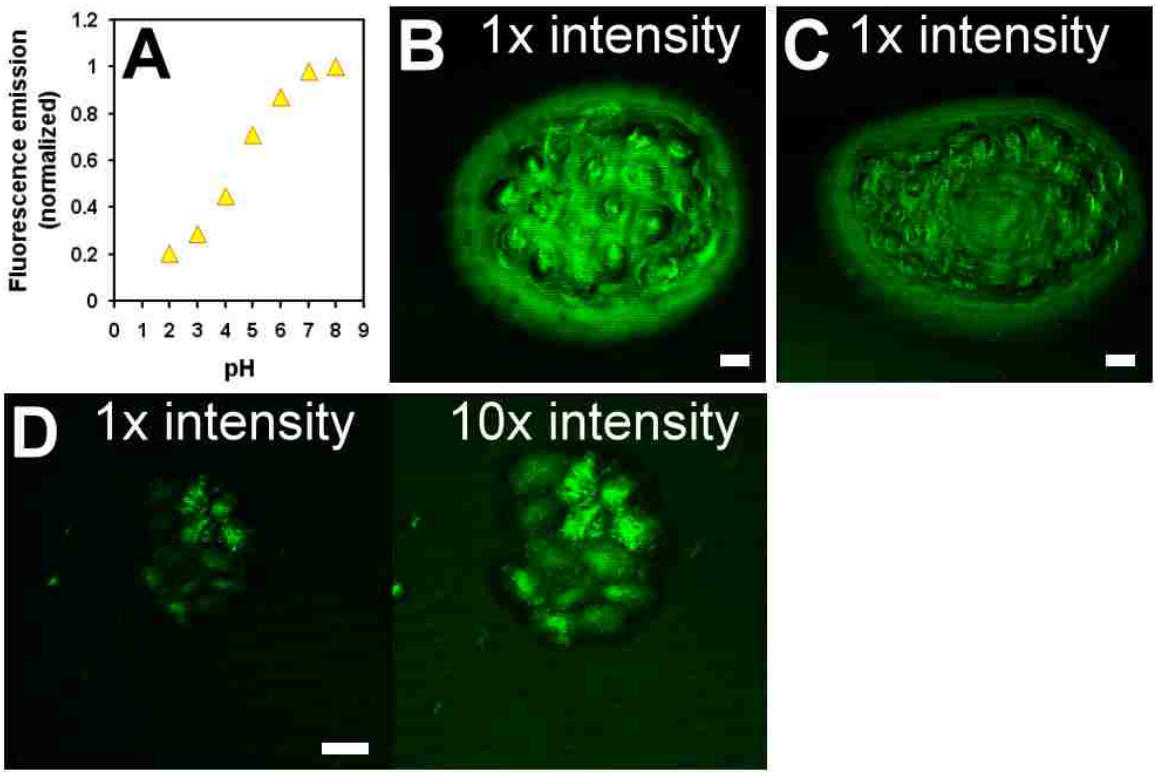

Figure 4. (A) Dependence of the fluorescence emission of the pH sensitive probe, Oregon Green, on pH. (B-D) Confocal projections comparing development of pH gradients using Oregon Green in mesostructured silica encapsulated yeast with: (B) DMPC liposomes without bR, with *di*C_6 PC, (C) bR added with *di*C_6 PC only, and (D) bR added in DMPC liposomes with *di*C_6 PC. Decreasing fluorescence intensity corresponds to decreasing pH. Scale bars = 3 μm.

Dramatic changes in pH gradient are observed for samples prepared from addition of bR-proteoliposomes to the yeast/*di*C_6 PC solution. As shown in Figure 4 D, the original several micrometer region of higher pH surrounding encapsulated cells is no longer present. Increasing fluorescence intensity by 10 fold (Fig. 4D) shows that the region surrounding the cells containing bR is now similar in pH to the surrounding silica matrix, ~ pH 3-4, consistent with proton pumping toward the cell. Unfortunately, due to the strongly overlapping spectral windows of Oregon Green emission and bR absorption and activation (Figures S1 and S2) attempts to image the initial pH gradient were

unsuccessful – confocal imaging unavoidably stimulates proton pumping eradicating the initial pH gradient. However, it is clear that the Oregon Green dye penetrates the multilayer vesicle region, retaining its capability to probe pH near the yeast cells, and does not photobleach significantly over the course of these experiments, as shown by the bright green emission in Figure 4 B where bR is absent. (Further addition of exogenous buffer (pH 7.0) caused immediate uniform green emission throughout the matrix). The decrease in pH of approximately 2 units over the typically 15 minutes required to locate cells and obtain the confocal projection is similar to that previously reported for bR reconstituted in porous silica microsphere supported bilayers.[11] In that study, after a 60 minute exposure of the 10 μm diameter microspheres to a UV-filtered xenon lamp, a 1.5 pH unit change was observed and attributed to bR orientation on the microsphere surface driven by fusion of unidirectional aligned bR proteoliposomes with the microsphere.[11] For our system, the comparatively smaller volume of the lipid-protein-encapsulated cells (>37x smaller for ~3 μm diameter yeast cells than for microspheres) and higher intensity of the laser light are consistent with a moderately greater pH change over a shorter time period.

These results show that bR retain their native functionality and adopt a preferred orientation to the yeast cellular surface when introduced in proteoliposomes with *di*C_6 PC. It has been shown that bR inserts unidirectionally into preformed liposomes under conditions of detergent saturation.[12] *di*C_6 PC may act as a detergent that, upon EISA and cell-directed assembly, reaches saturated concentration near the cells. This causes destabilization of the co-localized bR-proteoliposomes, facilitating fusion of liposomes with other liposomes and unidirectional orientation of bR.[12] This thesis is supported by

the lack of liposome fusion or bR localization near neutrally charged latex beads (Figure 3 B,C) which we have shown do not localize *di*C_6 PC under evaporation-induced cell-directed assembly.[8] The inside-out orientation of bR reported in this work is identical to the bR orientation reported for bR-proteoliposomes formed in the presence of saturating detergent. Additionally, the proposed mechanism that proteins always insert through the hydrophobic domain of the membrane with the more hydrophobic protein moiety[13] is followed by this system where the more hydrophobic NH_2-terminal region of bR penetrates the yeast supported multilayers yielding an inside-out orientation.

CONCLUSIONS

In summary, we have shown a simple method for interfacing and orienting functional exogenous membrane-bound proteins with cells. We expect that this method is general and can be adapted to other membrane-bound proteins. It may prove useful in fundamental studies of membrane protein function and in imparting non-native characteristics to arbitrary cells.

References

(1) (a) Avnir, D.; Coradin, T.; Lev, O.; Livage, J. *J. Mater. Chem.* **2006**, *16*, 1013-1030. (b) Hartmann, M. *Chem. Mater.* **2005**, *17*, 4577-4593. (c) Ispas, C.; Sokolov, I.; Andreescu, S. *Anal. Bioanal. Chem.* **2009**, *393*, 543-554. (d) Lee, M.-Y.; Park, C. B.; Dordick, J. S.; Clark, D. S. *Proc. Natl. Acad. Sci. USA* **2005**, *102*, 983-987.

(2) (a) Braun, S.; Rappoport, S.; Zusman, R.; Avnir, D.; Ottolenghi, M. *Mater. Lett.* **1990**, *10*, 1-5. (b) Ellerby, L. M.; Nishida, C. R.; Nishida, F.; Yamanaka, S.; Dunn, B.; Valentine, J. S.; Zink, J. I. *Science* **1992**, *255*, 1113-1115. (c) Yi, Y.; Neufeld, R.; Kermasha, S. *J. Sol-Gel Sci Technol.* **2007**, *43*, 161-170.

(3) (a) Nassif, N. Bouvet, O.; Rager, M. N.; Roux, C.; Coradin, T.; Livage, J. *Nat. Mater.* **2002**, *1*, 42-44. (b) Carturan, G.; Dal Toso, R.; Boninsegna, S.; Dal Monte, R. *J. Mater. Chem.* **2004**, *14*, 2087-2098. (c) Amoura, M.; Nassif, N.; Roux, C.; Livage, J.; Coradin, T. *Chem. Commun.* **2007**, 4015-4017.
(4) Brennan, J. D. *Acc. Chem. Res.* **2007**, *40*, 827-835.
(5) (a) Wu, S.; Ellerby, L. M.; Cohan, J. S. Dunn, B.; El-Sayed, M. A.; Valentine, J. S.; Zink, J. I. *Chem. Mater.* **1993**, *5*, 115-120. (b) Weetall, H. H.; Roberston, B.; Cullin, D.; Brown, J.; Walch, M. *Biochim. Biophys. Acta* **1993,** *1142*, 211-213. (c) Weetall, H. H. *Biosens. Bioelectron.* **1996**, *11*, 327-333. (d) Shamansky, L. M.; Luong, K. M.; Han, D. H., Chronister, E. L. *Biosens. Bioelectron.* **2002**, *17*, 227-231.
(6) Luo, T. J. M.; Soong, R.; Lan, E.; Dunn, B.; Montemango, C. *Nat. Mater.* **2005**, *4* 220-224.
(7) Bromley, K. M.; Patil, A. J.; Seddon, A. M.; Booth, P.; Mann, S. *Adv. Mater.* **2007**, *19*, 2433-2438.
(8) Baca, H. K.; Ashley, C.; Carnes, E.; Lopez, D.; Flemming, J.; Dunphy, D.; Singh, S.; Chen, Z.; Liu, N. G.; Fan, H. Y.; Lopez, G. P.; Brozik, S. M.; Werner-Washburne, M.; Brinker, C. J. *Science* **2006**, *313*, 337-341.
(9) Baca, H. K.; Carnes, E.; Singh, S.; Ashley, C.; Lopez, D.; Brinker, C. J. *Acc. Chem. Res.* **2007**, *40*, 836-845.
(10) (a) Birge, R. R. *Biochim. Biophys. Acta* **1990**, *1016*, 293-327. (b) Saaem, I.; Tian, J. *Adv. Mater.* **2007**, *19*, 4268-4271.
(11) Davis, R. W; Flores, A.; Barrick, T. A.; Cox, J. M.; Brozik, S. M.; Lopez, G. P.; Brozik, J. A. *Langmuir* **2007**, *23*, 3864-3872.
(12) Rigaud, J.-L.; Paternostre, M.-T.; Bluzat, A. *Biochemistry* **1988**, *27*, 2677-2688.
(13) Eytan, G. D. *Biochim. Biophys. Acta* **1982**, *694*, 185-202.

SUPPLEMENTAL INFORMATION

Methods and Materials

All chemicals used in this work were supplied by Aldrich unless otherwise noted. *S. cerevisiae* (strain S288C, Invitrogen) was grown in glucose-based rich medium (YPD+A) to G0 or stationary state. Cells were collected by centrifugation, washed 3 times in DI water, and resuspended in DI water.

Silica precursor solutions were prepared as described previously [1]. Briefly, precursor solutions were prepared by adding phospholipids to polymeric silica sols in a two step procedure designed to reduce siloxane condensation, avoiding kinetic barriers to silica-lipid supramolecular self-assembly during film deposition. Pre-hydrolyzed TEOS stock solutions ($A2^{**}$) were prepared by refluxing TEOS, ethanol, de-ionized water and HCl (molar ratios 1: 4: 1: $5x10^{-5}$) for 90 minutes at 60°C. Stock solutions were stored at -20°C. A2** stock was used to prepare the precursor sol solution with molar ratio of 1 TEOS: 4.0 ethanol: 2.0 water: 0.005 HCl.

A second solution was prepared containing the lipid 1,2-Dihexanoyl-*sn*-Glycero-3-Phosphocholine (*di*C_6 PC, Avanti Polar Lipids) at a concentration of 30mg/mL, with yeast cells in DI water, with fluorescently labeled NBD-*di*C_6 PC (1-hexanoyl-2-{6-[(7-nitro-2-1,3-benzoxadiazol-4-yl)amino]hexanoyl}-*sn*-glycero-3-phosphocholine, Avanti Polar Lipids) at 1 wt%, as appropriate. After dissolution of the lipid, 1 wt% bacteriorhodopsin, 1 wt% liposomes, and/or 50 µM fluorescent pH probe 2', 7'-difluorofluorescein [Oregon Green™ 488] (Invitrogen) were added as appropriate to the lipid/yeast mixture. This solution was then mixed with the silica precursor solution in

equal volume ratios and immediately deposited onto 25 mm No. 1.5 round glass coverslips which had been pretreated in 0.1 M KOH for 2 hours, washed with 1% Alconox in DI water, rinsed in DI water, and then cleaned in a UVO cleaner (Jelight model 342) for 5 minutes. The deposited solution was then spun at 1500 rpm for 30 seconds using a spincoater (Laurell model WS-400B) held at <20% RH.

Bacteriorhodopsin (Sigma) was dissolved in 1x PBS, pH 7.2 at a concentration of 1 mg/mL and fluorescently labeled via reaction with Alexa Fluor 594 carboxylic acid succinimidyl ester (Invitrogen) for one hour at room temperature. Excess dye was removed using an Amicon Ultra-4 centrifugal filter with a 10 kDa MWCO (Millipore). Palmitoyloleoyl phosphatidylcholine (POPC) and dimyristoylphosphatidylcholine (DMPC, both from Avanti Polar Lipids) were dissolved in chloroform, dried, and maintained overnight under vacuum to remove residual solvent. 2.5 mg of lipid was dissolved in 0.5x PBS, sonicated briefly, and extruded through a 100-nm filter (Millipore) ten times. Texas Red DHPE (Invitrogen) or NBD labeled POPC (Avanti Polar Lipids) at 1-6 wt%, and Alexa Fluor 594-labeled bacteriorhodopsin was added to DMPC at a weight ratio of 10:1 (lipid : bR).

Characterization

A Hitachi S-5200 scanning electron microscope (SEM) equipped with an Energy Dispersive Spectrometer (EDS) from Princeton Gamma Tech (PGT) was used in both spotlight and mapping modes to image the cells interfaces and perform elemental analysis for films on silicon substrates. Fluorescence microscopy was performed with a NIKON

Eclipse 600 or TE2000U with 75W Xenon lamp. Images were acquired with a Hi-QE color CCD camera and Photometrics Hi-mono quantitative fluorescence camera. Confocal microscopy was performed with a BioRad Laser Scanning Microscope (LSM) using a NIKON TE2000U inverted microscope, and a Zeiss LSM 510 Meta system mounted on a Axiovert 100 inverted microscope.

Supporting Information References

1. Baca, H.K. et al. Cell-directed assembly of lipid-silica nanostructures providing extended cell viability. Science **2006**, *313*, 337-341.

CHAPTER 3

Encapsulation of *S. cerevisiae* in Poly(glycerol) Silicate Derived Matrices: Effect of Matrix Additives and Cell Metabolic Phase on Long–Term Viability and Rate of Gene Expression

Harper, J. C., Lopez, D. M., Larkin, E., Economides, M. K., McIntyre, S. K., Alan, T. M., Tartis, M. S., Werner-Washburne, M., Brinker, C. J., Brozik, S. M., Wheeler, D. R.

Chem. Mater., **2011**, *23*, 2555-2564.

Abstract

Bioencapsulation of living cells into silica materials derived from the sol-gel process has resulted in novel hybrid living materials with exciting functionalities. Despite the many successes in this field, long-term viability and activity of the encapsulated cells remain a significant obstacle to producing practical and robust devices, e.g. whole-cell based biosensors. We report the first study on the effects of various media additives and the metabolic phase of encapsulated cells on long-term viability and the rate of inducible gene expression. *Saccharomyces cerevisiae (S. cerevisiae)* cells, genetically engineered to produce yellow fluorescent protein (YFP) in response to galactose, were encapsulated in poly(glycerol) silicate derived matrices. Surprisingly, we find that addition of media components to the glycerol-silica matrix adversely impacted long-term viability in all cases studied, with a 1.3, 1.4, or 5.4 fold decrease in viability after only 9 days of storage in matrices containing yeast peptone dextrose (YPD), yeast peptone (YP, no glucose), or

Synthetic Complete (SC) +2% glucose media, respectively. These findings are consistent with the media components inducing exit of the cells from the more robust quiescent state, and the metabolic production of toxic byproducts. Encapsulated cells from exponential culture exhibited inducible reporter gene expression rates approximately 33% higher than cells from stationary cultures. Addition of media components to the silica matrix increased gene expression rates under certain conditions. These results further elaborate on other silica matrix encapsulated living cell studies, and provide important design parameters for developing effective living cell-based biosensors for case-specific detection applications.

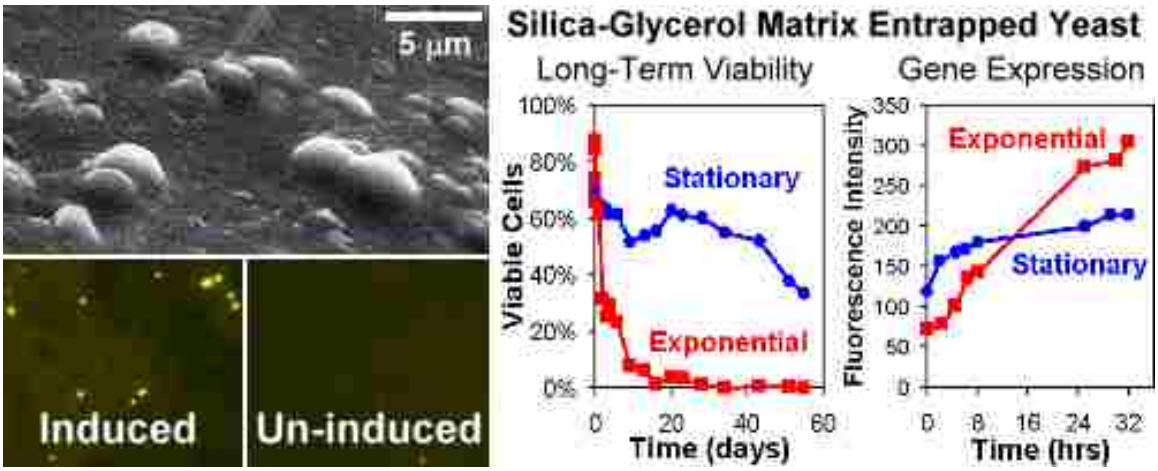

Abstract Figure

INTRODUCTION

The integration of living cells into silica matrixes by the sol-gel process continues to be a challenging field of research that offers many potential opportunities. Numerous researchers have reported the generation of novel hybrid living materials that confer protection to the encapsulated cells, enhance long-term viability, and provide control over bio/nano interfacial properties and the environment local to the cells.[1-7] Such control can provide an instructive background needed to achieve specific functionalities and guide cellular behavior.[8-12] Hybrid living materials with these properties can enable significant advances in biotechnological applications including biosensing, biocatalysis, tissue/organ replacement, environmental and industrial process monitoring, controlled delivery of therapeutics, and bioelectronics.[13-15]

Silica materials derived from sol-gel processing have several differentiating advantages over other polymers used for cellular encapsulation. These include the ability to retain water with negligible swelling, chemical and biological inertness, mechanical stability, controlled porosity, resistance to microbial attack, room temperature preparation, optical transparency, and the ease with which the chemistry of the sol-gel can be varied.[16-18] Indeed, silica is an archetypical cell-protectant in nature. Diatoms, radiolarians, and sponges have evolved to fix silica onto their cell surfaces, forming exoskeletons which can provide mechanical protection without adversely effecting nutrient and waste exchange required for growth.[19]

The high chemical and biological stability and excellent transparency inherent to sol-gel derived silica materials has been leveraged to produce effective silica matrix

entrapped whole cell-based biosensors. In these devices, the intact living cell serves as the active element, exploiting the intrinsic ability of cells to sense their environment and respond to various molecules and stresses. Cell responses are tunable, typically using genetic engineering and signal amplification approaches to produce a detectable signal. For example, Premkumar *et al*.[20, 21] encapsulated *Escherichia coli* (*E. coli*) strains engineered to respond to general toxicity, genotoxicity, and oxidative stress, in tetramethylorthosilicate (TMOS) derived silicate films. Exposure to various toxins was monitored by production of an exogenous bioluminescence. Production of fluorescent proteins by silica entrapped *E. coli* has also been employed for sensing,[22] and a careful study of the advantages/disadvantages of both luminescent and fluorescent systems has been reported.[23] Silica entrapped living cell-based sensors for biochemical oxygen demand (BOD),[24] naphthalene and salicylate,[25] anti-photo system II herbicides,[26] organophosphates,[27] dicyclopropyl ketone,[28] and other physiological stresses[29, 30] have been reported.

Despite these many successes, long-term viability and activity remains a significant obstacle in producing practical and robust living cell-based biosensors. It was recently suggested that adding nutrients to a glycerol containing silica matrix may improve long-term cellular viability.[31] Additionally, the metabolic state of the cell upon encapsulation may also hold importance in viability and sensing activity. Cells from stationary phase cultures are known to be more resistant to stresses that may occur upon encapsulation, while cells from exponential phase cultures are more responsive by way of inducible reporter gene expression,[32] both being vital for effective sensing. A survey of the literature shows that while cells from both exponential and stationary phase cultures

are encapsulated for sensing applications, the impact of cell metabolic state on long-term viability and sensor activity has not been addressed.

Herein, we present what we believe to be the first study investigating the effects of media additives and metabolic phase of silica matrix encapsulated yeast cells on long-term viability and the rate of inducible gene expression. *Saccharomyces cerevisiae* (*S. cerevisiae*), genetically engineered to produce yellow fluorescent protein (YFP) in response to galactose which serves as a model analyte for sensing applications, was encapsulated in sol-gel matrices. These matrices were derived from the hydrolysis of a glycerol orthosilicate with media in which the presence of fermentable carbon and other nutrients was independently varied. Interestingly, we observed that in all cases, *S. cerevisiae* viability was negatively impacted by the presence of a fermentable carbon source, and/or other nutrients in the silica matrix. The presence of nutrients and fermentable carbon had a positive or negative effect on the rate of inducible gene expression that was dependent on the cell metabolic phase and encapsulation time in the silica matrix. Encapsulated cells from exponential phase cultures showed enhanced inducible gene expression while cells from stationary phase cultures showed significantly greater long-term viability. These insights provide valuable design parameters that may facilitate the development of robust and effective silica encapsulated whole-cell based sensors for case-specific applications such as on-line process monitoring or autonomous environmental sensing.

RESULTS AND DISCUSSION

Poly(Glycerol) Silicate (PGS) Synthesis and Characterization

Increasing interest has developed in use of alkoxysilanes modified with diols or polyols for cellular encapsulation due to the attractive properties of these systems including high water solubility (no organic co-solvent required), initiation of hydrolysis and condensation reactions by the addition of water (no requirement of acid or base catalyst), and hydrolysis products that are biocompatible alcohols. Several diol or polyol modified silicates have been reported utilizing ethylene glycol, propane-1,2-diol, or glycerol.[34-36] In studies were diol/polyol modified alkoxysilanes have been used for cellular encapsulation, or in which diols/polyols have been added directly to a silica matrix used for cellular encapsulation, glycerol provided the greatest enhancement in cellular viability.[37, 38] This is attributed to the high osmolarity of glycerol which decreases the activity of water, and can be transported through the cell membrane via aquaglyceroporins, modifying the membrane permeability.[39] Therefore, a recently reported PGS was selected for use in this study that, to the best of our knowledge, has not yet been used for encapsulation of cells.

The starting material for the synthesis of the glycerol derived silicate was similar to that by Khonina *et al*.[33] with the catalyst substitution of titanium isopropoxide for titanium butoxide and a 10 to 1 molar ratio of glycerol to tetraethylorthosilicate (TEOS). One can expect a variety of different isomers to be present including cyclics and potential dimers and other oligiomers. No attempt was made to characterize the exact species present or their ratios. Slight variations in batches as evidenced by different gelation

times (± 10%) can reasonably be attributed to variations in the ratios of species present. Despite attempts to maintain tight control of reactions conditions, these variations likely arise from slight difference in reaction temperature, and additions rates, as well as slight variations in the amount of adventitious water present. We believe that the overall gelation process is not affected to a large extent by these slight variations, and no sensitivity of the entrapped cells to these variations was observed.

The hydrolytic stability of the synthesized PGS was investigated by ^{29}Si solution NMR. Multiple resonances were observed indicating that multiple Q^0 hydrolyzed species exist (major peaks at -82, -83, -84, and -85 ppm and minor Q^1 condensation peaks at -89, -90, and -91 ppm;[40, 41] spectrum presented in the Supporting Information, Figure S1). The degree of condensation of the as synthesized material after 2 months of capped storage at room temperature was 5%. This low degree of condensation is indicative of the relatively high hydrolytic stability of this material when compared to similar materials prepared from alternative methods.[34, 42] Silica gels formed from PGS stocks more than 6 months old exhibited negligible variation in gelation time, mechanical, and optical properties.

Gel Formation

The gelation characteristics of this material as a function of pH, theoretical SiO_2 weight percent, and in the presence of various yeast culture media are presented in Figure 1. Gelation time was defined as the point at which the aqueous buffer-PGS mixture no longer flowed when inverted. Of the ±10% batch to batch gelation time variation, 1-2% is attributed to the somewhat subjective determination of zero flow. An increase in gelation time as the pH decreased, with a sharp increase between pH 2-4, was observed (Figure

1A). This pH range corresponds to the isoelectric and zero charge points of silica and common tetraalkoxysilanes,[43] where silica condensation kinetics are minimized, resulting in longer gelation times. This observation corresponds well with trends observed in other glycol-based systems.[34] The effect of theoretical SiO_2 weight percent on gelation time was also studied by increasing or decreasing the volume percent of the PGS in the silicate-aqueous buffer mixture. As shown in Figures 1A and B, a minimum in gelation time is generally observed between 1.6-2.1 theoretical SiO_2 weight percent (35-50 vol% PGS in 0.1 M sodium phosphate, NaPB). Below this range, the increase in gelation time is attributed to the low concentration of silica in the mixture. The resulting gels also exhibited decreased mechanical integrity (data not shown). Above this range, the increase in gelation time is attributed to the lower relative concentration of the H_2O catalyst.

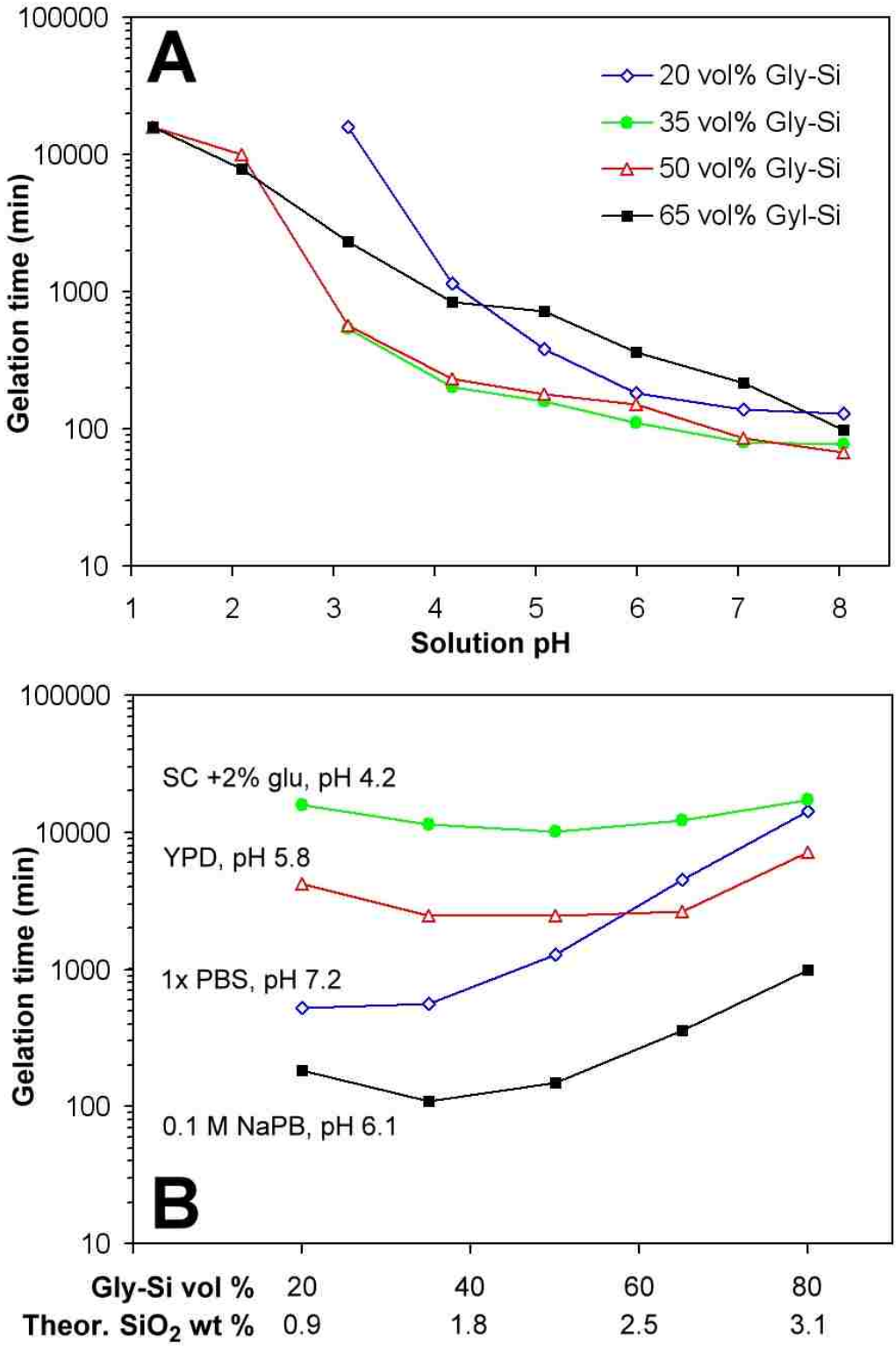

Figure 1. (A) Gelation time following introduction of 20, 35, 50, or 65% (vol.) PGS into buffered solutions at pH 1.21, 2.09, 3.14, 4.17, 5.08, 5.99, 7.05 or 8.05. (B) Gelation time following introduction of 20, 35, 50, 65 or 80% (vol.) PGS into SC +2% glu, YPD, 1x PBS, or 0.1 M NaPB solutions.

The incorporation of yeast culture media, as a general trend, increased gelation time of the PGS as pH decreased (Figure 1B) with a minimum gelation time, again near 1.6-2.1 theoretical SiO_2 weight percent. An exception to these trends is the gelation time of 1× PBS (pH 7.2). Based on the pH trends observed in Figure 1A and the higher ionic concentration of this solution (~0.152 M), it may be expected that 1× PBS would yield similar, if not shorter gelation times than 0.1 M NaPB (pH 6.1). Although the hydrolysis and condensation reactions for common tetraalkoxylsilanes are well understood, little is known regarding the hydrolysis and condensation behavior of glycol modified silianes.[34] This is further complicated by conflicting reports on the impact, or lack thereof, of ionic strength and pH on the gelation of various poly(glycerol) silicate derived sol-gels.[34,44] Based on the results shown in Figure 1, encapsulated cell monoliths were prepared by mixing a 1:1 volume ratio (2.1 theoretical SiO_2 wt%; 50 vol%) of the PGS, with the given medium, pH adjusted to 6.0. This provided a silica gel at a pH amenable to cellular viability, sufficient mechanical integrity, and practical gelation times.

Gel Structural Characterization

The degree of silica condensation for PGS derived gels, with and without cells, was measured using solid state ^{29}Si MAS NMR. Table 1 contains the ^{29}Si NMR spectral data from monoliths formed from 50 vol% PGS in 0.1 M NaPB, pH 6.0, and allowed to age for approximately 25 days. From this data, the degree of condensation (C) for monoliths without *S. cerevisiae* cells, and with *S. cerevisiae* cells, was calculated to be 88.1% and 88.2%, respectively. These results show that although a substantial degree of silica has condensed, condensation was not complete. Furthermore, the chemistry of the

sol-gel system was not extensively changed by the presence of *S. cerevisiae* cells at the concentrations used. Unfortunately, the initial kinetics of the gelation reaction are too fast to accurately observe via ^{29}Si NMR given the long recycle delay required for complete relaxation and large dilution of the silica upon addition of the buffer or buffer/cell suspension. Within eight minutes of mixing, the Q^0 sites of the original material had decreased to 10% of their initial intensity, and the very broad condensation Q^1 and Q^2 resonances were visible at low intensities. The initial spectrum of the PGS, and spectra acquired after addition of the buffer solution or buffer solution containing cells, are presented in Figures S2 and S3.

Table 1. Solid state ^{29}Si MAS NMR spectral data for PGS derived silica gels with and without entrapped yeast.[a]

	δ(^{29}Si), ppm	**Relative Integration (%)**
Sol-gel only	-111 Q^4	52
	-101 Q^3	48
Sol-gel with entrapped yeast	-111 Q^4	59
	-102 Q^3	35
	-90.8 Q^2	6

[a] PGS derived gels prepared with 50% (vol.) 0.1 M NaPB, pH 6.0. Spectra collected approx. 25 days post gelation.

The surface morphology of PGS derived gels containing *S. cerevisiae* cells was examined using scanning electron microscopy (SEM). SEM imaging was performed directly (without fixation, supercritical drying, or metal sputtering) on glycerol-silica gel monoliths. Figure 2A shows the typical long range morphology of glycerol-silica gels is

globular, with some regions of disordered porosity visible. Shallowly encapsulated yeast cells are also visible, as shown by the higher magnification image of a small cluster of yeast cells (Figure 2B). These images suggest that the glycerol-silica matrix is not completely homogenous. EDS measurements did not provide any evidence that the globular regions were high in salt or glycerol content; however, phase separation is known to occur in glycerol containing silica matrixes.[34] The formation of a high glycerol and water containing region surrounding cells entrapped in silica matrices has been reported, and that interface has been implicated in improved cellular viability.[31,37] Planar, less-globular surface regions are less frequently observed (Figure 2C). Depressions are also visible in many areas of the sample, and were observed to form as the sample was exposed to the electron beam (compare Figure 2C and 2D, imaging separated by a few minutes). These depressions are likely the result of the collapsing of silica matrix encapsulated yeast cells as the cytosolic fluid evaporates due to local heating from the electron beam.

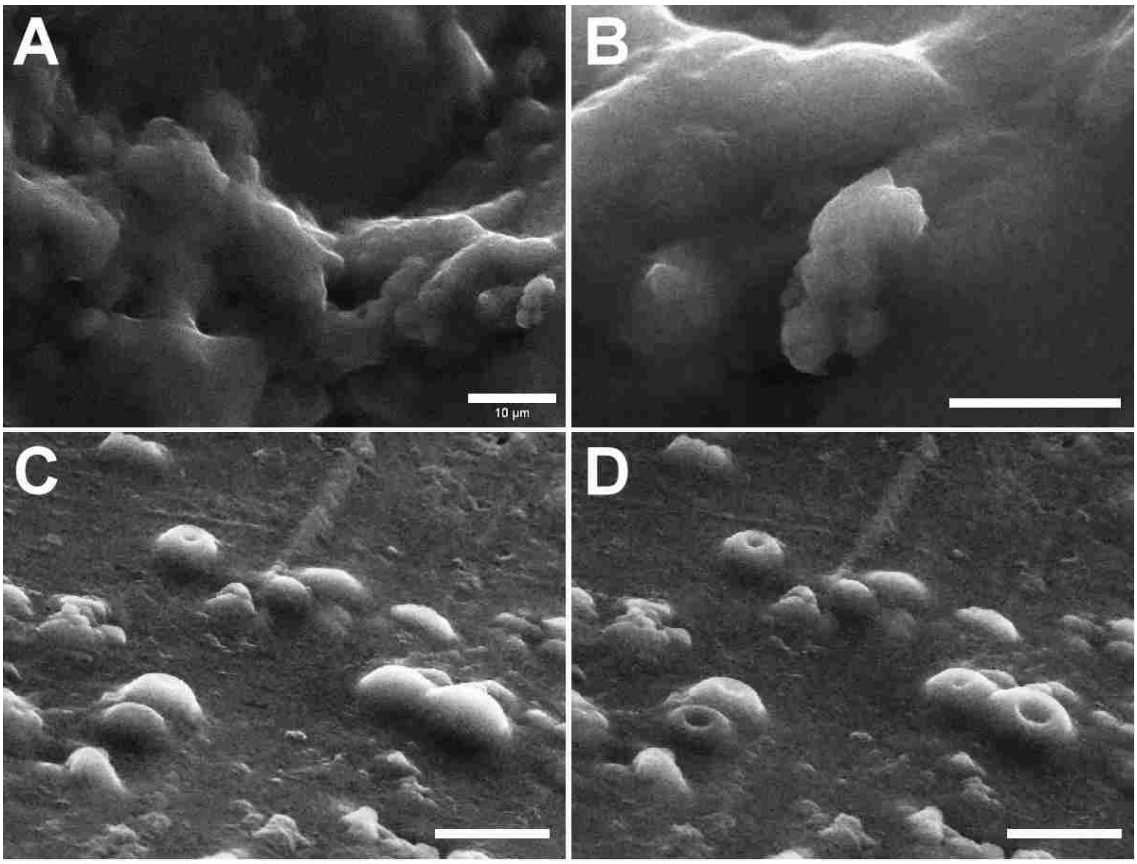

Figure 2. SEM images of PGS derived silica gels containing *S. cerevisiae* cells. (A) Typical long-range morphology with some shallowly encapsulated cells visible (B). Image (D) was collected several minutes after image (C), showing development of depressions during imaging. Scale bars in (B-D) are 5 μm.

Effect of Cell Metabolic Phase and Media Additives on Long-Term Viability

The long-term viability of glycerol-silica gel encapsulated *S. cerevisiae* cells was explored with cell metabolic phase upon encapsulation, and various media component additives to the glycerol-silica matrix, as variables. For cell metabolic phase samples, *S. cerevisiae* cells from exponential phase culture (overnight cultures) and stationary phase culture (8 day old cultures) were used. Cells from these two cultures have significantly different metabolic properties. Cells in exponential phase culture derive their energy from

aerobic fermentation, metabolizing carbon rich glucose via glycolysis, while cells in stationary phase culture have negligible energy requirement. The progression from exponential phase to stationary phase requires two metabolic shifts. Rapidly proliferating cells in exponential culture deplete fermentable carbon and undergo slow carbon starvation. At the diauxic shift, cells change their metabolism to consume ethanol and non-fermentable carbon produced as byproducts of fermentation. A second metabolic shift occurs after all fermentation byproduct carbon is depleted and the cells readjust their metabolism, entering a maintenance-like resting state (quiescence), in which proliferation does not occur and the cells can remain viable without nutrients.[45]

In media additive experiments, the long-term viability of *S. cerevisiae* cells from exponential or stationary phase cultures encapsulated in PGS derived silica matrices containing a fermentable carbon source or other nutrients was studied. Four medium additives were used: a nutrient and fermentable carbon rich media (YPD), a nutrient rich media without fermentable carbon (YP), a nutrient restricted and fermentable carbon rich media (SC +2% glucose), and simple buffer without nutrients or fermentable carbon (0.1 M NaPB). Figure 3A plots the viability of *S. cerevisiae* from exponential phase culture over 56 days of encapsulation in glycerol-silica matrix with various medium. Prior to gelation, cells in PGS-buffer/medium solution and cells from exponential phase culture had similar viabilities measured as 89 ± 2%. Following gelation (~2 hrs for all samples) viability dropped to 66 ± 6%. This loss in viability is attributed to the stresses exerted on the cells during the silica condensation reactions and the ensuing compressive stresses from gelation. Three regions of differing slope in viability are observed following gelation. The first region occurs over the first 2 days after gelation in which a rapid

decline in viability is measured for cells encapsulated in all 4 mediums, resulting in viability between 23-34% after 2 days. This significant loss in viability may correspond to the lower concentration and decreased rate of diffusion of fermentable carbon and/or nutrients through the matrix leading to rapid death for these cells with high metabolic activity. The second region occurs between 2-9 days following gelation. Over this period the viability continues to drop, but at a decreased rate with some minor distinction between cells encapsulated in the 4 mediums. This region may correspond to a small population of cells that could enter the diauxic shift. However, by 9 days post-gelation, viability for all samples decreased to less than 8%. This suggests that the effective concentration of metabolizable carbon was not high enough to permit the slow shift of metabolism from exponential growth, through non-fermentable carbon metabolism, to quiescence. Finally, a third region extending from day 10 to 55 shows little change in viability with all data points between 0-7% viability.

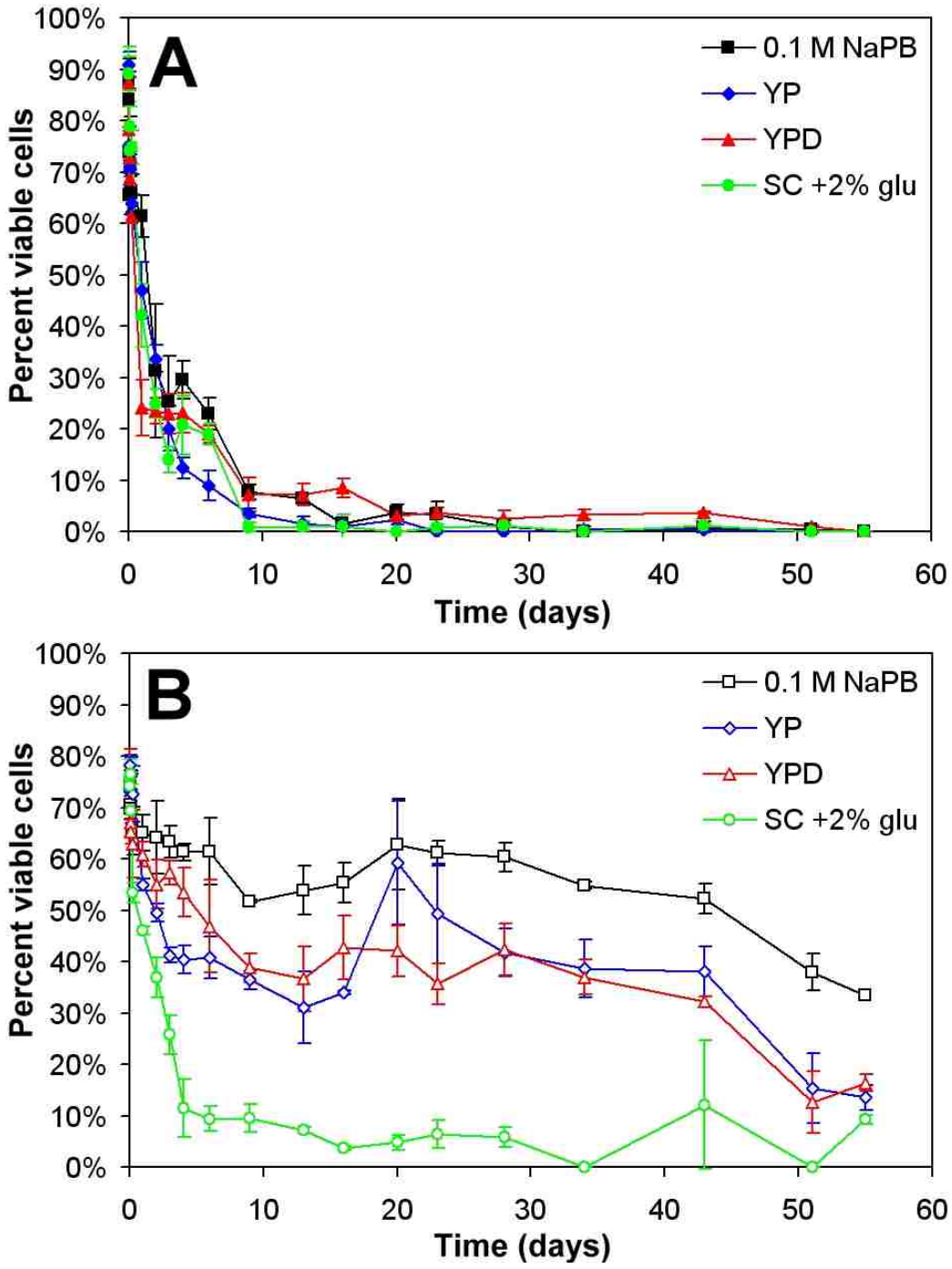

Figure 3. Viability of *S. cerevisiae* cells from (A) exponential culture and (B) stationary culture encapsulated in glycerol-silica gels derived from 50% (vol.) PGS and 50% (vol.) medium that was: nutrient and fermentable carbon rich (YPD, red), nutrient rich without fermentable carbon (YP, blue), nutrient restricted and fermentable carbon rich (SC +2% glu), or without nutrients or fermentable carbon (0.1 M NaPB, black). All mediums were adjusted to pH 6.0. Encapsulated cells stored at room temperature. Viability determined via CFDA/PI assay. Error bars are the standard deviation of measurements from 3 regions of a given sample.

For encapsulated cells from stationary culture (Figure 3B) a decrease in viability post gelation to 64 ± 8%, similar to cells from exponential culture, was measured and attributed to stresses exerted on the cells during gelation. However, viability following gelation was substantially improved. Three regions of differing slope were observed, which are similar between samples with different matrix additives. The first region spanned 1-9 days post-gelation in which the greatest decline in viability was observed. The second region spanned approximately days 9 to 43. Viability in this region was, within experimental error, constant. In the fourth region, 43+ days after gelation, viability declined.

The viability of cells from stationary phase culture in the last three regions depended strongly on the nutrient and fermentable carbon source content of the encapsulation matrix. In control samples, *S. cerevisiae* cells were encapsulated in a glycerol-silica matrix with simple buffer (Figure 3B, black). Viability measured for these cells decreased to 51-61% over the first 1-9 day region. As the matrix lacked both nutrients and fermentable carbon, quiescent cells should remain in that state. We therefore propose that this loss in viability was due to residual syneresis exerting minor compressive stresses that damaged some cells. Additionally, a small population of cells may not have been adequately insulated from the polar chemical groups at the silica surface (i.e. silanols) by the glycerol, slowly leading to damage at the cell/gel interface, inducing cell lysis.[31] From 9-43 days following gelation, control cells viability remained nearly constant between 52-63%. This is slightly higher than the 40-50% viability 1 month post encapsulation that is commonly reported for glycerol containing films. Here, higher viabilities maybe due to the greater glycerol and lower Si content of these gels,

and ensuring the *S. cerevisiae* cells were in stationary phase prior to encapsulation by culturing for 8 days, or a combination of these factors. Typically, post-diauxic shift cultures (~2-4 days from inoculation) are used for encapsulation studies and incorrectly assumed to be in the stationary phase,[45] which may lead to differences from the data reported in this study. Also of note is the similarity of this measured viability to the recently reported 40-50% percent of yeast cells in a stationary phase culture that are truly quiescent, termed 'daughter cells'.[32] These cells are distinct from the remaining nonquiescent 'mother cells'. Finally, a drop in viability was observed 43 days following gelation. This loss in viability may be due to break down of the gel resulting in cell damaging compressive stresses, or exposure of the cell wall to damaging polar groups. Minor expulsion of fluid was observed in some monoliths prepared for the gelation time studies (Figure 1) 2-3 months after gelation.

For cells from stationary phase culture encapsulated in PGS-derived silica matrices containing nutrient and fermentable carbon rich YPD media (Figure 3B, red), viability initially decreased from 62% to ~40% over the first 9 days post-gelation. We propose that this greater decrease in viability, compared to the control sample (black), is due to the quiescent cells sensing the presence of glucose, leading to exit of a subpopulation of the cells from quiescence.[46] However, the relatively low concentration and finite source of glucose is rapidly depleted. These cells may then enter diauxic shift and metabolize the non-fermentable carbon byproducts of fermentation. As the measured viability 9 to 43 days following gelation was between 32-43%, it is evident that addition of this complex media to the matrix resulted in a substantial loss in viability over the control sample. Cells encapsulated with nutrient rich medium without fermentable carbon

(YP, Figure 3B, blue) showed nearly identical viability trends as YPD medium. One exception is the greater rate in loss of viability over the first 9 days following gelation. Like cells exposed to YPD (red), a portion of these cells from stationary phase culture may sense the presence of nutrients in the YP medium and exit quiescence. Glucose in water, in the absence of any other nutrients, is known to induce exit from quiescence.[46] However, it is unknown whether a few key nutrients or other chemical factors that may be present in the yeast extract or peptone can also induce exit from quiescence.[45] Still, as no fermentable carbon source is present, non-fermentable carbon byproducts cannot be generated reducing the likelihood of an effective diauxic shift. Therefore, cells that exit quiescence ultimately die. This results lower viability for these cells between days 1-9, as compared to cells encapsulated with YPD. Still, it would appear that nearly the same population of cells was lost for samples prepared with YP or YPD, indicating that the populations of cells that exit quiescence ultimately cannot return to a quiescent state and die regardless of the presence of a fermentable carbon source.

For nutrient restricted and carbon rich SC +2% glucose media (Figure 3B, green) cell viability rapidly decreased to 11 ± 6% after only 4 days. This loss in viability is much greater than that measured for cells encapsulated with YPD which contained the same concentration of glucose. Although SC media is commonly used in yeast cell culture, it was recently reported that yeast metabolism of SC media leads to formation of an undesirable byproduct, acetic acid, which can negatively impact viability.[47] Under shaken culture conditions, the produced acetic acid is quickly dispersed throughout the culture media, resulting in concentrations that are only moderately detrimental to the yeast cells. However, for silica matrix encapsulated yeast, the effective diffusion rate for the

produced acetic acid is lower than under shaken culture conditions. This results in the development of an acetic acid concentration gradient, with high acetic acid concentrations within close proximity to the cells, leading to a substantial loss in viability. Additionally, the resultant pH gradient could detrimentally affect the surrounding silica matrix causing the cells to sustain additional stresses.

The fluorescence dye viability results (Figure 3) were also confirmed by freeing cells from the silica matrix followed by shaken culture and plating on solid medium. These results are presented in Table 2. Trends in cell viability observed from the culture and plating results were similar to those measured by fluorescence viability dye assay. (Images of colony growth on plates of previously entrapped *S. cerevisiae* cells from exponential and stationary cultures are presented in the Supporting Information, Figures S4 and S5, respectively). These results also demonstrate that encapsulated cells, when removed from the glycerol-silica matrix, remain viable and culturable.

Table 2. Reproductive capability of *S. cerevisiae* removed from glycerol-silica gels with 50% (vol.) medium additives.[a]

		24 hr culture in YPD[2]				48 hr incubation on YPD-Agar[3]			
	Stored for:[1]	2 wks	4 wks	6 wks	8 wks	2 wks	4 wks	6 wks	8 wks
Exponential	0.1 M NaPB	M	X	X	X	L	X	X	X
	YP	H	X	X	X	L	X	X	X
	YPD	L	L	L	X	M	L	L	X
	SC +2% glu	M	L	M	X	L	L	L	X
Stationary	0.1 M NaPB	M	H	H	M	H	M	M	M
	YP	M	H	H	L	M	M	L	L
	YPD	H	M	H	M	H	M	H	H
	SC +2% glu	M	H	H	L	L	M	M	L

[a] All mediums were adjusted to pH 6.0.

[1] Encapsulated cells stored at room temperature.

[2] Optical density (OD) of cultures: high (H; $O.D._{600}$ = 1.6-3.0), moderate (M; $O.D._{600}$ = 1.1-1.5), low (L; $O.D._{600}$ = 0.6-1.0), and none (X; $O.D._{600}$ = 0.0-0.5). Measured values for each sample are reported in the supporting information (Table S1).

[3] Relative number of CFUs: high (H), moderate (M), low (L), and none (X). Images of each sample are provided in the supporting information (Figures S4 and S5).

Surprising, and contrary to what was predicted,[31] in all cases in which media components were added to the matrix, the viability of encapsulated *S. cerevisiae* cells was negatively impacted. This can be rationalized by comparing the viability data for cells from exponential versus stationary culture. For effective long-term viability, *S. cerevisiae* cells should be in the more robust quiescent state. Addition of media induces exit from quiescence and should be avoided to maintain long-term viability. A similar conclusion was drawn by Nassif *et. al.* who showed substantially improved viability for glycerol-silica gel entrapped bacteria following addition of quorum sensing inducer molecules.[48] The authors suggest that these molecules maintain the bacteria in a stationary phase, enhancing their resistance to encapsulation induced stresses.

Inducible Gene Expression

In addition to long-term viability, effective whole-cell based biosensors must recognize a particular analyte and then generate a measurable signal. This is typically done by genetically engineering cells to introduce an exogenous reporter protein that produces a fluorescence, luminescent, or electrochemical signal. Expression of this protein is controlled by selecting a promoter that is induced by either the target analyte itself, or a molecule that is produced as part of a cell signaling pathway activated by the target analyte.[49]

In this work, *S. cerevisiae* cells were engineered to produce yellow fluorescent protein (YFP) in the presence of the model analyte, galactose. The selectivity of this engineered stain for galactose over the monosaccharide epimer, glucose, is shown in

Figure 4. Bright fluorescence was observed for engineered cells treated in shaken culture with YP +gal induction medium (Figure 4A), and for glycerol-silica encapsulated cells treated with YP +gal placed on top of the monoliths (Figure 4C). Engineered cells in shaken culture with YPD medium (Figure 4B), and silica matrix encapsulated cells treated with YPD (Figure 4D) showed very little background fluorescence. This dim fluorescence is often attributed to 'leaky promoter' expression of the recombinant protein. These results show the exceptional selectivity possible with cell-based biosensors. Additionally, fluorescence was observed from cells encapsulated deep within the silica monolith demonstrating that galactose and oxygen can diffuse throughout the glycerol-silica matrix.

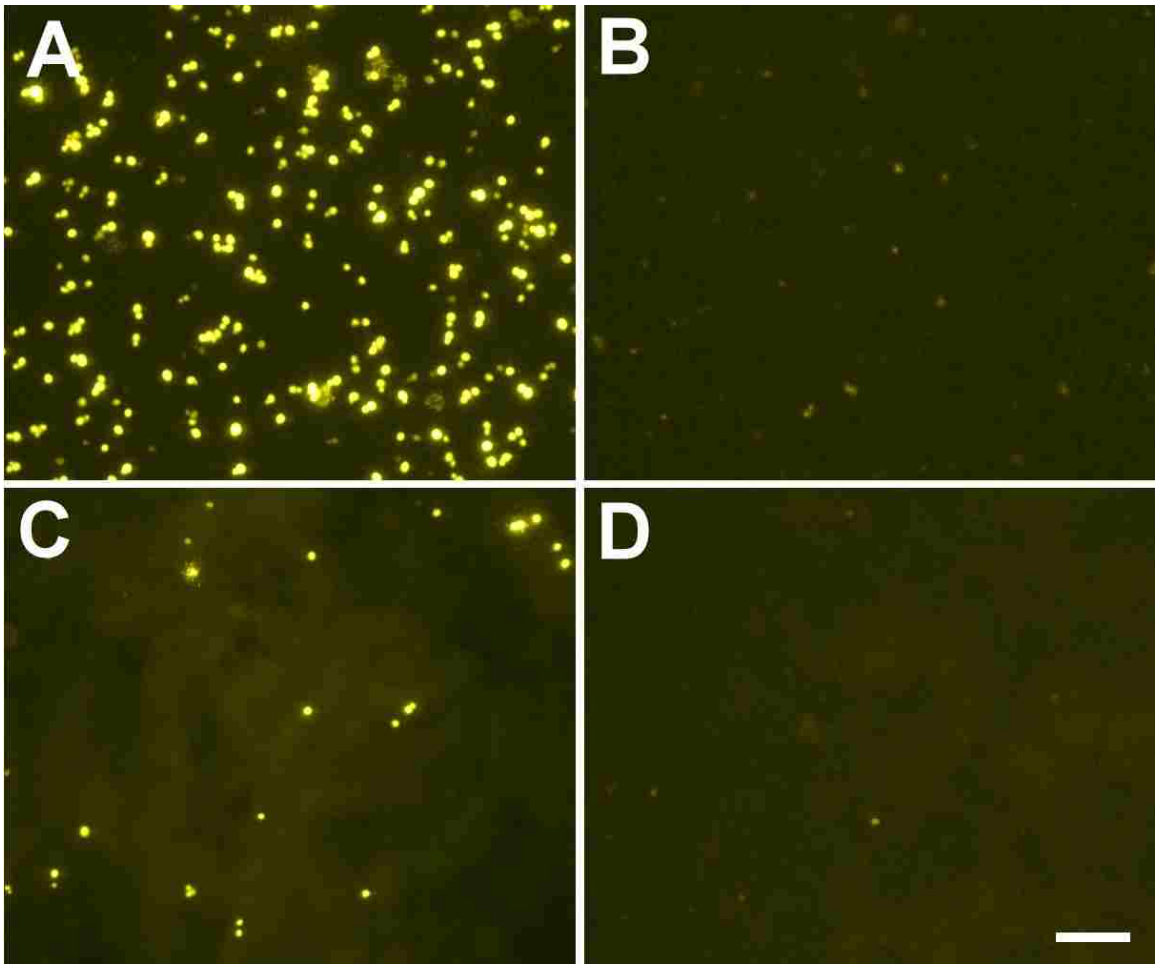

Figure 4. Fluorescence microscopy images (false colored) of YFP expressing *S. cerevisiae* cells in exponential shaken culture (A, B), and cells from exponential culture entrapped in a 1:1 (vol.) matrix of PGS : 0.1 M NaPB, pH 6.0, for 24 hours (C, D). YFP expression was induced (YP +gal treatment overnight at 30 ºC) in (A) and (C). Control uninduced samples (YPD treatment overnight at 30 ºC) are shown in (B) and (D). Cell density in silica matrix samples (C, D) was approximately 25% the density in culture samples (A, B). All images were captured under identical camera settings. Scale bar = 30 μm.

Effect of Cell Metabolic Phase and Media Additives on Inducible Gene Expression

As fluorescence intensity from fluorescent proteins is a function of protein concentration, monitoring intensity over time provides information regarding the rate of expression of the protein. In addition to providing insights into cellular metabolism, the

rate of reporter gene expression is also the governing parameter for response time of the cell-based sensor.

The rate of galactose-induced YFP expression was first monitored for cells in exponential and stationary cultures under shaken or stagnant conditions (Figure 5A,B). Both exponential (Figure 5A) and stationary (Figure 5B) phase cultures show similar trends over a 32 hour period. Shaken culture in induction medium (Figure 5A,B blue points), lead to significant expression of YFP over cells cultured in control medium (Figure 5A,B red points). However, the rate of YFP expression was much greater for *S. cerevisiae* in exponential vs. stationary culture. Development of a fluorescence signal 3σ above the background fluorescence signal (LOD_{Fluor}, see Experimental Section) in the shaken stationary phase culture required nearly 4.5 hours. This signal took less than 2 hours to develop in the shaken exponential phase culture. Although the saturation intensity (25 and 32 hour time points) for both stationary and exponential phase cultures was similar, the initial background fluorescence for cells in stationary culture was higher (avg. 132 ± 6 a.u.) than in exponential culture (avg. 105 ± 22 a.u.), indicative of greater leaky expression for this construct in stationary phase culture. This higher background fluorescence also contributed to the delayed development of a signal greater than the LOD_{Fluor}. Finally, stagnant culture in induction medium (Figure 5A,B green points) showed a significantly lower rate of YFP expression and lower saturation intensity for both exponential and stationary phase *S. cerevisiae* cultures. This is attributed to the lower diffusion rate of the inducer molecule and oxygen required for fluorescence through the stagnant medium to the settled cells.

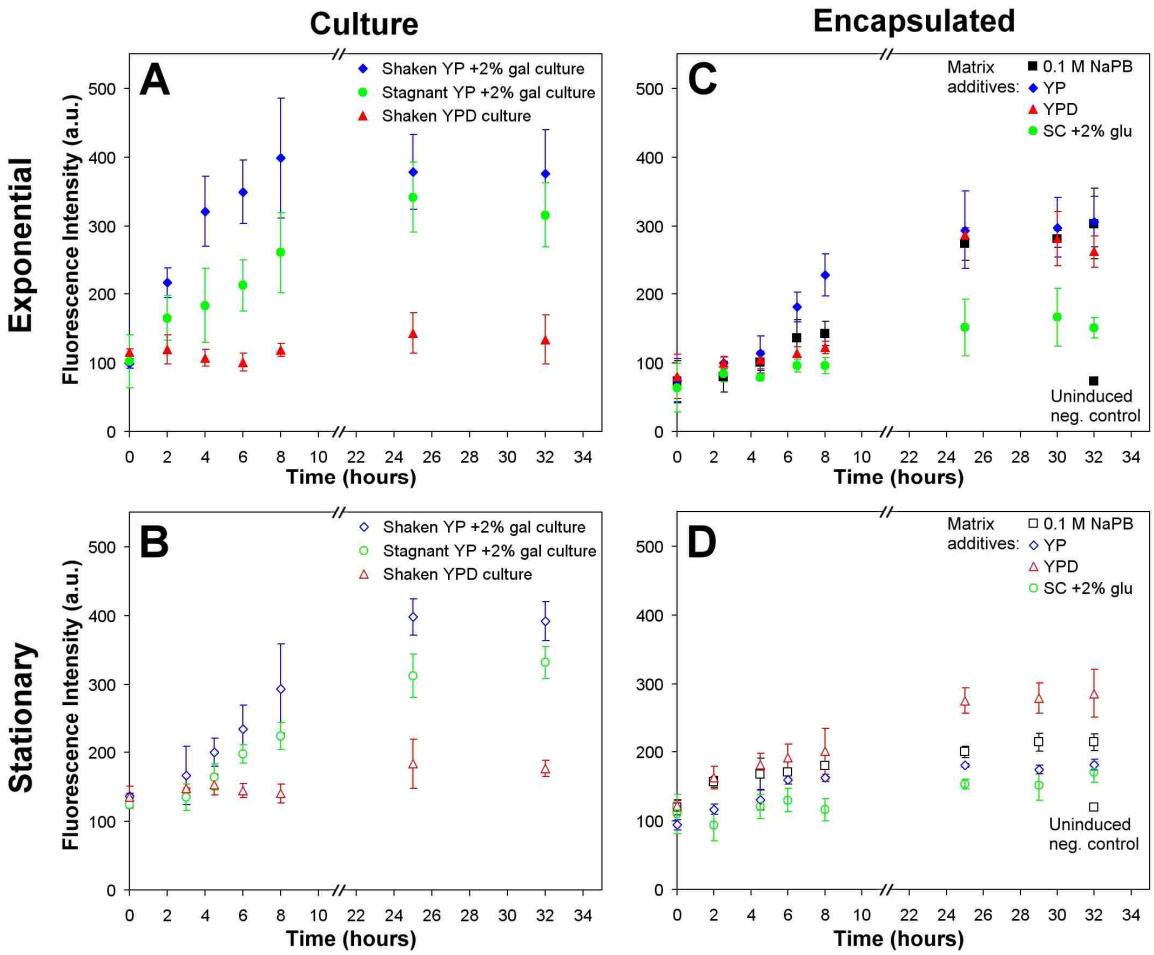

Figure 5. Rate of induced gene expression measured by YFP reporter protein fluorescence intensity for *S. cerevisiae* cells under differing culture conditions (A, B) and encapsulated with in glycerol-silica matrixes with various additives (C, D). Cells from exponential phase culture (A, C), are shown with solid symbols; stationary phase culture (B, D), are with open symbols. *S. cerevisiae* cells encapsulated in glycerol-silica matrixes derived from 50% (vol.) PGS and 50% (vol.) medium that was: nutrient and fermentable carbon rich (YPD, red), nutrient rich without fermentable carbon (YP, blue), nutrient restricted and fermentable carbon rich (SC +2% glu), or without nutrients or fermentable carbon (0.1 M NaPB, black). All media were adjusted to pH 6.0. Encapsulated *S. cerevisiae* cells from exponential culture were entrapped for 24-48 hours, and cells from stationary culture were entrapped for 7 days prior to inducing gene expression. Encapsulated cells were stored at room temperature. Error bars in (A, B) are one standard deviation of measurements from 3 samples. Error bars in (C, D) are one standard deviation of measurements from 3 regions of a given sample. For clarity, only the final data point for uninduced negative control samples (YPD treated) are shown in (C, D). All negative control data points are presented in the supporting information, Figure S6.

The rate of inducible gene expression of cells from exponential culture encapsulated in PGS derived silica gels with various media additives is presented in Figure 5C. Treatment with YP +gal induction medium on top of each of the encapsulated cell monoliths resulted in expression of YFP to varying degrees. Cells from exponential culture encapsulated with nutrient rich YP medium without fermentable carbon (Figure 5C, blue points) had the highest rate of gene expression, with a signal above the LOD_{Fluor} near 6.5 hours from induction. This high rate, relative to the other samples with media additive, may be due to the presence of some nutrients sustaining the metabolically active cells over the first 24-48 hours of encapsulation, while not presenting a competing fermentable carbon source to the cells. In cultures with multiple fermentable carbon sources yeast selectively metabolize the most metabolically accessible carbon source, glucose.[50] This preferential metabolism of glucose could delay uptake and response to galactose, as was observed with YPD entrapped samples (Figure 5C, red points) which generated a signal above the LOD_{Fluor} after approximately 12 hours, and with SC +2% glu entrapped samples (Figure 5C, green points) which did not reach a signal above the LOD_{Fluor} over the course of the experiment. In addition to selective carbon uptake, the SC +2% glu entrapped samples may have also suffered from low viability and locally high acidity from acetic acid generation. Cells entrapped with 0.1 M NaPB (Figure 5C, black points) showed a slightly higher rate of gene expression than the YPD samples (fluorescence intensity > LOD_{Fluor} at 10 hours), which is again attributed to the lack of a competing carbon source. Among these 4 media, YP, NaPB, and YPD all reached a similar saturation level of fluorescence intensity (~290 a.u.) 25 hours after treatment with induction medium. This saturation level is very similar to that obtained for of exponential

phase cells under stagnate culture (Figure 5A, green points), and is also attributed to decreased diffusion of galactose and oxygen through the silica matrix.

Encapsulated cells from stationary culture also exhibited measurable YFP expression, as shown in Figure 5D, but at much lower rates than observed for cells from exponential culture. Similar to the higher background fluorescence observed between stationary and exponential phase cultures (Figure 5A,B), these samples exhibited higher background fluorescence (avg. 111 ± 13 a.u.) in comparison to encapsulated cells from exponential culture (avg. 73 ± 7 a.u.). Initially, rates between the mediums were similar (excluding SC +2% glu, for reasons already addressed). The development of a fluorescence intensity > LOD_{Fluor} for YP, YPD, and 0.1 M NaPB, took approximately 6, 5, and 8 hours, respectively. Again, *S. cerevisiae* entrapped with SC +2% glu did not reach a signal > LOD_{Fluor} after the 32 hour treatment with inducer. At saturation, however, there was greater variation between cells entrapped in the various additives, with *S. cerevisiae* entrapped with YPD showing the highest fluorescence intensity, followed by NaPB, and YP. YFP fluorescence intensity for cells entrapped in SC +2% glu was measurable, but poor.

Ramifications for Encapsulated Living Cell-Based Biosensor Design

The results of this study provide key parameters for selection of cell metabolic phase and silica matrix additives for case-specific cell-based biosensing applications. For example, in the case of 'leave behind' environment monitoring sensors, long-term viability is required. Quiescent cells should be selected and encapsulated without media to prevent exit from stationary phase. Such sensors could potentially operate for over 2

months under the conditions tested in this study, after which the sensors can be collected, analyzed, and replaced. The lower rate of gene expression for cells from stationary culture entrapped with buffer may not be a significant disadvantage as fast response time is often not a requirement. For on-line process monitoring, fast response times are required, therefore cells from exponential culture should be used to meet this requirement. The choice of media additives to the matrix is not as crucial, with the caveats that matrix additives should not compete with the target analyte, nor yield undesirable byproducts. Further, the low viability of cells from exponential culture would require weekly replacement of the sensor. Although not ideal, long-term viability is not a key requirement for on-line process monitoring which typically occurs in developed regions where replacement sensors can be stored under refrigeration, or received through reliable shipments.

CONCLUSIONS

Our investigations have shown the importance of the initial metabolic phase for encapsulated *S. cerevisiae* cells, and the presence of media additives to the encapsulation matrix, on the rate of reporter gene expression and long-term viability of the cells. Encapsulated cells from exponential cultures showed moderately higher rates of induced reporter gene expression, and quiescent cells exhibited significantly greater long-term viability. Addition of media components to the glycerol-silica matrix, while beneficial to reporter gene expression under certain conditions, adversely impacted long-term viability in all cases studied. This was attributed to components of media inducing exit of the cells

from the more robust quiescent state, and the metabolic production of toxic byproducts. These results elaborate further on other silica gel whole-cell encapsulation studies, and provide important insights that may facilitate design and development of effective cell-based biosensors for case-specific applications.

EXPERIMENTAL SECTION

Materials. Aqueous solutions were prepared with 18 MΩ water using a Barnstead Nanopure water purifier (Boston, MA). Tetraethylorthosilicate (TEOS), glycerol (anhydrous), glucose (99%), galactose (99%), and titanium isopropoxide (97%) were purchased from Sigma-Aldrich (St. Louis, MO). Phosphate buffer saline (PBS) solution, pH 7.2 (11.9 mM phosphates, 137 mM NaCl, and 2.7 mM KCl at 1× concentration), hydrochloric acid (HCl), sodium hydroxide (NaOH), sodium phosphate (monobasic and dibasic), and yeast extract were obtained from Fischer Scientific (Pittsburgh, PA). Bacto™ Peptone was from BD Biosciences (Franklin Lakes, NJ). Yeast nitrogen base (YNB) w/o amino acids was from Formedium, LTD (Hunstanton, England), and Drop-out Mix Complete (w/o YNB) was from U.S. Biological (Swampscott, MA). *Funga* Light™ CFDA/PI yeast viability kit was purchased from Invitrogen (Carlsbad, CA). All reagents were used as received.

Yeast Culture Mediums. Yeast extract, peptone, dextrose (YPD) media contained 10 g yeast extract, 20 g Bacto™ peptone, and 20 g of glucose per 1 L of nanopure water. For YPD-agar plates, 20 g of agar was added to YPD media. In yeast

extract, peptone, galactose (YP +gal) induction medium the 20 g of glucose in the YPD recipe was replaced with 20 g of galactose. YP media was identical to YPD media without addition of glucose. Synthetic complete with glucose (SC +2% glu) contained 5.9 g of YNB w/o amino acids, 550 mg KCl, 2 g Drop-out Mix Complete, and 20 g of glucose per 1 L of nanopure water.

Synthesis of Poly(Glycerol) Silicate.[33] A round-bottomed flask equipped with a stir bar, dropping funnel, and reflux condenser was charged with 63.4 g of glycerol (688 mmol) and heated to 60 ºC with stirring. To the hot glycerol was added a mixture of 10.21 g TEOS (49.0 mmol) and 1.02 g titanium isopropoxide (3.0 mmol). After addition, the reaction mixture was refluxed at 130 ºC for 3 hours. Ethanol co-product was removed under vacuum (~10 mTorr) at 130 ºC. The product (63.5g; 98% yield) was a viscose opalescent white liquid that was somewhat soluble with water. The mass of the product agreed with the reported theoretical formula: $Si(C_3H_7O_3)_4 \cdot 10C_3H_8O_3$;[33] however, it is certain that many isomers exist in the mixture as well as some inadvertent hydrolysis products.

Preparation of Poly(Glycerol) Silicate (PGS) Derived Silica Gels and Encapsulated *S. cerevisiae* Monoliths. For gelation time point experiments, a given volume percent (20, 35, 50, 65, 80%) of buffer or media was added to the PGS (3 mL total volume) in a polystyrene 15 mL centrifuge tube and homogenized by vortexing for 60 seconds. For silica matrix encapsulated *S. cerevisiae* monoliths, 50 volume percent of *S. cerevisiae* cells (10^6-10^7 cells/mL) in a given media or buffer previously adjusted to

pH 6.0, was added to the PGS (250-350 μL total volume) in a 1.5 mL polypropylene microcentrifuge tube and homogenized by vortexing for 60 seconds. All samples were allowed to gel in the centrifuge tubes and stored capped at room temperature (22 ºC). The theoretical density of the final wet gels corresponds to 1.1-1.3 $g \cdot cm^{-3}$.

Fluorescence and SEM Imaging. Fluorescence microscopy imaging was performed on an Olympus IX70 microscope and recorded using an Olympus DP71 camera. A Hitachi 3200N scanning electron microscope (SEM) operating at 25 kV was used to directly image poly(glycerol) silica gel encapsulated *S. cerevisiae* cells on a graphite support ~6 hrs post gelation, without further preparation.

^{29}Si NMR Analysis. ^{29}Si solution state NMR spectra of the PGS were obtained on a Bruker DRX 400 using a 10mm ^{29}Si-selective probe. The ^{1}H-decoupled ^{29}Si spectra were acquired using an inverse gating pulse sequence with 512 scans and a 60 second recycle delay. The spectra were referenced to the external secondary standard of neat TMS at $\delta(^{29}Si) = 0$ ppm. The solid state ^{29}Si magic angle spinning (MAS) NMR spectra of silica-glycerol gels were obtained on a Bruker Avance 400 using a 7 mm broadband probe spinning at 4 kHz, with 4k scans and a 240 second recycle delay using a standard single pulse Bloch decay sequence. The solid state spectra were referenced to the secondary external standard Q_8M_8 at $\delta(^{29}Si) = 11.8$ ppm with respect to TMS. The degree of condensation (C) was defined based on the relative concentrations of the different Q^n species:

$$C = \frac{[Q^1] + 2[Q^2] + 3[Q^3] + 4[Q^4]}{4}$$

Long-Term Viability Measurements. Encapsulated *S. cerevisiae* cell viability was measured using three methods: fluorescence dyes, 24 hour culture in YDP medium, and 48 hour growth on YPD-agar. For viability dye assays, the *Funga* Light™ assay was used which contains a cell permeable non-specific esterase substrate (CFDA) and a cell membrane integrity indicator (PI). Viability assay was performed using the manufacturer's protocol with slight modifications: 1 μL of CFDA solution (1 mg in 100 μL DMSO) and 1 μL of PI solution (20 mM in H_2O) was added to 1 mL of 1× PBS, pH 7.4. From this solution 250 μL was pipetted on top of a glycerol-silica gel encapsulated *S. cerevisiae* cell monolith and incubated for 45-60 min at 30 ºC. Following incubation a portion of the monolith was removed from the microcentrifuge tube by scrapping the monolith with a small sterile wooden dowel. This portion was then mounted between a glass microscope slide and coverslip. Cells were then imaged with an inverted fluorescence microscope. Cells with esterase activity and intact membranes fluoresced green and were counted as viable. Cells without esterase activity and damaged membranes fluoresced red, cells with residual esterase activity and damaged membranes fluoresced yellow, neither was counted as viable.

As viability is ultimately defined as the ability of a cell to reproduce, cell culture and the ability of cells to form colonies on solid medium plates was also used to assess viability. For 24 hour culture, a portion of a glycerol-silica gel encapsulated *S. cerevisiae* cell monolith was removed and mixed with 200 μL of 1× PBS, pH 7.4, forming a homogenous suspension. From this cell-PBS suspension, 100 μL was added to 5 mL of YPD medium in a 15 mL culture tube from which 100 μL was retained for the 48 hour

growth on YDP-agar plates (described below). The remainder was incubated with shaking at 30 ºC for 24 hours. The optical density at 600 nm ($O.D._{600}$) was measured at time = 0 and 24 hours using a μQuant microplate reader (Bio-Tek Instruments, Winooski, VT). For the 48 hour growth on YDP-agar plates, the retained 100 μL cell-YPD suspension was spread onto YPD-agar in a plastic 10 cm Petri dish and incubated at 30 ºC for 48 hours.

Rate of Inducible Gene Expression Measurements. The rate of gene expression was monitored by measuring the fluorescence intensity with time of the reporter protein, yellow fluorescent protein (YFP). For induction of YFP expression in *S. cerevisiae* culture, exponential or stationary phase cells were pelletted by centrifugation and re-suspended in YP +gal induction medium. The cells were incubated with shaking, or under stagnant conditions, at 30 ºC. At given time intervals, a 50-100 μL aliquot was removed from the culture, pelleted, aspirated, and re-suspended in 1× PBS, pH 7.4. Cells were imaged via fluorescence microscopy. For PGS derived sol-gel matrix encapsulated *S. cerevisiae* cells 250 μL of YP +gal was pipetted on top of the matrix, followed by incubation at 30 ºC for various times between 0 and 32 hours. A separate monolith was prepared for each time point. Following the incubation, a portion of the monolith was removed, mounted between a glass microscope slide and coverslip, and imaged. Identical microscope and camera settings were used for all imaging allowing quantitative analysis of YFP expression between all samples imaged. The limit of fluorescence detection represents the lowest fluorescence intensity of a positive control whose signal strength is greater than the sum of the mean fluorescent intensity of a negative control sample (μ)

and its standard deviation (σ) multiplied by 3 ($LOD_{Fluor.} = \mu + 3\sigma$). The time required for a given sample to develop a fluorescence intensity greater than the LOD_{Fluor} was used to compare the rate of YFP expression between samples.

References

1. Meunier, C. F.; Dandoy, P.; Su, B. L. *J. Colloid Interf. Sci.* 2010, *342*, 211-224.
2. Yap, F. L.; Zhang, Y. *Biosens. Bioelectron.* 2007, *22*, 775-788.
3. Harper, J. C.; Khirpin, C. Y.; Carnes, E. C.; Ashley, C. E.; Lopez, D. M.; Savage, T.; Jones, H. D. T.; Davis, R. W.; Nunez, D. E.; Brinker, L. M.; Kaehr, B.; Brozik, S. M.; Brinker, C. J. *ACS Nano* 2010, *4*, 5539-5550.
4. Baca, H. K.; Ashley, C.; Carnes, E.; Lopez, D.; Flemming, J.; Dunphy, D.; Singh, S.; Chen, Z.; Liu, N. G.; Fan, H. Y.; Lopez, G. P.; Brozik, S. M.; Werner-Washburne, M.; Brinker, C. J. *Science* 2006, *313*, 337-341.
5. Dave, B. C.; Dunn, B.; Valentine, J. S.; Zink, J. I. *Anal. Chem.* 1994, *66*, A1120-A1127.
6. Bjerketorp, J.; Hakansson, S.; Belkin, S.; Jansson, J. K. *Curr. Opin. Biotech.* 2006, *17*, 43-49.
7. Coradin, T.; Livage, J. *Acc. Chem. Res.* 2007, *40*, 819-826.
8. Stevens, M. M.; George, J. H. *Science* 2005, *310*, 1135-1138.
9. Zhang, S. G. *Nat. Biotech.* 2004, *22*, 151-152.
10. Carnes, E. C.; Lopez, D. M.; Donegan, N. P.; Cheung, A.; Gresham, H.; Timmins, G. S.; Brinker, C. J. *Nat. Chem. Bio.* 2010, *6*, 41-45.
11. Carnes, E. C.; Harper, J. C.; Ashley, C. E.; Lopez, D. M.; Brinker, L. M.; Liu, J. W.; Singh, S.; Brozik, S. M.; Brinker, C. J. *J. Am. Chem. Soc.* 2009, *131*, 14255-14257.
12. Raghavan, S.; Chen, C. S. *Adv. Mat.* 2004, *16*, 1303-1313.
13. Kandimalla, V. B.; Tripathi, V. S.; Ju, H. X., *Crit. Rev. Anal. Chem.* 2006, *36*, 73-106.
14. Carturan, G.; Dal Toso, R.; Boninsegna, S.; Dal Monte, R. *J. Mater. Chem.* 2004, *14*, 2087-2098.
15. Meunier, C. F.; Rooke, J. C.; Leonard, A.; Xie, H.; Su, B. L. *Chem. Commun.* 2010, *46*, 3843-3859.
16. Gupta, R.; Chaudhury, N. K. *Biosens. Bioelectron.* 2007, *22*, 2387-2399.
17. Avnir, D.; Coradin, T.; Lev, O.; Livage, J. *J. Mater. Chem.* 2006, *16*, 1013-1030.
18. Dunphy, D. R.; Alam, T. M.; Tate, M. P.; Hillhouse, H. W.; Smarsly, B.; Collord, A. D.; Carnes, E.; Baca, H. K.; Kohn, R.; Sprung, M.; Wang, J.; Brinker, C. J. *Langmuir* 2009, *25*, 9500-9509.
19. Hamm, C. E.; Merkel, R.; Springer, O.; Jurkojc, P.; Maier, C.; Prechtel, K.; Smetacek, V. *Nature* 2003, *421*, 841-843.
20. Premkumar, J. R.; Lev, O.; Rosen, R.; Belkin, S. *Adv. Mater.* 2001, *13*, 1773-1775.

21. Premkumar, J. R.; Rosen, R.; Belkin, S.; Lev, O. *Anal. Chim. Acta* 2002, *462*, 11-23.
22. Premkumar, J. R.; Sagi, E.; Rozen, R.; Belkin, S.; Modestov, A. D.; Lev, O. *Chem. Mater.* 2002, *14*, 2676-2686.
23. Sagi, E.; Hever, N.; Rosen, R.; Bartolome, A. J.; Premkumar, J. R.; Ulber, R.; Lev, O.; Scheper, T.; Belkin, S. *Sens. Actuat. B-Chem.* 2003, *90*, 2-8.
24. Jia, J. B.; Tang, M. Y.; Chen, X.; Li, Q.; Dong, S. J. *Biosens. Bioelectron.* 2003, *18*, 1023-1029.
25. Trogl, J.; Ripp, S.; Kuncova, G.; Sayler, G. S.; Churava, A.; Parik, P.; Demnerova, K.; Halova, J.; Kubicova, L. *Sens. Actuat. B-Chem.* 2005, *107*, 98-103.
26. Nguyen-Ngoc, H.; Tran-Minh, C. *Anal. Chim. Acta* 2007, *583*, 161-165.
27. Yu, D.; Volponi, J.; Chhabra, S.; Brinker, C. J.; Mulchandani, A.; Singh, A. K. *Biosens. Bioelectron.* 2005, *20*, 1433-1437.
28. Ferrer, M. L.; Yuste, L.; Rojo, F.; del Monte, F. *Chem. Mater.* 2003, *15*, 3614-3618.
29. Perullini, M.; Jobbagy, M.; Moretti, M. B.; Garcia, S. C.; Bilmes, S. A. *Chem. Mater.* 2008, *20*, 3015-3021.
30. Kuncova, G.; Podrazky, O.; Ripp, S.; Trogl, J.; Sayler, G. S.; Demnerova, K.; Vankova, R. *J. Sol-Gel Sci. Technol.* 2004, *31*, 335-342.
31. Ferrer, M. L.; Garcia-Carvajal, Z. Y.; Yuste, L.; Rojo, F.; del Monte, F. *Chem. Mater.* 2006, *18*, 1458-1463.
32. Allen, C.; Buttner, S.; Aragon, A. D.; Thomas, J. A.; Meirelles, O.; Jaetao, J. E.; Benn, D.; Ruby, S. W.; Veenhuis, M.; Madeo, F.; Werner-Washburne, M. *J. Cell Biol.* 2006, *174*, 89-100.
33. Khonina, T.; Chupakhin, O.; Larionov, L.; Boyakovskaya, T.; Suvorov, A.; Shadrina, E. *Pharm. Chem. J.* 2008, *42*, 609-613.
34. Brandhuber, D.; Torma, V.; Raab, C.; Peterlik, H.; Kulak, A.; Husing, N. *Chem. Mater.* 2005, *17*, 4262-4271.
35. Gill, I. *Chem. Mater.* 2001, *13*, 3404-3421.
36. Gill, I.; Ballesteros, A. *J. Am. Chem. Soc.* 1998, *120*, 8587-8598.
37. Nassif, N.; Bouvet, O.; Rager, M. N.; Roux, C.; Coradin, T.; Livage, J. *Nat. Mater.* 2002, *1*, 42-44.
38. Nassif, N.; Roux, C.; Coradin, T.; Rager, M. N.; Bouvet, O. M. M.; Livage, J. *J. Mater. Chem.* 2003, *13*, 203-208.
39. Fu, D.; Libson, A.; Miercke, L. J.; Weitzman, C.; Nollert, P.; Krucinski, J.; Stroud, R. M. *Science* 2000, *290*, 481-486.
40. Sahai, N.; Tossell, J. A. *Inorg. Chem.* 2002, *41*, 748-756.
41. Kemmitt, T.; Milestone, N. *Aust. J. Chem.* 1995, *48*, 93-102.
42. (a) Goldberg, E. P.; Powers, E. J. *J. Polym. Sci. Polym. Phys. Ed.* 1964, 2, 835. (b) Goneberg, A.; Verheyden, A. Belgian Patent 510419 (to Union chimique belge Soc.), 1952. (c) Krimm, H.; Schnell, H. German Patent 1136114 (to Farbenfabrik Bayer), 1962. (d) Vaughn, H. A. British Patent 989379, (to General Electric Co.), 1965.
43. Brinker, C. J.; Scherer, G. W. *Sol-Gel Science*; Academic Press, 1989.
44. Brook, M. A.; Chen, Y.; Guo, K.; Zhang, Z.; Jin, W.; Deisingh, A.; Cruz-Aguado, J.; Brennan, J. D. *J. Sol-Gel Sci. Technol.* 2004, *31*, 343-348.
45. Gray, J. V.; Petsko, G. A.; Johnston, G. C.; Ringe, D.; Singer, R. A.; Werner-Washburne, M. *Microbiol. Mol. Biol. Rev.* 2004, *68*, 187-206.

46. Granot, D.; Snyder, M. *Proc. Nat. Acad. Sci. USA* 1991, *88*, 5724-5728.
47. Burtner, C. R.; Murakami, C. J.; Kennedy, B. K.; Kaeberlein, M. *Cell Cycle* 2009, *8*, 1256-1270.
48. Nassif, N.; Roux, C.; Coradin, T.; Bouvet, O. M. M.; Livage, J. *J. Mater. Chem.* 2004, *14*, 2264-2268.
49. van der Meer, J. R.; Belkin, S. *Nat. Rev. Micro.* 2010, *8*, 511-522.
50. Gelade, R.; Van de Velde, S.; Van Dijck, P.; Thevelein, J. *Genome Biol.* 2003, *4*, 233.

SUPPORTING INFORMATION

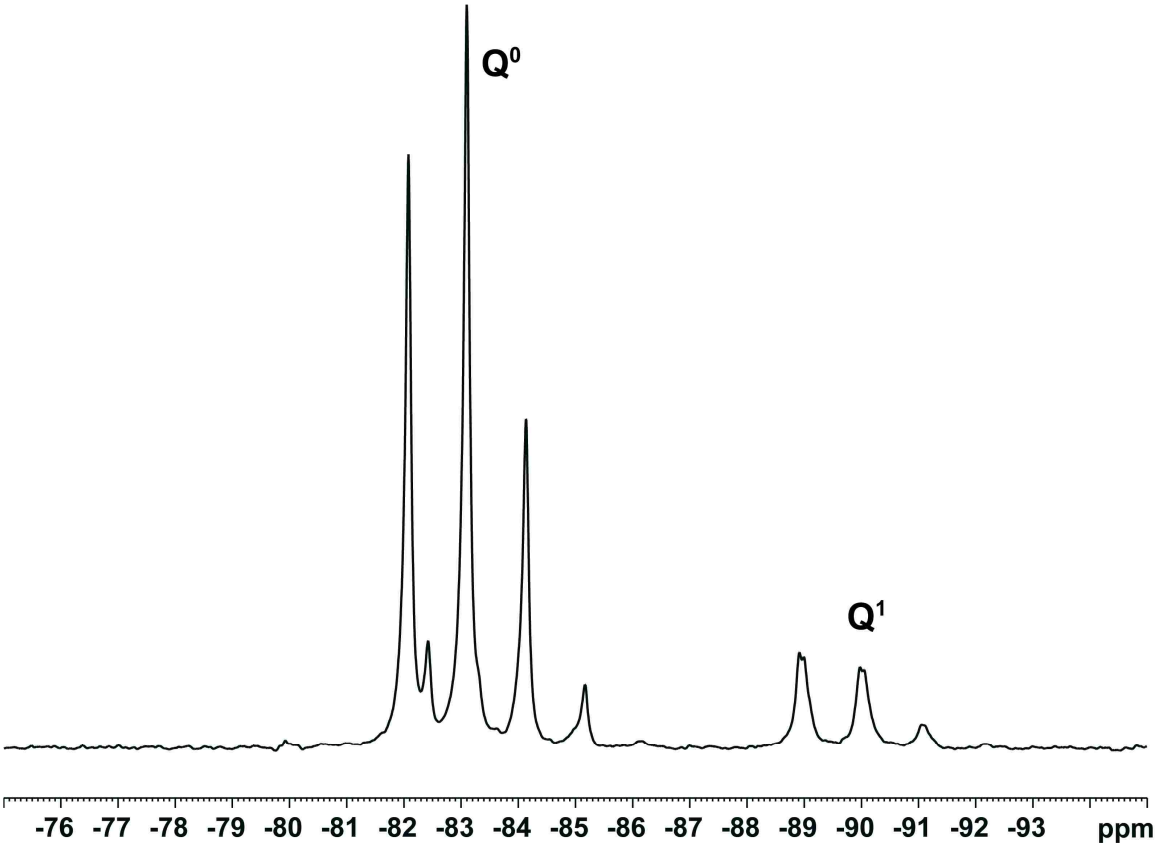

Figure S1. ^{29}Si solution NMR spectrum of the as synthesized poly(glycerol) following 2 months of capped storage at room temperature. Several resonances in both the Q^0 and Q^1 regions are observed.

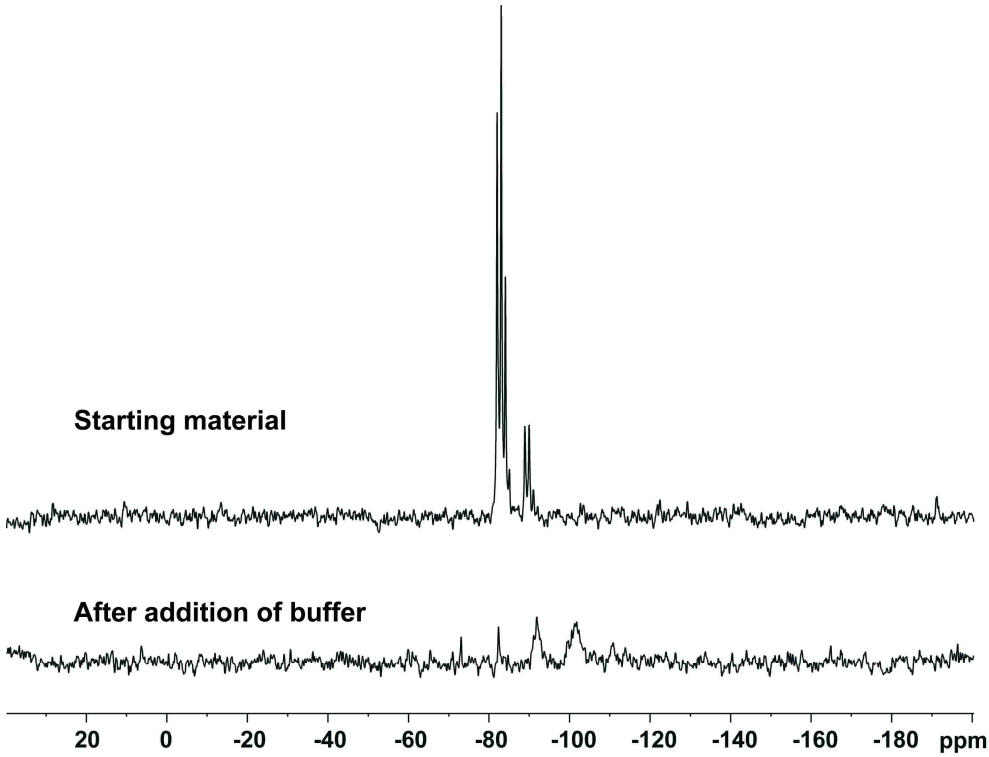

Figure S2. ^{29}Si solution state NMR spectrum of the as synthesized poly(glycerol) before and after addition of equal volume 0.1 M NaPB, pH 6.1.

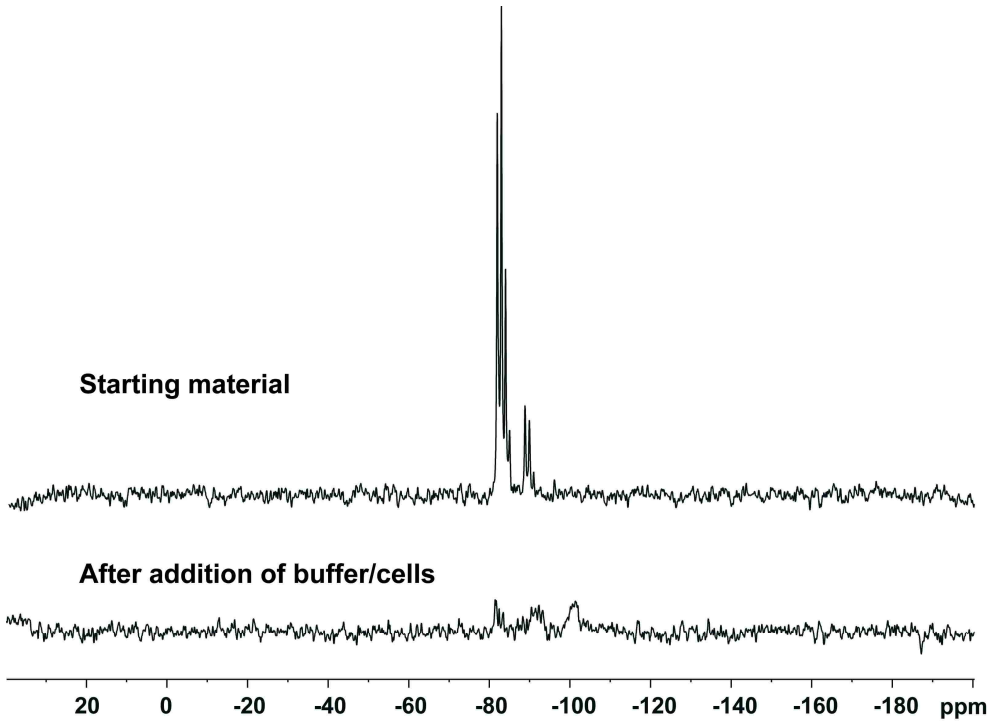

Figure S3. ^{29}Si solution state NMR spectrum of the as synthesized poly(glycerol) before and after addition of equal volume yeast cell suspension in 0.1 M NaPB, pH 6.1.

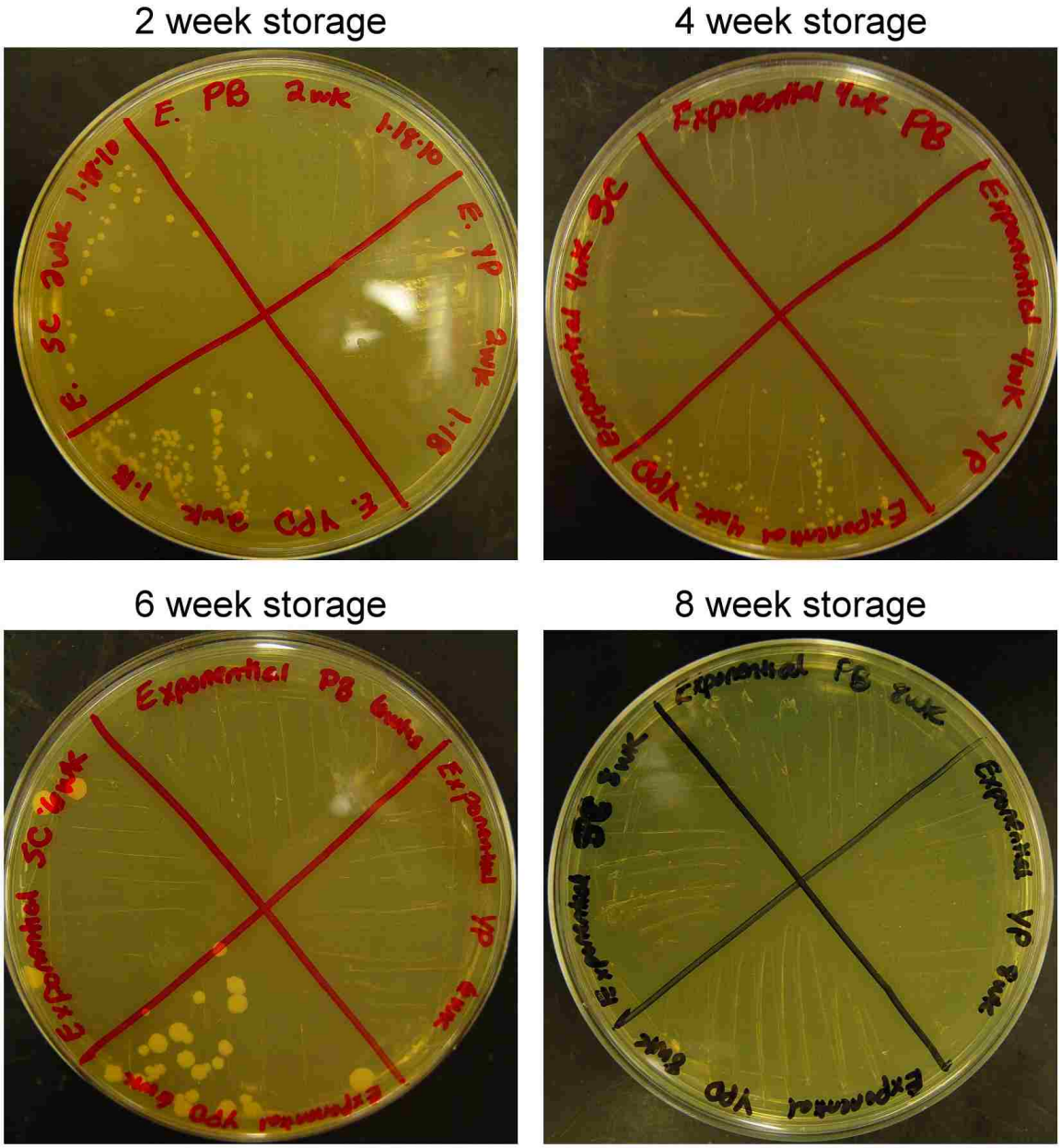

Figure S4. Images of colonies formed from plating portions of glycerol-silica encapsulated *S. cerevisiae* cell monoliths onto YPD-agar after room temperature capped storage for 2, 4, 6, or 8 weeks. Encapsulated *S. cerevisiae* cells were from **exponential culture**. Glycerol-silica gels derived from 50% (vol.) PGS and 50% (vol.) medium that was: nutrient and fermentable carbon rich (YPD, bottom quadrant), nutrient rich without fermentable carbon (YP, right quadrant), nutrient restricted and fermentable carbon rich (SC, left quadrant), or without nutrients or fermentable carbon (PB, top quadrant).

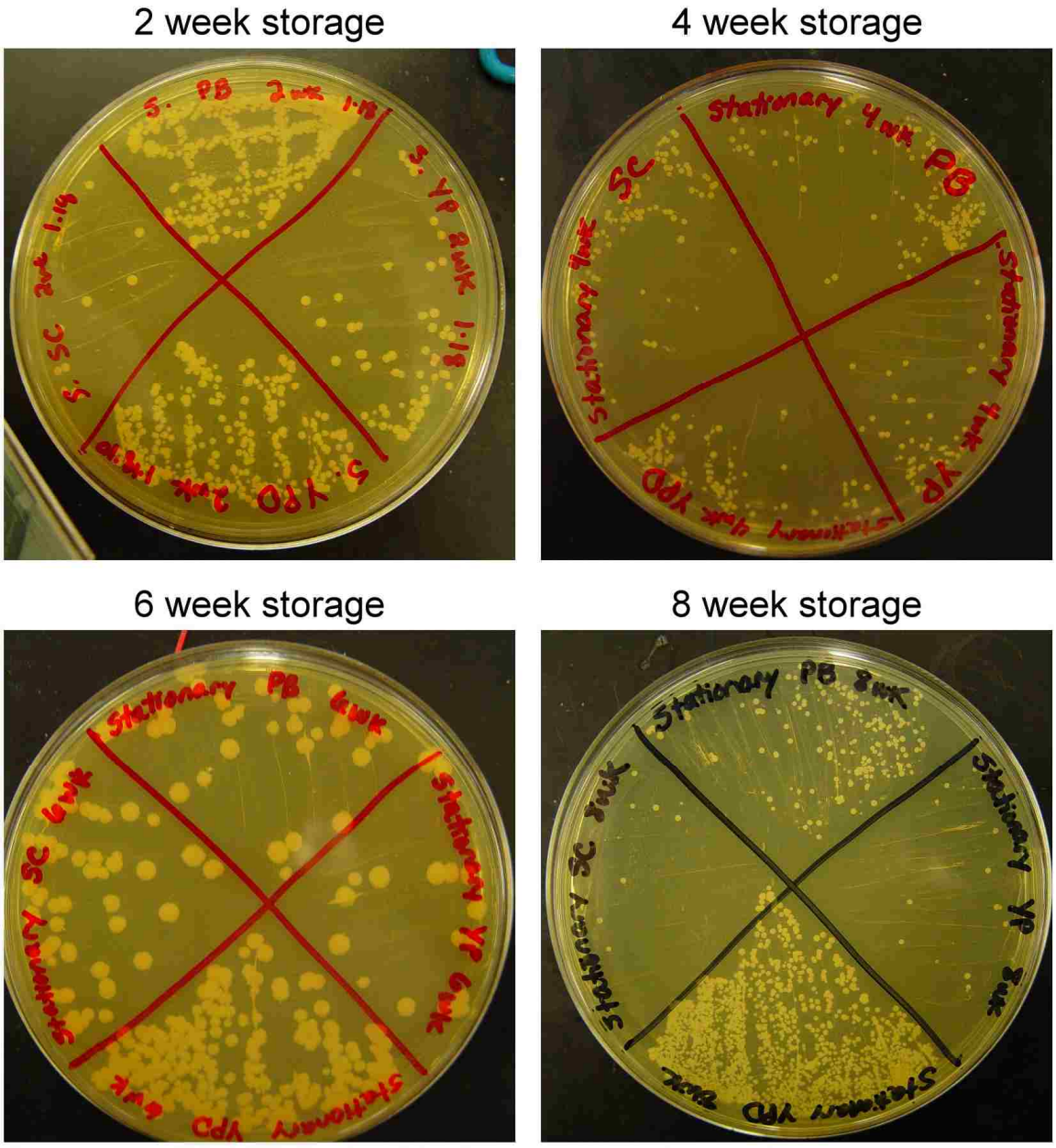

Figure S5. Images of colonies formed from plating portions of glycerol-silica encapsulated *S. cerevisiae* cell monoliths onto YPD-agar after room temperature capped storage for 2, 4, 6, or 8 weeks. Encapsulated *S. cerevisiae* cells were from **stationary phase culture**. Glycerol-silica gels derived from 50% (vol.) PGS and 50% (vol.) medium that was: nutrient and fermentable carbon rich (YPD, bottom quadrant), nutrient rich without fermentable carbon (YP, right quadrant), nutrient restricted and fermentable carbon rich (SC, left quadrant), or without nutrients or fermentable carbon (PB, top quadrant).

Table S1. Optical density ($O.D._{600}$) measurements following 24 hour shaken culture of *S. cerevisiae* removed from glycerol-silica gels with 50% (vol.) medium additives.[a]

		24 hr culture in YPD ($O.D._{600}$)			
	Stored for:[1]	2 wks	4 wks	6 wks	8 wks
Exponential	0.1 M NaPB	1.1	0.37	0.10	0.3
	YP	1.76	0.31	0.16	0.18
	YPD	0.96	0.90	1	0.41
	SC +2% glu	1.2	1	1.1	0.25
Stationary	0.1 M NaPB	1.45	2.3	1.9	1.13
	YP	1.1	2.93	2	1
	YPD	1.79	1.45	2.5	1.25
	SC +2% glu	1.42	1.61	2.1	1.04

a All mediums were adjusted to pH 6.0.
1 Encapsulated cells stored at room temperature.

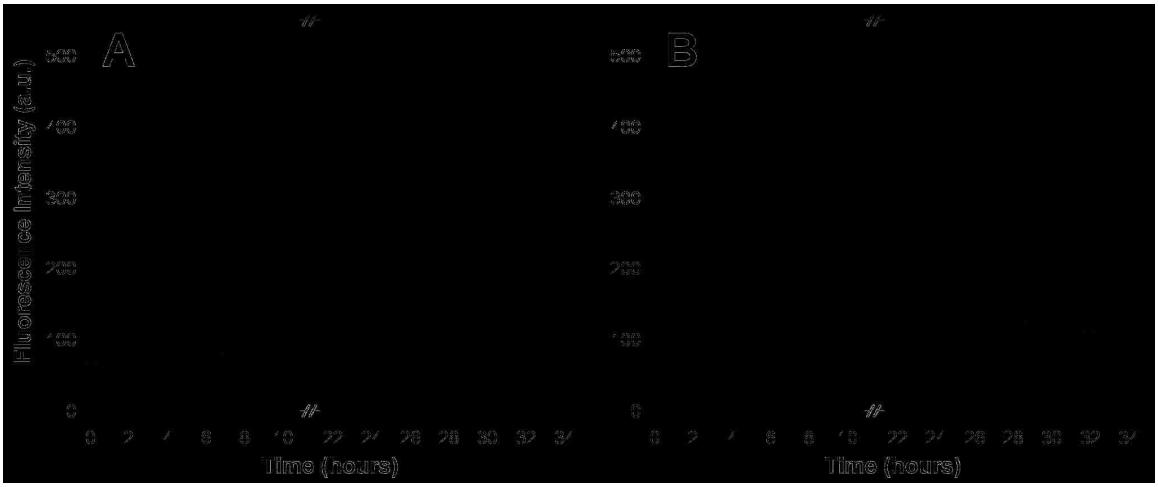

Figure S6. YFP reporter protein fluorescence intensity for *S. cerevisiae* cells from (A) exponential (B) and stationary phase culture encapsulated in glycerol-silica matrixes derived from 50% (vol.) PGS and 50% (vol.) 0.1 M NaPB, pH 6.0, treated with YPD (negative control medium).

CHAPTER 4

Orthogonal Cell-Based Biosensing: Fluorescent, Electrochemical, and Colorimetric Detection from Silica Matrix Encapsulated Cells in an ITO/Plastic Laminate Cartridge

Harper, J. C., Edwards, T. L., Savage, T., Harbaugh, S., Kelley-Loughnane, N., Stone, M. O., Brinker, C. J., Brozik, S. M.

Abstract

We report living cell-based sensor platform capable of orthogonal fluorescent, electrochemical, and colorimetric detection of a single target analyte in a complex solution. Coupling these three signal transduction methods may substantially reduce the impact of potential interferants, increase confidence in the sensor's output, and holds significant implications towards development of practical devices for environmental monitoring.

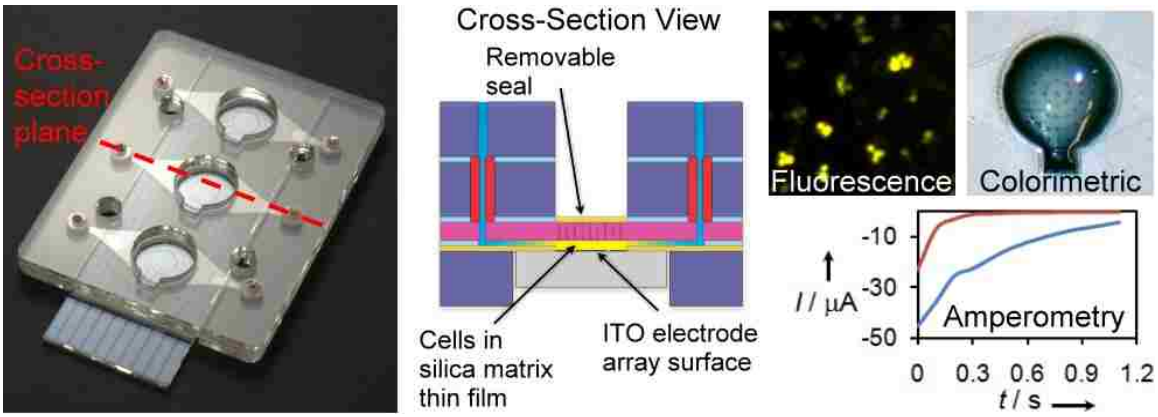

Abstract Figure

INTRODUCTION

Advances in agriculture and foodstuff production have sustained the current rate of world population growth, but have lead to an enormous increase in the use of pesticides and herbicides, with clear implications towards environmental and human health.[1,2] Analytical devices capable of detecting chemicals in the '*ex*-laboratory' environment with high specificity and sensitivity are essential for regulatory purposes and for advancing our ability to identify, understand, and enable remediation of environmental pollutants. Additionally, such devices could prove valuable in food safety, medicine, public safety, and military defense applications.[3] Thus, demand for analytical devices that are robust, inexpensive, portable, low-power and simple to operate, continues to dramatically increase.

As an alternative to traditional chemical and physical analysis techniques, analytical tools based on living cells to provide analyte recognition and response functions are attracting increased attention.[4] Often described as the equivalent of canaries used to detect toxic gases in mines,[5] whole cell-based biosensors have proven effective in the non-specific detection of various cellular stresses, DNA damage, and general toxicity.[6,7] Additionally, living cells are capable of amplifying subtle signals by many orders of magnitude *via* native signaling cascades. Used together, with advances in genetic engineering, real-time and highly sensitive and specific cell-based detection of bacteria, viruses, and toxins has been reported.[8]

Living cell-based biosensors, however, suffer from several limitations including (i) difficulties in interfacing cells with the transducer, effectively hindering translation of

the biological response to a measurable signal,[4] (ii) susceptibility of cells to stresses from the *ex vivo* environment leading to a high false positive/negative response rate[9] or loss in viability/activity,[10] and (iii) interferences with complex sample solutions. Depending on one's method of signal transduction, common interferants include molecules that are redox active at the potential range employed for electrochemical measurements,[4] or are autofluorescent or cause high solution turbidity, confounding optical measurements.[1] To address limitations associated with interference and ambiguous readings, use of a device that relies on more than one distinct method for signal transduction may prove an innovative option. Coupling the two most commonly used signal transducers in cell-based biosensing, electrochemistry and fluorescence, would provide complementary information regarding the sample properties, substantially decreasing false positive/negative responses due to interferants, and significantly increasing the confidence of the analyst in the results.

Indeed, platforms capable of simultaneous amperometric and fluorescence measurements of cells,[11] and most recently, simultaneous amperometric and total internal reflection fluorescent (TIRF) measurements,[12] have been reported. In these pioneering works exocytosis from chromaffin cells was monitored under conditions of continuous perfusion culture. Although ideal for fundamental molecular biology studies, these devices were not designed for long-term environmental biosensing. In another recent study, the utility of coupling electrochemical and fluorescent techniques for cell-based biosensing of pesticides was reported.[13] In this work photosynthetic cells were entrapped within protein gels in two separate devices, one for fluorescence

measurements, the other for amperometric measurements. The authors showed that coupling these two data sets provided less ambiguous identification of target toxins.

Herein we report the first orthogonal detection mode living cell-based sensor capable of fluorescent, electrochemical and colorimetric measurements of a target analyte in complex media, all on a single device. Orthogonality is enabled by use of multiple cell lines engineered to provide distinct responses to the target analyte. We also address sensitivity of the cells to the environment *via* entrapment in a matrix derived from glycerated silicate, which we have recently characterized for cell-based sensing applications.[14] Finally, we report what we believe to be the first co-entrapment of eukaryotic and bacterial cells in a silica matrix, demonstrating multianalyte biodetection by mixing cell lines that would not be compatible under standard culture conditions.

RESULTS AND DISCUSSION

Fabrication of the senor platform's fluidic cartridge was accomplished *via* laser machining of plastic laminates.[15] The device was composed of nine thin plastic layers, each cut with a CO_2 laser, and an ITO coated microscope slide patterned by photolithography and wet chemical etching. A schematic layer-by-layer representation of the ITO-glass/plastic laminate cartridge is shown in Figure 1a, with an expanded layer-by-layer schematic presented in the Supporting Information (Figure S1). Adhesive coatings on plastic layers allowed for assembly of the device by simple hydraulic pressing of the layers. Fabrication details can be found in the Supporting Information.

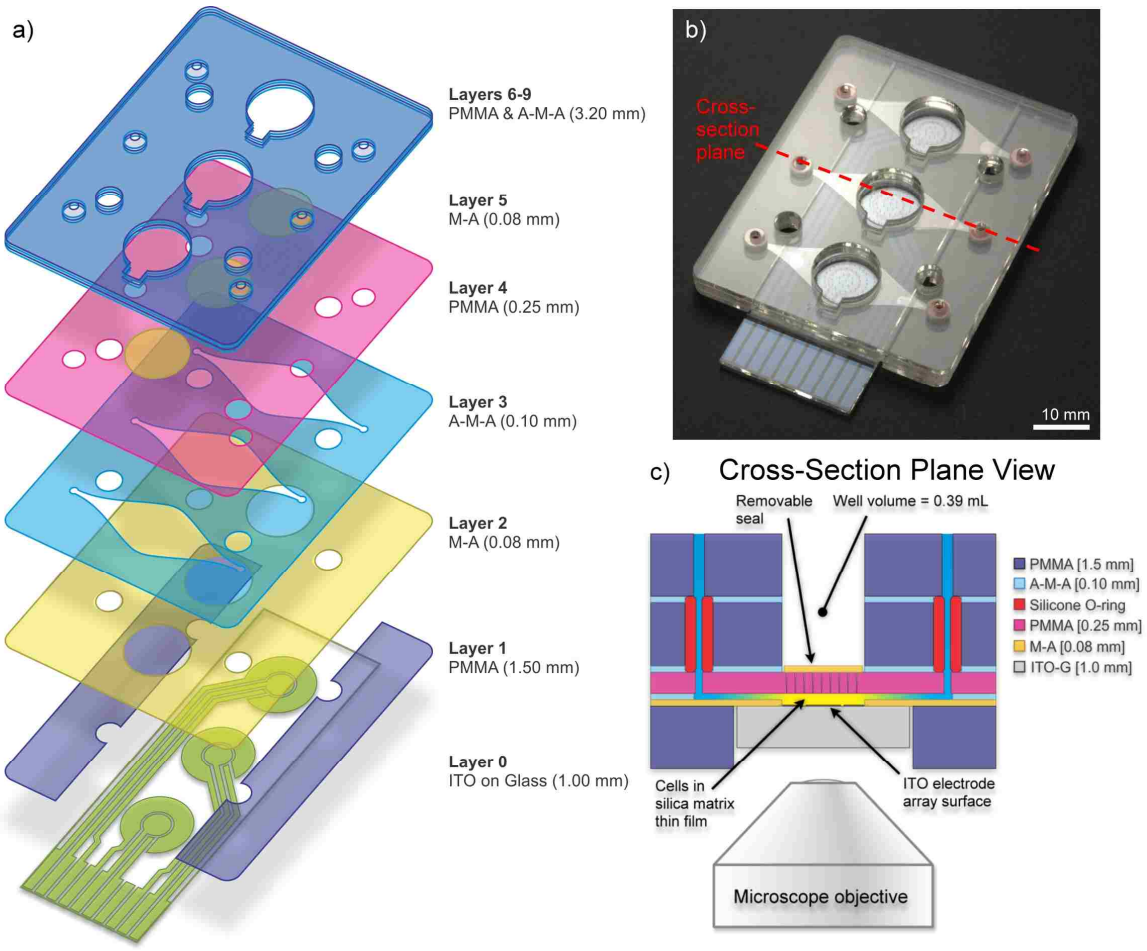

Figure 1. a) Schematic layer-by-layer representation and b) photograph of the ITO-glass/plastic laminate cartridge. Fluorescence and visible detection occur through the glass, ITO, and silica matrix; electrochemical detection is performed on the ITO surface. c) Cross-section cutout schematic of the device (from the plane marked in panel (b)) highlighting the location of living cells encapsulated within the glycerol-silica matrix thin film (bright yellow). Dark blue represents fluidic access vials through the o-rings and the fluidic channel over the ITO electrode array for introducing the cell/silica matrix solution to the cartridge. Pores were laser machined into portions of PMMA layer 4 (pink) directly above the electrodes, providing analyte solution access to the underlying entrapped cells upon removal of the Mylar seal at the bottom of the well (layer 5, yellow). Abbreviations: polymethylmethacrylate (PMMA), polyethyleneterapthalate (Mylar, M), indium tin oxide (ITO), glass (G), Mylar coated with adhesive oriented down (M-A), Mylar coated with adhesive on both sides (A-M-A).

A photograph of the assembled cartridge is shown in Figure 1b. Visible in the image are the ITO leads and the array of 3 electrochemical cells, each containing 3 individually addressable electrodes at the bottom of each well. Surface areas of the ITO working, pseudo-reference, and counter electrodes are 22.9, 8.2, and 55.1 mm^2, respectively. A schematic of the assembled cartridge highlighting the conductive electrode regions is presented in Figure S2. The cross-section view through one of the wells (Figure 1c) highlights the region in which cells entrapped in a glycerol-silica matrix thin film are interfaced between the ITO electrode surface and a polymethylmethacrylate (PMMA) sheet (Figures 1a and S1, layer 4, pink). The portion of this PMMA sheet that forms the well bottom is porous, allowing the analyte solution to access the underlying silica matrix entrapped cells. A removable seal (layer 5, yellow) is placed over the porous well bottoms during assembly (Figure 1c). Living cells in a glycerol-silica matrix precursor solution are introduced to the device through microfluidic ports on either side of each well. Following introduction of the cell/glycerol-silica matrix solution, the inlet and outlet ports are sealed with adhesive tape. In this configuration, the device can be stored under ambient conditions for months with significant retention in cellular activity and viability (40% viability after 60 days).

For orthogonal detection mode cell-based biosensing, an equal molar mixture of *S. cerevisiae* cells engineered to express yellow fluorescent protein (YFP), and *S. cerevisiae* cells engineered to express and secret glucose oxidase (GOx), were immobilized within a glycerol-silica matrix thin film in an ITO-glass/plastic laminate cartridge. Expression of YFP and GOx in each cell line is induced by the presence of a model analyte, galactose. Detection of YFP occurred *via* fluorescence microscopy

imaging through the transparent ITO electrodes and silica matrix. Electrochemical detection occurred at the ITO electrode *via* chronoamperometric reduction of hydrogen peroxide (H_2O_2) produced during GOx turnover, using a hand-held potentiostat. To enhance the amperometric response from H_2O_2 reduction, the ITO surface was modified with gold nanoparticles (AuNPs), followed by deposition of Prussian Blue (PB). Electrode surface functionalization was performed within the fully assembled device and was selective, modifying the working electrodes only. Details of the ITO array surface modification process, including a photograph, SEM images, and electrochemical characterization, are presented in the Supporting Information (Figure S3). The resultant surface (ITO-AuNP-PB) retained excellent optical transparency, allowing for fluorescence measurements through the functionalized electrodes, while showing a significantly enhanced H_2O_2 current response at low potentials (–100 mV vs. ITO pseudo-reference). Introduction of living cell/glycerol-silica matrix precursor solution to the device occurred following electrode surface functionalization.

A solution of complex media (YP, see Supporting Information) containing galactose (2% mass) was added to a well in the ITO-glass/plastic laminate cartridge, following removal of the plastic cap (layer 5), to an end volume of 250 μL. Cells entrapped beneath the well were then monitored *via* simultaneous fluorescence microscopy and chronoamperometry measurements. The electrochemical and fluorescence response with time is shown in Figure 2a. The amperometric response (blue trace) initially increased more rapidly than the fluorescence response (red trace), reaching a signal 3σ above the negative control signal in less than 4 hours. This same fluorescence signal intensity (3σ above the negative control) took nearly 6 hours to develop. This is

not unexpected as the electrochemical response is based on catalytic production of H_2O_2 by GOx, whereas the fluorescent response is proportional only to the total concentration of YFP expressed by the cells (not catalytic). Between 6-9 hours from introduction of the analyte sample, the electrochemical response reached a maximum, after which the signal continued to decrease with time. This is attributed to the depletion of enzymatic substrate, and the breakdown and electrochemical consumption of H_2O_2. In contrast, the fluorescent signal continued to increase, reaching a maximum between 12-18 hours from induction. This fluorescent signal was highly stable, being detectable even after cell death (data not shown).

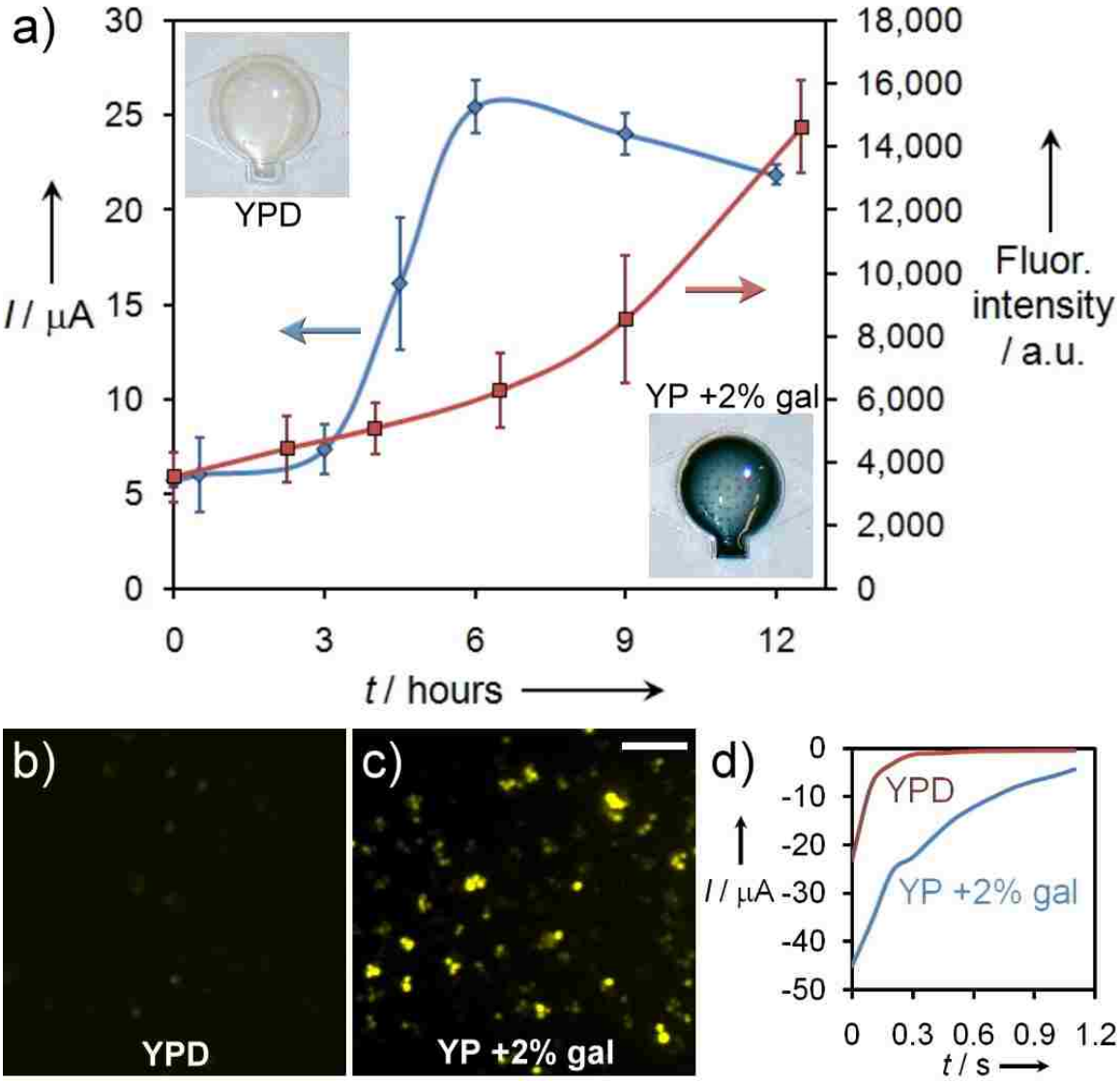

Figure 2. Orthogonal biosensing of a single model analyte *via* fluorescent, electrochemical, and visible (colorimetric) detection modes. *S. cerevisiae* cells engineered to express either YFP or GOx in response to galactose (gal) were co-encapsulated in a glycerol-silica matrix thin film within an ITO-glass/plastic laminate cartridge. a) Simultaneous electrochemical (blue) and fluorescence (red) measurements upon treatment with YP +2% gal at 30 °C. Error bars are the standard deviation of 3 independent measurements. Insets: Photographs of colorimetric assay results following overnight incubation of wells with YPD (negative control) or YP +2% gal at 30 °C. Fluorescence microscopy images (b, c) of YFP expression following an overnight treatment with (b) YP +2% gal or (C) YPD at 30 °C. (False-colored, scale bar = 30 μm). d) Chronoamperometric measurements of H_2O_2 (produced by GOx turnover) following treatment with YPD (red) or YP +2% gal (blue) for 9 hours at 30 °C. ITO working electrodes were selectively modified with gold nanoparticles and Prussian blue to improve H_2O_2 sensitivity while remaining transparent (see Supporting Information, Figure S3).

Typical fluorescent and amperometric responses to treatment with galactose in complex media are shown in Figures 2b and 2d. Bright fluorescence was observed for glycerol-silica matrix encapsulated cells in an ITO-glass/plastic laminate cartridge treated with YP +2% gal (Figure 2b). A similar response was also observed electrochemically. The current response 200 ms after a potential step to –100 mV was 35.6 μA for encapsulated cells in an ITO-glass/plastic laminate cartridge treated with YP +2%gal. The high selectivity of the engineered stains for galactose over the monosaccharide epimer, glucose (negative control), in complex media is shown in Figures 2b and 2d. Encapsulated cells treated with YPD (2% glucose) showed very little background fluorescence (Figure 2c), and only 7.2 μA of electrochemical signal was observed 200 ms after a potential step to –100 mV. These results show the exceptional selectivity possible with genetically engineered cell-based biosensors in this system. The galactose concentration dependence of amperometric and fluorescent signals was also measured and is presented in Figures S4a and S4b, respectively.

Colorimetric detection of galactose from YFP and GOx expressing *S. cerevisiae* cells entrapped in an ITO-glass/plastic laminate cartridge was also demonstrated (Figure 2a, insets). Colorimetric assay solution (ABTS assay, see Supporting Information) was added to each well following an overnight incubation with YPD or YP +2% gal. Following colorimetric assay, the solution and silica matrix remained clear in the well treated with YPD. For the well treated with YP +2% gal, the solution and silica matrix developed a strong dark green-blue color that was clearly discernable by eye. This provides an additional orthogonal approach for the detection of the target analyte that can be performed and measured without any instrumentation, significantly simplifying leave-

behind environmental monitoring. Photographs and absorbance measurements for ABTS assays following incubation with YP containing differing concentrations of galactose are presented in Figure S5, and Table S1.

We further demonstrated the ability to co-entrap disparate classes of living cells within an ITO-glass/plastic laminate cartridge. In this case, eukaryotic *S. cerevisiae* cells engineered to express YFP in the presence of galactose, and gram-negative prokaryotic *E. coli* 'riboswitch' cells, were co-immobilized in a glycerol-silica matrix thin film. As an improvement to our earlier fluorescence resonance energy transfer (FRET) based riboswitch construct,[16] the riboswitch *E. coli* system used in this work contains a synthetic riboswitch: an mRNA strand consisting of an aptamer sequence against the respiratory drug, theophylline, and a sequence encoding a new green fluorescent protein from amphioxus *Branchiostoma floridae* (GFPa1).[17] In the absence of theophylline, this mRNA strand forms a hairpin loop, preventing access to, and translation of, the GFPa1 sequence. In the presence of theophylline, the aptamer sequence binds the drug, exposing the GFPa1 sequence for translation, resulting in a strong GFP signal.

Multianalyte detection from the co-entrapped *S. cerevisiae* and *E. coli* cells is shown in Figure 3. Treatment of the cells in the cartridge with 2% galactose and/or 3.5 mM theophylline in complex medium (YP) resulted in strong YFP and/or GFP fluorescence. Fluorescence intensities and images of the responses clearly show the cell-based sensor successfully distinguished between the two targets. Also apparent is a slightly higher background signal for the YFP expressing *S. cerevisiae* cells which is attributed to 'leaky promoter' expression in cells from stationary phase culture.[14] The lower GFP background obtained from the riboswitch *E. coli* cells is inherent of the tighter

synthetic riboswitch-based regulation over fluorescence.[16] These results further demonstrate that both classes of disparate cells remain viable and active, even when immobilized together at intimate proximities within the glycerol-silica matrix. Similar results would not be expected under standard culture conditions as the cell line with the greater metabolic advantage would quickly overrun the culture.

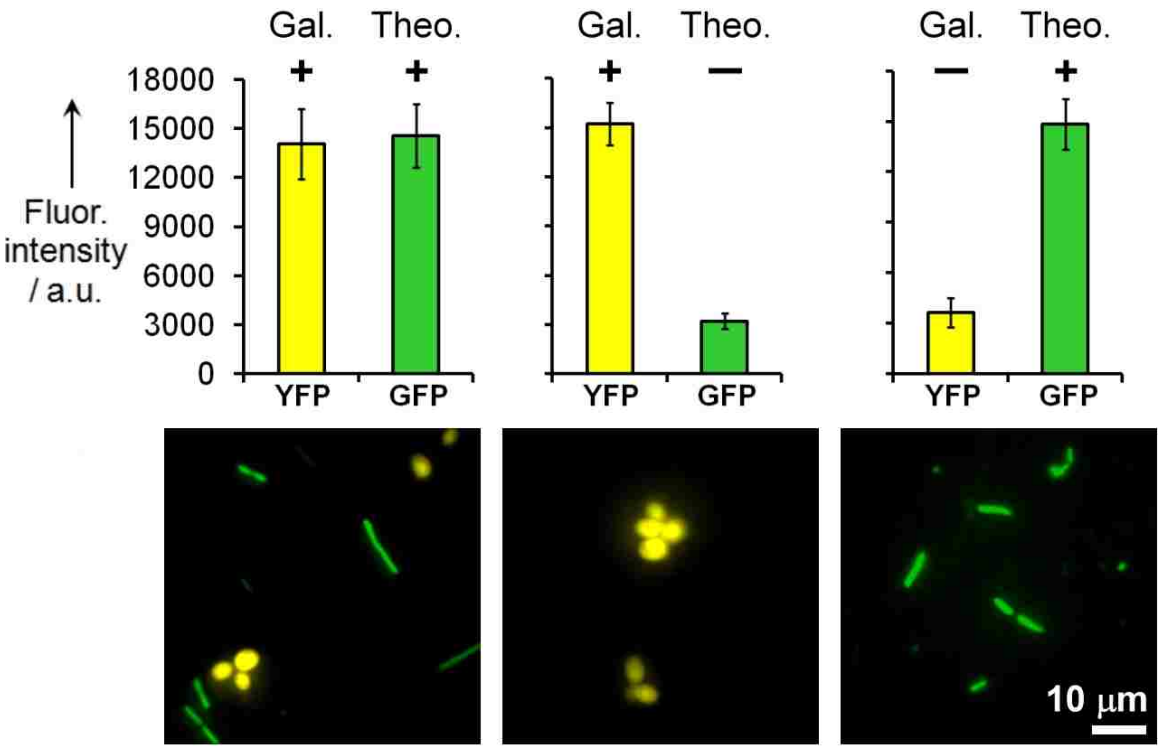

Figure 3. Multianalyte biodetection *via* co-encapsulation of eukaryotic and bacterial cells in a glycerol-silica matrix thin film within an ITO-glass/plastic laminate cartridge. Exposure of *S. cerevisiae* cells to galactose induces YFP expression. Exposure of *E. coli* 'riboswitch' cells to theophylline (theo) results in GFP expression. Treatment in YP with (+) or without (–) 2% gal. and/or 3.5 mM theo. for 17 hours at 30 °C. Fluorescence images are false-colored. Error bars are the standard deviation of 3 independent measurements.

Finally, the glycerated silicate based immobilization matrix chosen for this study provides for long-term stability of the entrapped cells. We have previous reported that use of this matrix with *S. cerevisiae* cells from stationary phase cultures could potentially allow 'leave behind' environment monitoring sensors to operate for over 2 months, after which time the sensors can be collected, analyzed, and replaced.[14] We expect the less complex prokaryotic *E. coli* cells encapsulated within this matrix to demonstrate greater long-term viability and activity than *S. cerevisiae* cells.

CONCLUSIONS

In summary, we have demonstrate for the first time the orthogonal fluorescent, electrochemical, and colorimetric cell-based detection of a target analyte in complex media, with high specificity, using a single device. Coupling these three signal transduction methods provides complementary information regarding the sample properties, potentially reducing the impact of interferants from complex samples, and substantially increasing the confidence of the analyst in the sensor's output. We also showed the first co-entrapment in a silica matrix of eukaryotic and prokaryotic cells which remained viable and responsive, facilitating multianalyte measurements within the ITO-glass/plastic laminate cartridge. These advances in cell-based biosensing hold significant implications towards the development of practical devices for environmental monitoring and open intriguing opportunities for integrating living cells with nanomaterials and macroscale systems.

References

[1] F. Lagarde, N. Jaffrezic-Renault, *Anal. Bioanal. Chem.* 2**011**, *400*, 947-964.

[2] I. J. Allan, B. Vrana, R. Greenwood, G. A. Mills, B. Roig, C. Gonzalez, *Talanta* **2006**, *69*, 302-322.

[3] X. Xu, Y. Ying, *Food Rev. Int.* **2011**, *27*, 300-329.

[4] L. Su, W. Jia, C. Hou, Y. Lei, *Biosens. Bioelectron.* **2011**, *26*, 1788-1799.

[5] D. A. Stenger, G. W. Gross, E. W. Keefer, K. M. Shaffer, J. D. Andreadis, W. Ma, J. J. Pancrazio, *Trends Biotechnol.* **2001**, *19*. 304-309.

[6] Y. Lei, W. Chen, A. Mulchandani, *Anal. Chim. Acta* **2006**, *568*, 200-210.

[7] S. Belkin, *Curr. Opin. Microbiol.* **2003**, *6*, 206-212.

[8] T. H. Rider, M. S Petrovick, F. E. Nargi, J. D. Harper, E. D. Schwoebel, R. H. Mathews, D. J. Blanchard, L. T. Bortolin, A. M. Young, J. Chen, M. A. Hollis, *Science*, **2003**, *301*, 213-215.

[9] K. H. Gilchrist, L. Giovangrandi, R. H. Whittington, G. T. A. Kovacs, *Biosens. Bioelectron.* **2005**, *20*, 1397-1406.

[10] M. S. Petrovick, F. E. Nargi, T. Towle, K. Hogan, M. Bohane, D. J. Wright, T. H. MacRae, M. Potts, R. F. Helm, *Biotechnol. Bioeng.* **2010**, *106*, 474-481.

[11] C. Amatore, S. Arbault, Y. Chen, C. Crozatier, F. Lamaître, Y. Verchier, *Angew. Chem. Int. Ed.* **2006**, *45*, 4000-4003.

[12] A. Meunier, O. Jouannot, R. Fulcrand, I. Fanget, M. Bretou, E. Karatekin, S. Arbault, M. Guille, F. Darchen, F. Lemaître, C. Amatore, *Angew. Chem. Int. Ed.* **2011**, *50*, 5081-5084.

[13] K. Buonasera, G. Pezzotti, V. Scognamiglio, A. Tibuzzi, M. T. Giardi, *J. Agric. Food Chem.* **2010**, *58*, 5982-5990.

[14] J. C. Harper, D. M. Lopez, E. Larkin, M. K. Economides, S. K. McIntyre, T. M. Alan, M. S. Tartis, M. Werner-Washburne, C. J. Brinker, S. M. Brozik, D. R. Wheeler, *Chem. Mater.* **2011**, *23*, 2555-2564.

[15] T. L. Edwards, J. C. Harper, R. Polsky, D. M. Lopez, D. R. Wheeler, A. C. Allen, S. M. Brozik, *Biomicrofluidics* **2011**, *in review*.

[16] S. Harbaugh, N. Kelley-Loughnane, M. Davidson, L. Narayanan, S. Trott, Y. G. Chushak, M. O. Stone, *Biomacromol.* **2009**, *10*, 1055-1060.

[17] E. K. Bomati, G. Manning, D. D. Deheyn, *BMC Evol. Biol.***2009**, *9*, 77.

SUPPORTING INFORMATION

Experimental Methods

Materials and Reagents

Aqueous solutions were prepared with 18 MΩ water using a Barnstead Nanopure water purifier (Boston, MA). Tetraethylorthosilicate (TEOS), glycerol (anhydrous), titanium isopropoxide (97%), potassium ferricyanide ($Fe(CN)_6$), gold potassium cyanide ($Au(CN)_2$), glucose (99%), galactose (99%), potassium chloride (KCl), theophylline (99%), ampicillin sodium salt, peroxidase (from horseradish), and Indium Tin Oxide (ITO) coated glass microscope slides (30-60 Ω/sq) were purchased from Sigma-Aldrich (St. Louis, MO). 2,2'-Azinobis [3-ethylbenzothiazoline-6-sulfonic acid]-diammonium salt (ABTS, 10mg tablets), phosphate buffer saline (PBS) solution, pH 7.2 (11.9 mM phosphates, 137 mM NaCl, and 2.7 mM KCl at 1× concentration), sodium phosphate (monobasic and dibasic), 30% hydrogen peroxide (H_2O_2), hydrochloric acid (HCl), sulfuric acid (H_2SO_4), acetone, ammonium hydroxide, ferric chloride ($FeCl_3$) solution (40% w/v), and yeast extract were obtained from Fischer Scientific (Pittsburgh, PA). Bacto™ Peptone and Bactro™ Tryptone were from BD Biosciences. Difco Luria-Bertani (LB) was purchased from Becton Dickinson and Company (Sparks, MD). All reagents were used as received.

Culture Mediums and Cell Preparation

Yeast extract, peptone, dextrose (YPD) media contained 10 g yeast extract, 20 g Bacto™ peptone, and 20 g of glucose per 1 L of nanopure water. In yeast extract, peptone, galactose (YP +2% gal) induction medium, the 20 g of glucose in the YPD recipe was replaced with 20 g of galactose. In studies where the concentration of galactose was varied, the concentration of all other components (YP) remained constant. LB broth contained 10 g bactro-tryptone, 5 g yeast extract, 10 g NaCl, and 1 g ampicillin per 1 L of nanopure water.

A single colony of *S. cerevisiae* was inoculated into 3 ml of YPD media in a 15 mL culture tube. This solution was cultured at 30°C in a shaking incubator at 250 rpm until stationary phase (7-10 days). A single colony of *E. coli* was inoculated into 35-40 mL of LB media in a 250 mL flask. This inoculated solution was cultured in a shaking incubator at 250 rpm to stationary phase (18-24 hrs) at 37 °C.

Synthesis of Poly(Glycerol) Silicate (PGS)[1,2]

A round-bottomed flask equipped with a stir bar, dropping funnel, and reflux condenser was charged with 63.4 g of glycerol (688 mmol) and heated to 60 ºC with stirring. To the hot glycerol was added a mixture of 10.21 g TEOS (49.0 mmol) and 1.02 g titanium isopropoxide (3.0 mmol). After addition, the reaction mixture was refluxed at 130 ºC for 3 hours. Ethanol co-product was removed under vacuum (~10 mTorr) at 130 ºC. The product (63.5g; 98% yield) was a viscose opalescent white liquid that was somewhat soluble with water. The mass of the product agreed with the reported

theoretical formula: $Si(C_3H_7O_3)_4 \cdot 10C_3H_8O_3$;[33] however, it is certain that many isomers exist in the mixture as well as some inadvertent hydrolysis products.

ITO-Glass/Plastic Laminate Cell-Based Biosensing Cartridge

The ITO electrochemical cell sensor array was integrated into a plastic package which included microfluidic channels allowing a silica matrix thin film to be cast between the ITO electrode surface and the porous well bottom (390 mL volume). The integrated system is referred to as a cartridge with overall size of $(5 \times 50 \times 75)$ mm^3, and is shown schematically in Figures 1a, S1 and S2. The cartridge was fabricated by laminating laser-cut layers of polyethyleneterapthalate (PET, Mylar) and polymethylmethacrylate (PMMA), and final adhesion to a ITO coated glass microscope slide. The basic fluidic channel was made by cutting the channel pattern using a CO_2 laser ablation system (Model PLS 6.75 with a 60 watt cartridge, Universal Laser Systems, Scottsdale, AZ) into a custom sheet of PET double-side coated with pressure sensitive acrylic-based adhesive (0.05 mm thick for the PET and 0.025 mm thick for each adhesive; Fralock, Valencia, CA) forming the side walls and defining the channel's three dimensions. The top and bottom walls were formed from plain PET (0.1 mm thick). Into one or both of these plain PET sheets fluidic vias were cut to allow for access to external tubing or channels located above or below. Alignment of the layers was accomplished with registration holes and pins. The layers were pressed together between two flat steel plates in a hydraulic press.

Individually addressable working, pseudo-reference, and counter electrodes at the bottom of each well were defined by etching ITO through a photolithography defined

photoresist mask. The ITO electrodes were fabricated from commercially available ITO coated glass microscope slides (part no. 636908, Sigma-Aldrich, St. Louis, USA). The ITO thickness was specified at 300-600 Angstroms (30-60 ohms per square). AZ4110 positive tone photoresist was spin coated onto the slide at 4000 rpm for 30 seconds and then baked on a hotplate at 90°C for 90 seconds. The resist was exposed to a broad UV light source of 200 mJ/cm^2 and subsequently developed in AZ400k (5:1 dilution in DI water) for two minutes. The ITO was etched in 18% hydrochloric acid for five minutes at room temperature. The photoresist mask was then removed using acetone and cleaned with an isopropanol and DI water rinse.

The fluidic fixture consisted of nine plastic laminate layers (four PMMA, five PET), an ITO coated glass slide, and a set of O-rings. Each of these layers is number from zero to nine starting at the glass slide, and is shown in detail in Figure S1. In Figure 1 only layers 0-5 are shown exploded, without the O-rings, for simplicity. Layers 2, 3, 5, and 6 were PET with single- (M-A) or double-sided (A-M-A) adhesive. Layer 4 was 0.5 mm thick PMMA. Layers 0, 7, and 9 were 1.5 mm thick PMMA supports. Layer 7 housed six O-rings (silicone, AS568A-002, *McMaster-Carr,* Santa Fe Springs, CA) for receiving 1/16 inch diameter rigid PEEK or PTFE tubing to introduce and remove liquid samples at low pressures (tested to be leak free up to at least 90 psi) without the need for additional fittings. Electrical connections from the hand-held potentiostat to layer 0 were made using a 10-conductor card-edge connector and ribbon cable assembly (*3M*, St. Paul, MN).

The primary channel which delivered and contained the cells in sol-gel was located in layer 3 with dimensions of 100 microns thick and entrance/exit regions

combined volume of 10 microliters. Layer 2 defined the circular well over the three electrodes of layer 0. This well depth was 175 microns with a total volume of 20 microliters. The upper wall of the channel and well botoom was layer 4, made from PMMA. In this layer, located over the electrodes and electrode well, an array of 81 holes (approximately 50 microns in diameter) was laser ablated to form a “shower head” pattern. Prior to the introduction of the sol-gel the shower head was capped with PET layer 5. This prevented the cell/sol-gel precursor solution from leaking through the porous region of layer 4, and allowed for long-term storage of the entrapped cells under ambient conditions without evaporation. Prior to introducing the analyte solution to the cartridge well, the cap was removed to allow liquid reagents to be effused through the porous well bottom into the gel (locally over the electrodes) without disruption of the gel.

The laminates were assembled in the following order, starting with layer 8: 9, 7, 6, 4, 5, 3, 2, and 1. After the addition of one or more layers, they were pressed at approximately 3000 psi at room temperature for 2 minutes in a manual hydraulic laboratory press (Model 3850, *Carver, Inc.*, Wabash, IN). In the final step, layer 0 was pressed at a reduced pressure of 500 psi for 2 minutes to prevent cracking of the glass layer. A custom fixture, to ensure alignment of layers and uniform force distribution, was fabricated from two plates of 1/4 inch steel with surfaces machined and polished flat. Complete assembly of the cartridge from the prepared layers required 45 minutes.

Functionalization of ITO Working Electrodes with AuNPs and PB

Prior to assembly in the plastic laminate cartridge, patterned ITO electrode array microscope slides were cleaned via successive sonication in dilute ammonia (1:1 (vol.)

nanopure H_2O : ammonium hydroxide), nanopure H_2O, acetone, and nanopure H_2O, for 5 minute each at room temperature (22 ºC). Between sonication steps the glass slides were rinsed in nanopure H_2O and dried with a stream of N_2. Following cleaning, the slides were assembled into the plastic laminate cartridge or stored in nanopure H_2O for up to 12 hours.

Gold nanoparticles (AuNPs) were electrochemically deposited onto the clean ITO working electrodes using a method modified from Wang et al.[3] To 10 mL of sodium phosphate buffer (10 mM, pH 7.0) was added 600 μL of 2.0 mM $KAu(CN)_2$ in nanopure H_2O (end concentration 110 μM). This solution was introduced to a given three electrode cell in the ITO-glass/plastic laminate cartridge via the microfluidic channel inlet port. AuNP electrodeposition occurred by cyclic voltammetry from –0.5 to –1.4 V vs. ITO pseudo-reference at room temperature (without deoxygenation) for 20 cycles at a potential scan rate (v) of 50 $mV \cdot s^{-1}$. Following electrodeposition the channel was flushed with ~3 mL of nanopure H_2O, followed by a stream of air to vacate the channel.

Prussian blue (PB) was deposited onto the AuNP modified ITO working electrode using a method modified from Qiu et al.[4] A solution with 1.0 mM $FeCl_3$, 1.0 mM $Fe(CN)_6$, 0.1 M KCl, and 0.025 M HCl in nanopure H_2O was introduced to a given three electrode cell in the ITO-glass/plastic laminate cartridge *via* the microfluidic channel inlet port, and incubated at room temperature for 30 minutes. Following deposition the channel was flushed with ~3 mL of nanopure H_2O, followed by a stream of air to vacate the channel.

Encapsulation of S. cerevisiae and/or E. coli in PGS Derived Silica Thin Films

For orthogonal mode biodetection, silica matrix precursor solutions were prepared by first adding an equal molar mixture of *S. cerevisiae* cells engineered to express YFP, and *S. cerevisiae* cells engineered to express and secrete GOx (total concentration 10^6-10^7 cells/mL), to 100 mM sodium phosphate buffer, pH 6.0. This cell/buffer solution was added to the PGS in a 1:1 volume ratio to a final volume of 500-750 μL in a 1.5 mL polypropylene microcentrifuge tube, and homogenized by vortexing for 60 seconds. The solution was aged for 30 minutes at room temperature (22 ºC), and then transferred into the ITO-glass/plastic laminate *via* a syringe interfaced to an inlet port by a plastic tube (1/16 inch o.d.). By allowing the solution to age before introducing it to the device the *S. cerevisiae* cells remained homogenously dispersed throughout the silica matrix upon gelation. Otherwise, *S. cerevisiae* cells were observed to settle to the bottom of the microfluidic channel, reaching an undesirably high density on top of the ITO electrodes upon silica matrix gelation. Once loaded, the tube was removed and the inlet and outlet ports were sealed with adhesive tape. Cell/buffer/PGS solution gelation occurred less than 30 minutes after introduction to the device. This was confirmed by monitoring gelation of the remaining cell/buffer/PGS solution not introduced to the cartridge.

For disparate cell co-entrapment and multianalyte detection, the cell/buffer solution contained *S. cerevisiae* cells engineered to express YFP and *E. coli* cells engineered to display green fluorescence, at a ratio of approximately 1:2 (*S. cerevisiae* cells to *E. coli* cells) in 100 mM sodium phosphate buffer, pH 6.0. There was no other change to the procedure as described above.

ABTS Assay

2, 2'-azino-bis [3-ethyl-benzothiazoline-6-sulfonic acid] (ABTS) assay was modified from Sun, et al.[5] The ABTS working solution consisted of 100 mM sodium phosphate buffer, pH 7.0, 50 mM glucose, 3 units of horseradish peroxidase (HRP), and 2 mg/mL ABTS. Following analyte solution treatment of the silica matrix entrapped cells beneath a given well in the ITO-glass/plastic laminate cartridge, the analyte solution was discarded and replaced with 250 μL of ABTS working solution. Incubation with ABTS working solution proceeded overnight at room temperature (22 °C). The wells were then imaged with a digital camera and ABTS solution was collected and absorbance was measured at 410 nm using a microplate UV/Vis spectrophotometer.

Electrochemical Instrumentation; Fluorescence and Scanning Electron Microscope Imaging

All electrochemical measurements were performed on a PalmSens hand-held potentiostat (Palm Instruments BV, The Netherlands) using the on-chip ITO working, ITO pseudo-reference, and ITO counter electrodes. Fluorescence microscopy imaging was performed on a Zeiss Axiovert 200M inverted microscope (Germany) and recorded using a Zeiss monochrome high resolution camera (AxioCam HRm). SEM imaging was performed by a Hitachi 3200N scanning electron microscope operating at 25 kV.

ITO Working Electrode Functionalization and Characterization

Hydrogen peroxide (H_2O_2) electrochemistry is unfavored on indium tin oxide (ITO) surfaces. To enhance the electrochemical signal from H_2O_2 while maintaining an optically transparent surface for fluorescence measurements, gold nanoparticles (AuNPs) were deposited from a solution of potassium gold cyanide onto the ITO working electrode (see Experimental Methods, above). Following electrodeposition, the AuNP modified ITO surface changed from a dull brown to a light pink, as shown in Figure S3a. This characteristic color shift is due to surface plasmon resonance coupling of the deposited AuNPs. Scanning electron microscope (SEM) images of the bare ITO surface, and the ITO-AuNP surface, are shown in Figure S3b and S3c, respectively. Images reveal mostly spherical AuNPs evenly distributed across the ITO surface with diameters from 10 to 75 nm, with larger particles being more globular in structure.

Cyclic voltammograms in H_2SO_4 solution prior to and after AuNP deposition are shown in Figure S3e. The current response from a bare ITO electrode (blue trace) was nearly flat, as expected for a clean ITO surface. Following AuNP deposition (red trace), an oxidation wave centered near 845 mV (vs. ITO pseudo-reference), and reduction peak at –455 mV, were observed. These waves are attributed to oxygen absorption (oxidation wave) and desorption (reduction wave) on the AuNP surface. Integration of the reduction wave provides the total charge transferred upon oxygen desorption, which is directly proportional to the electroactive surface area of Au, according to the relation of 400 $\mu C \cdot cm^{-2}$ as reported by Woods.[6] The charge measured from the reduction wave shown in Figure S3e \was 7.49 μC, which corresponds to a AuNP electroactive surface area of

1.875 mm^2. This accounts for less than 8% of the ITO working electrode surface area, which thus retains excellent optical transparency.

Following AuNP modification of the ITO electrode, the surface was functionalized with Prussian blue (PB). Often described as an "artificial peroxidase,"[4] PB can significantly enhance H_2O_2 reduction while being more stable than enzymes used for the same purpose. Incubation of the 3 electrode cell surface with a solution of $FeCl_3$, $Fe(CN)_6$, KCl and HCl (see Experimental Methods) resulted in AuNP catalyzed deposition of PB onto the ITO-AuNP working electrode only. A characteristic change in color to dull blue was observed for the working electrode, as shown in Figure 3a. Deposition of PB onto the AuNPs involves the reduction of free ferric ions, or ferric ions in the CN complex, as shown in reaction (1).[4] This reaction is thermodynamically unfavorable due to the standard free-energy change of +173 kJ/mol. Gold substrates, however, can act as catalysts for reaction (1).[7] This results in iron(II) molecules that can proceed to PB via reaction (2).

$$Fe^{3+} + ½\ H_2O = ¼\ O_2 + H^+\ Fe2^+ \quad (1)$$

$$K^+ + Fe^{2+} + Fe(CN)_6^{3-} = KFe(III)[Fe(II)(CN)_6] \quad (2)$$

SEM images of the ITO-AuNP-PB surface reveal a microcrystalline structured network with features on the order of 100 nm in diameter (Figure S3d). The ITO-AuNP-PB surface also retained excellent optical transparency allowing for fluorescence measurements of YFP expressing *S. cerevisiae* cells through the electrodes.

The current response following a 1 second potential step to –100 mV (vs. ITO pseudo-reference) for each of these surfaces in 1× PBS containing 1 mM H_2O_2 is shown in Figure S3f. A significant increase in H_2O_2 reduction current was observed for the ITO-AuNP-PB surface (blue trace) vs. the ITO-AuNP (red trace) and bare ITO (green) trace, with currents of –50.9, –9.1, and –0.4 μA, respectively (200 ms from potential step initiation). The current from H_2O_2 reduction obtained from the ITO-AuNP-PB surface was sufficient to allow detection of H_2O_2 generated by GOx expressed and secreted by *S. cerevisiae* cells used in this study. This same chronoamperometric protocol was applied hourly following introduction of analyte solution during the orthogonal fluorescence and electrochemical measurement experiments.

References

[1] T. Khonina, O. Chupakhin, L. Larionov, T. Boyakovskaya, A. Suvorov, E. Shadrina, *Pharm. Chem. J.* **2008**, *42*, 609-613.

[2] J. C. Harper, D. M. Lopez, E. Larkin, M. K. Economides, S. K. McIntyre, T. M. Alan, M. S. Tartis, M. Werner-Washburne, C. J. Brinker, S. M. Brozik, D. R. Wheeler, *Chem. Mater.*, **2011**, *23*, 2555-2564.

[3] J. Wang, L. Wang, J. Di, Y. Tu, *Talanta* **2009**, *77*, 1454-1459.

[4] J.-D. Qiu, H.-Z. Peng, R.-P. Liang, J. Li, X.-H. Xia, *Langmuir* **2007**, *23*, 2133-2137.

[5] L. H. Sun, T. Bulter, M. Alcalde, I. P. Petrounia, F. H. Arnold, *Chembiochem* **2002**, *3*, 781–783.

[6] R. Woods, *Chemisorption at electrodes*. In: Bard, A. (Ed.), Electroanalytical Chemistry. 1976, Marcel Dekker, New York

[7] K. Itaya, I. Uchida, V. D. Neff, *Acc. Chem. Res.* **1986**, *19*, 162-168.

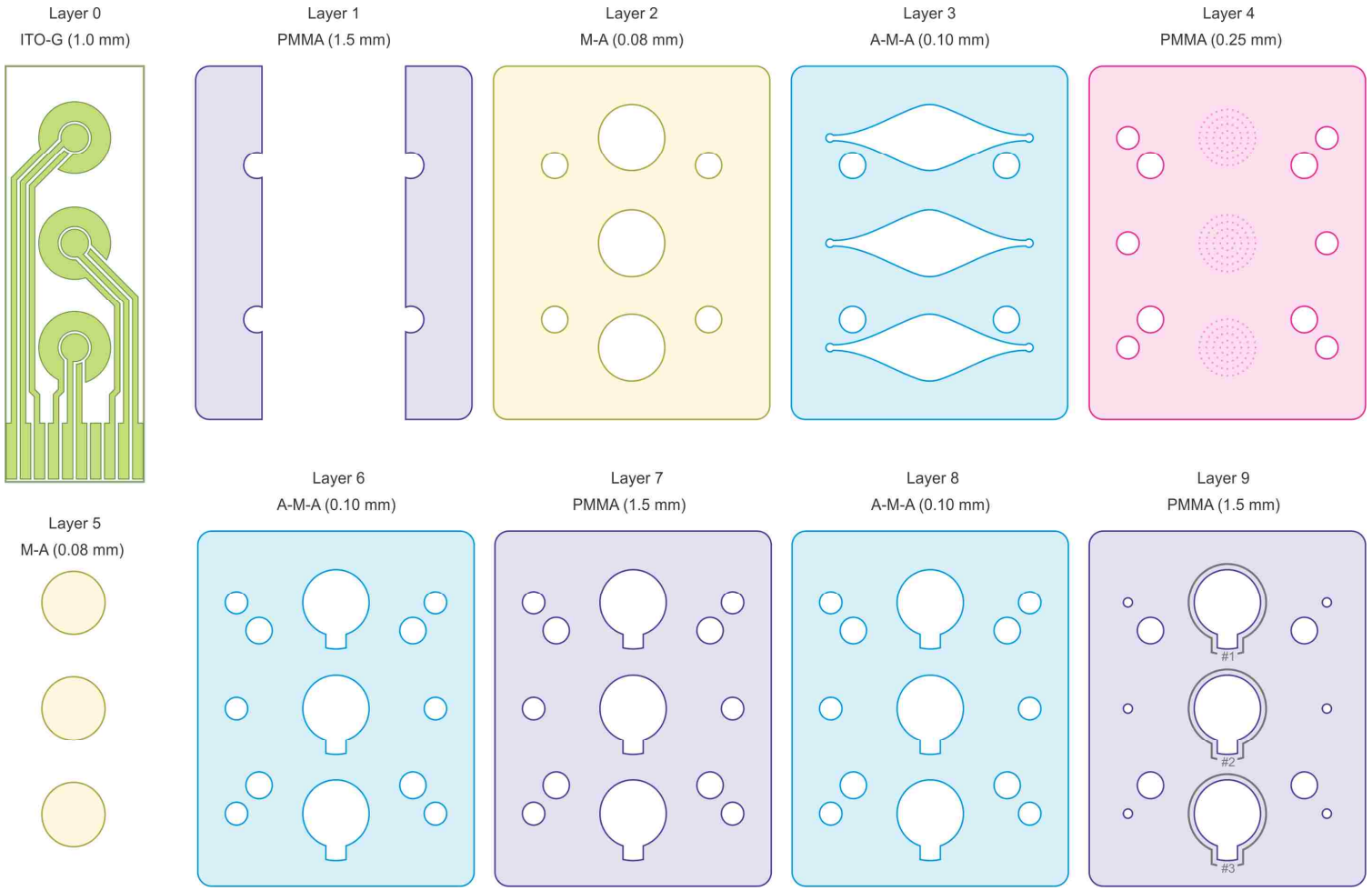

Figure S1. Expanded layer-by-layer schematic of the ITO-glass/plastic laminate cartridge. The four small holes shown in layer 2, and perpetuated through all layers, are used for layer registration/alignment during cartridge assembly. Abbreviations: polymethylmethacrylate (PMMA), polyethyleneterapthalate (Mylar, M), indium tin oxide (ITO), glass (G), Mylar coated with adhesive oriented down (M-A), Mylar coated with adhesive on both sides (A-M-A).

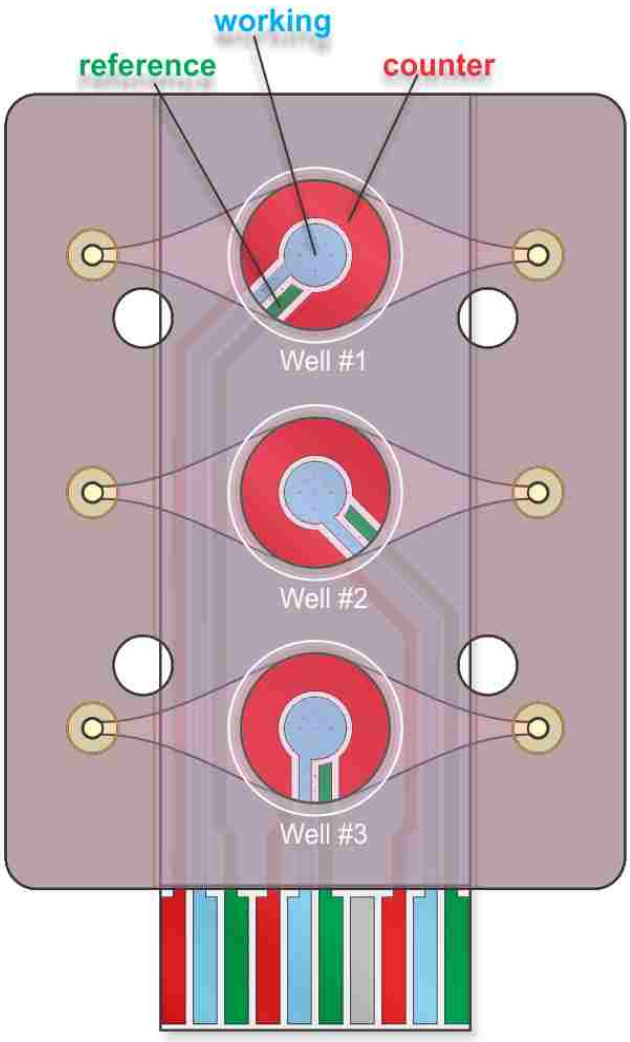

Figure S2. Schematic of assembled laminate cartridge highlighting the working (blue), reference (green) and counter (red) ITO electrode array and leads to the ribbon cable interface. A_{WE} = 22.9 mm^2, A_{RE} = 8.2 mm^2, A_{CE} = 55.1 mm^2, A_{CE}/A_{WE} = 2.5.

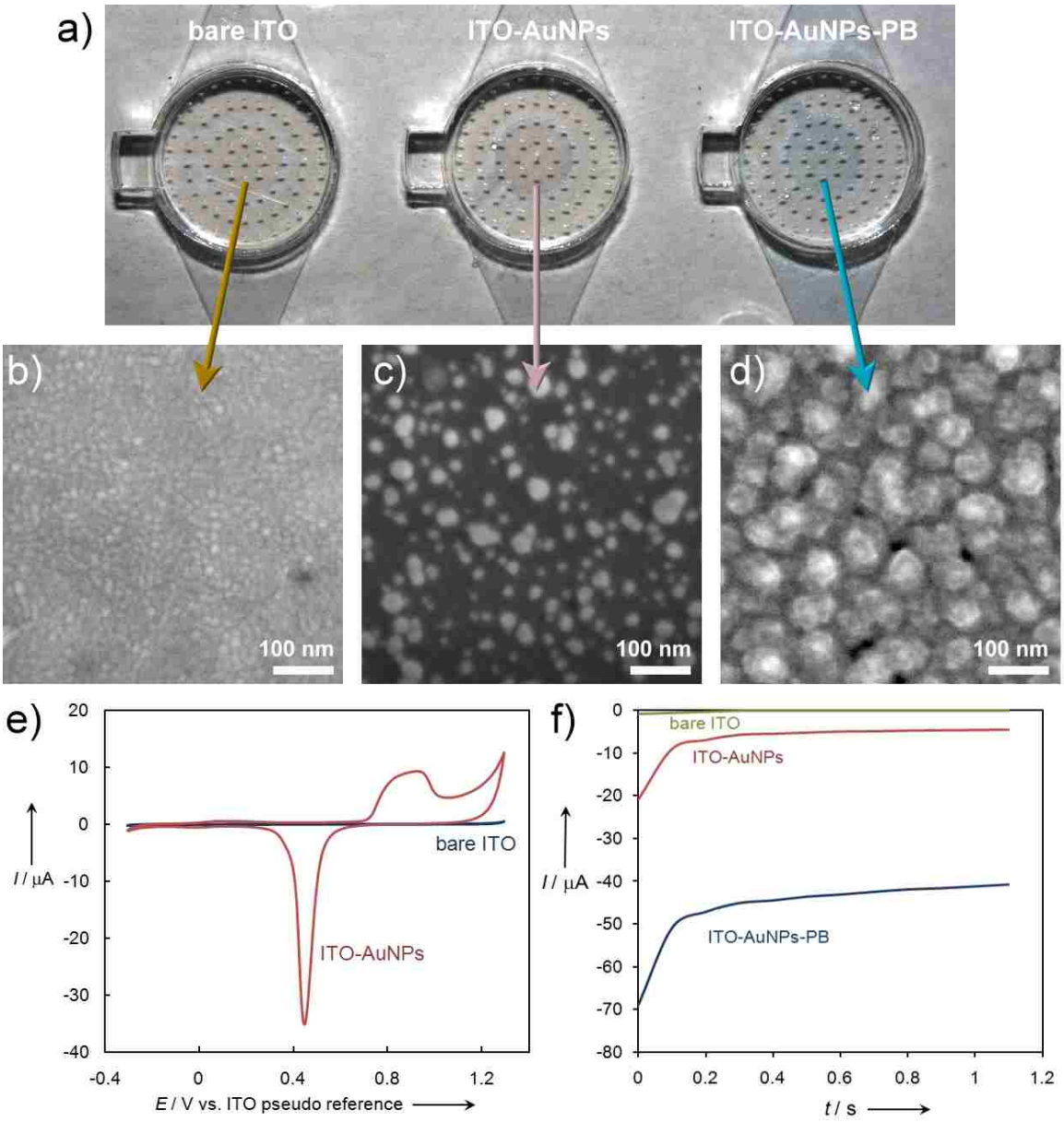

Figure S3. a) Photograph of an ITO-glass/plastic laminate cartridge with a bare ITO WE (left, light brown), a AuNP modified ITO WE (middle, light pink), and a AuNP-PB modified ITO WE (right, dull blue). Image brightness, contrast, and leveling were adjusted to improve color distinction between WEs. SEM images (b-d) of the WEs imaged in panel (a): b) bare ITO, c) AuNP modified ITO, and d) AuNP-PB modified ITO. e) Cyclic voltammograms (CV) of a bare ITO (blue) and a AuNP modified ITO (red) electrode in an ITO-glass/plastic laminate cartridge in 1 M H_2SO_4, v = 100 mV · s^{-1} (second CV sweeps shown). f) Chronoamperometric response of a bare (green), a AuNP modified (red), and a AuNP-PB modified (blue) ITO WE in 1 mM H_2O_2, 1× PBS, pH 7.4. E = –100 mV vs. on-chip ITO pseudo-reference.

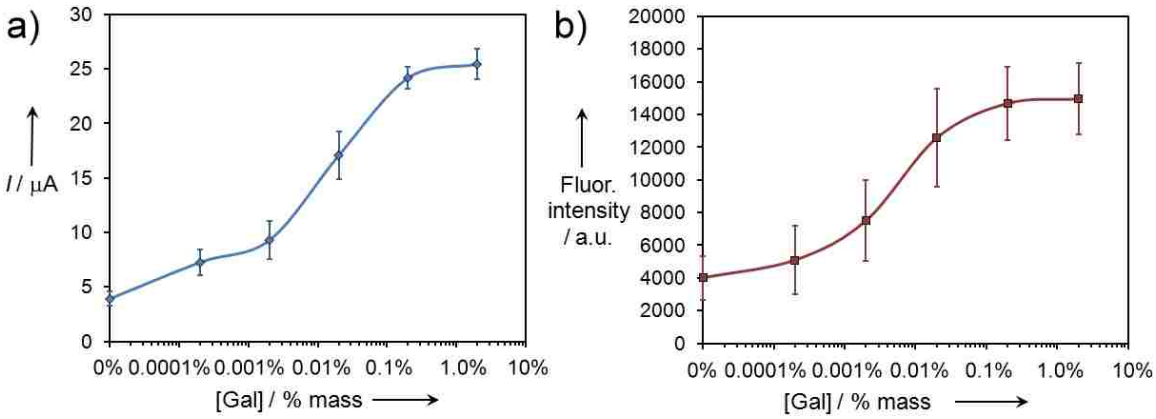

Figure S4. a) Chronoamperometric current response and b) fluorescence intensity from glycerol-silica matrix encapsulated *S. cerevisiae* cells in a ITO-glass/plastic laminate cartridge following treatment with YP +2%, 0.2%, 0.02%, 0.002%, 0.0002% gal, and YPD (0% gal control containing 2% glucose) at 30 °C for 9hrs (a), or overnight (b). Error bars are the standard deviation of 3-5 independent measurements.

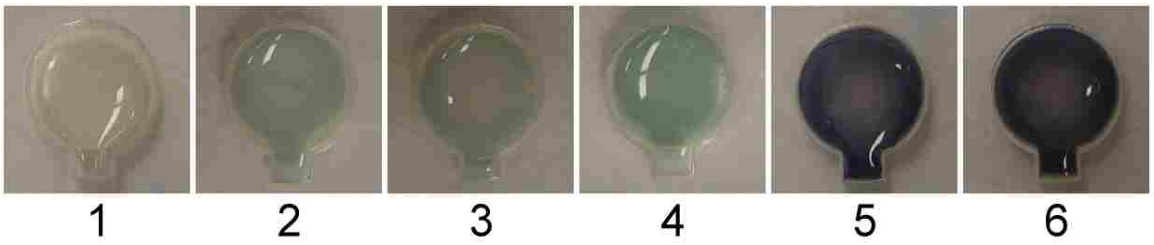

Figure S5. Photographs of ITO-glass/plastic laminate cartridge wells following an overnight ABTS assay at room temperature (22 °C). Glycerol-silica matrix encapsulated *S. cerevisiae* cells were previously exposed to: 1) YPD (0% gal, 2% glucose), 2) YP +0.0002% gal, 3) YP +0.002% gal, 4) YP +0.02% gal, 5) YP +0.2% gal, and 6) YP +2% gal overnight at 30 °C.

Table S1. ABTS assay absorbance measurements (410 nm) per galactose concentration

	Sample ID (corresponds with images in Figure S5)					
	1	2	3	4	5	6
[Gal] / % mass	0 (YPD)	0.0002	0.002	0.02	0.2	2.0
Abs 410 nm / a.u.	0.199	0.324	0.382	0.455	1.201	1.213

CHAPTER 5

Biocompatible Microfabrication for Targted Confinement of Single Cells and Their Progeny

Harper, J. C., Brozik, S. M., Brinker, C. J., Kaehr, B.

Abstract

We demonstrated, for the first time, the selection of a single target cell followed by its *in situ* isolation in a porous 3D protein microchamber formed by biocompatible 2-photon microfabrication. This process permits the selection and isolation of a target cell (+ phenotype) from a population of cells with mixed phenotypes, and the subsequent monitoring of its behavior, and that of its progeny, under well defined conditions. To our knowledge, this cannot be accomplished using any other reported techniques. We further show the growth of diverse cells to densities difficult to achieve using typical *in vitro* techniques and the response of these cells to external stimuli. Finally, we show the ability to impact cell growth and cell-to-cell signaling by tuning the physical properties of the protein microchamber. The possibilities for single-cell analysis afforded by this new technology make it attractive for studying cell noise and heterogeneity, cell-to-cell signaling (i.e. quorum sensing), spontaneous mutation, cell differentiation, and the onset of aging.

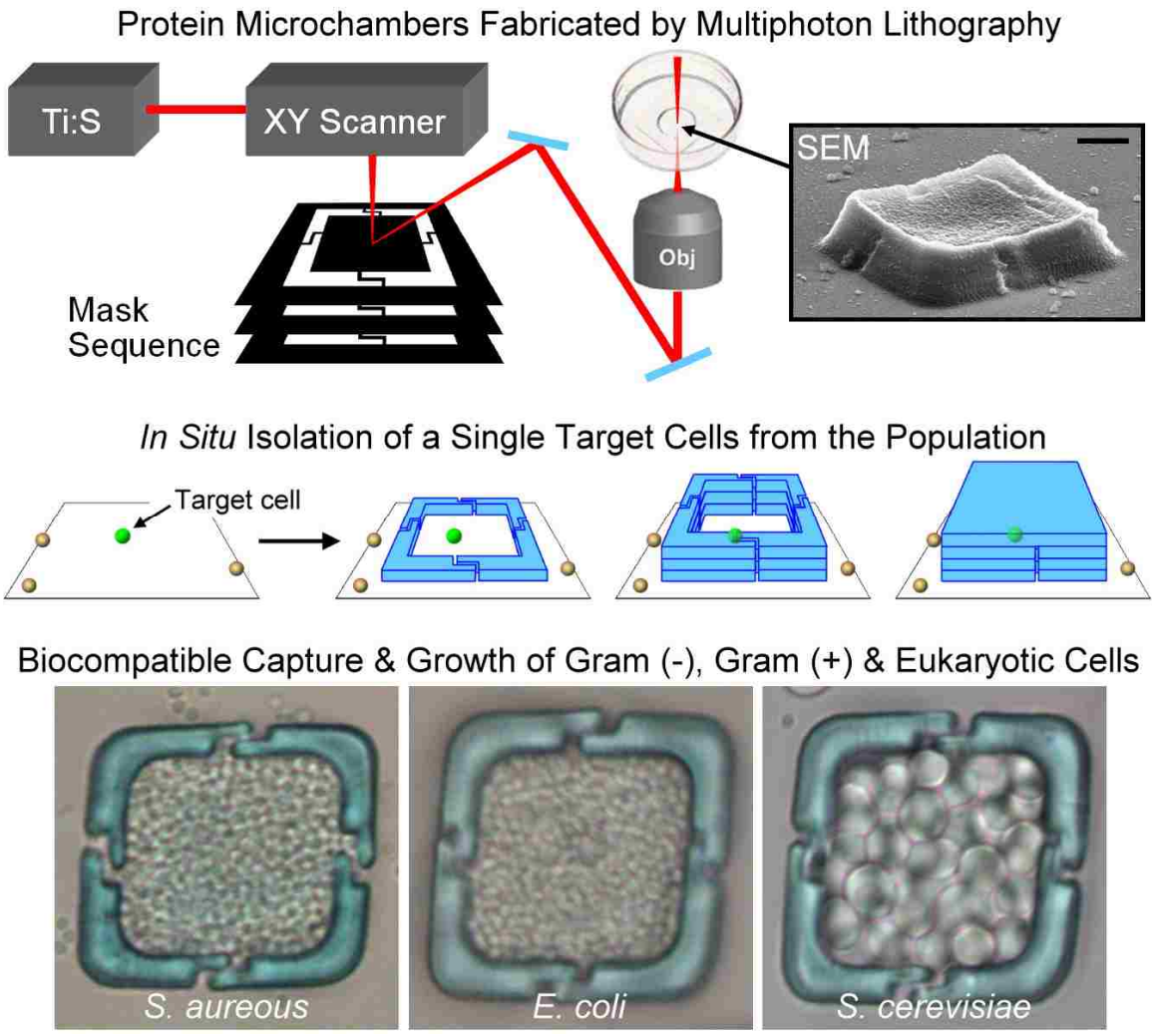

Abstract Figure

INTRODUCTION

The development of technologies and techniques facilitating measurements at the single-cell level has revealed substantial cell to cell variation in genetic and proteomic profiles, enzymatic activity, and response to signals[1,2]. This is expected from stem or progenitor cells which differentiate into specialized phenotypes by altering genetic expression patterns[3]. However, it has been shown that even genetically identical (clonal) cells under *in vitro* culture conditions can be phenotypically diverse[4,5]. Recent studies have proposed that this cell-to-cell variation, also referred to as 'noise', is important in the development and function of many tissues allowing, for example, creation of the retinal mosaic for color vision[6] or preventing harmful bursts of inflammation-triggering molecules[7]. Thus, measuring and identifying cellular heterogeneity is crucial in order to gain a deeper understanding into cellular biology and tissue physiology. As analytical techniques carried out on cell populations 'average out' single cell fluctuations, the importance of developing methods to select and study individual cells and clonal populations is evident.

Several technologies have been developed to enable individual cell selection and study including flow cytometry fluorescence-activated cell sorting (FACS)[8], laser-capture microdissection[9], gene-expression chips[10], mass spectrometry (MS)[11], and microfluidics[12,13]. Increasingly, microfluidic platforms are being used in cell biology as they allow for monitoring the behavior of single cells and their progeny under well defined conditions over time[14,15]. A prime example is the microfluidic chemostat developed by Groisman *et al.* for bacterial and yeast cell study[16]. This device allows

chemostatic and thermostatic culture of cells trapped in polydimethylsiloxane (PDMS) microchambers. Although this device allows for the extended study of cells in a well controlled environment, selecting a specific target cell(s) for study is not possible as initial cell isolation relies on random capture in the microfluidic chambers during loading. The selection of a desired target cell, followed by *in situ* isolation of the cell and its progeny for subsequent analysis, has not been reported.

Herein we demonstrate the isolation of a (single and multiple) target cells using biocompatible three-dimensional microfabrication. This process permits, for the first time, the selection and isolation of a target cell, *in vitro*, from a population of cells with mixed phenotypes, and the subsequent monitoring of its behavior, and that of its progeny, in picoliter environments. Cells can be grown to ultra-high densities in "breathable" hydrogel microchambers that allow external (chemical) probing. This approach enables us to study bacterial inter-cell communication at the single cell level and we show changes in the diffusivity of the microchamber can result in 'self-signaling'. The possibilities for single-cell analysis afforded by this approach make it attractive for studying cell noise and heterogeneity, cell-to-cell signaling (i.e. quorum sensing, host-pathogen response), spontaneous mutation, and cell differentiation.

RESULTS

Fabricaton of microstructures *via* multiphoton lithography

In situ selection and isolation of single target cells (+ phenotype) from a population of cells with mixed phenotypes was performed on an inverted microscope modified with a dynamic mask-based multiphoton lithography (MPL) system. MPL is a direct-write process in which soluble synthetic or natural monomers are solidified at precise 3D coordinates via muliphoton absorption within the focal volume (voxel) of a tighly focused high peak-power pulsed laser beam[17,18] Scanning the laser source across a series of digital masks permits rapid fabrication of highly detailed and complex 3D architectures[19]. The choice of reactants used (i.e. monomers, photosensitizer) for MPL can allow *in situ* formation of scaffolds under physiological conditions in the presence of cells[17]

In situ confinement of eukaryotic cells in protein microchambers

Direct-writing of 3D protein microstructures occurs by cross-linking oxidizable amino acid residues present on proteins in an aqueous solution promoted *via* type I (direct radical) and type II (oxygen-dependent) photosensitizers[20]. We have carefully selected for reagents and conditions that minimize phototoxic effects to allow for fabrication of structures large enough for complete enclosure of target cell(s). As shown in **Fig. 1A**, a single *s. cerevisiae* cell expressing yellow fluorescent protein (YFP) from a population of non-expressing cells was identified and subsequently confined in a protein microchamber (**Fig. 1B, and Movie S1)**. Side ports (chicanes, see **Fig. 1B**) in the walls provide free

diffusion of nutrients and wastes while maintaining a physical barrier between internal and external cells.

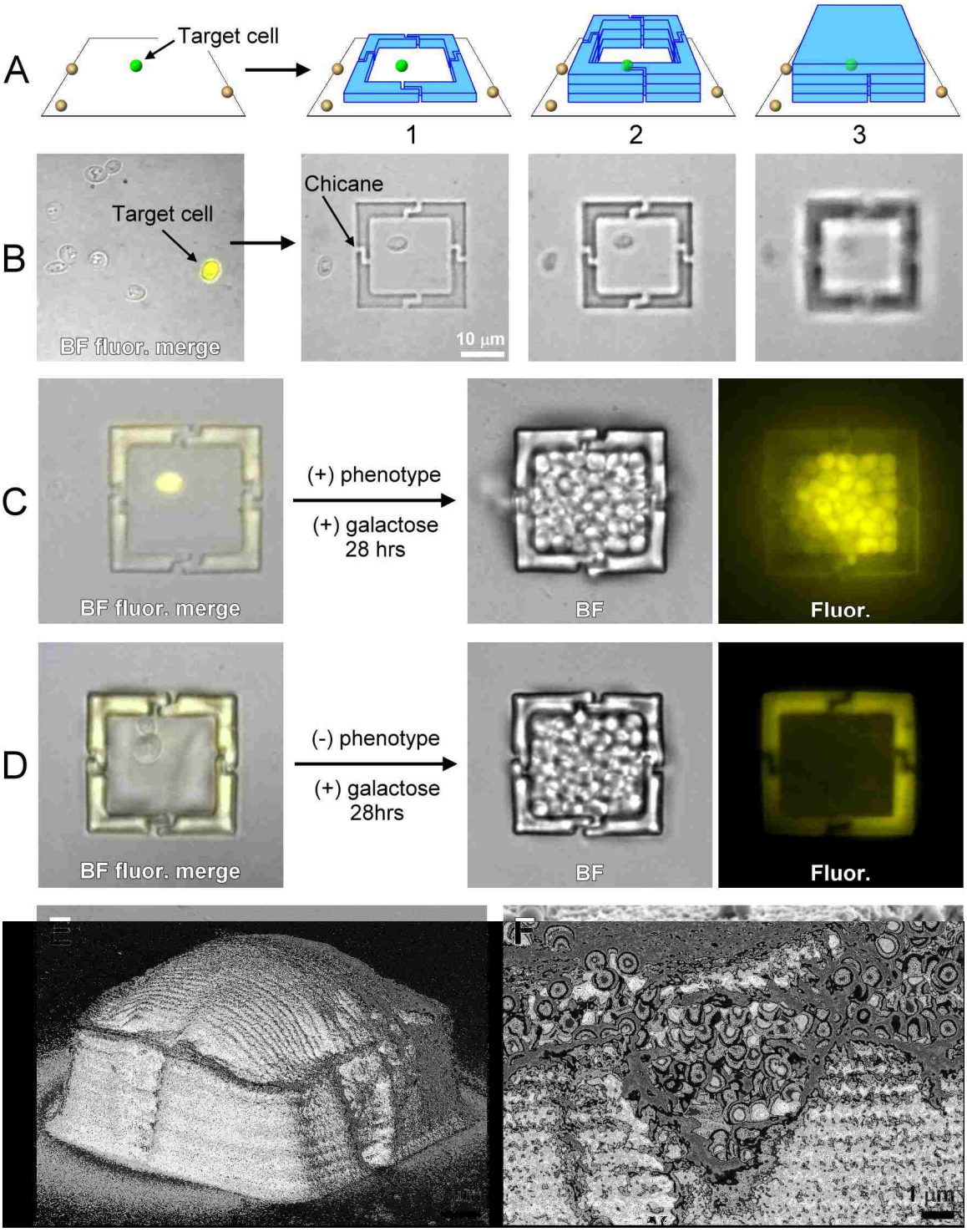

Figure 1. Biocompatible fabrication of 3D protein microstructures allowing physical isolation and confinement of a desired living cell from a population of cells. (A) Simplified schematic of protein hydrogel fabrication isolating desired cell. (B) Isolation of a single *S. cerevisiae* cell expressing YFP from a population of *s. cerevisiae* cells with images following the schematic shown in (A). See the Supplementary Information for a movie of this process. (C) Isolation of a single *S. cerevisiae* cell expressing YFP followed by growth in the presence of inducer, galactose (YP +gal medium). (D) Isolation of a non-fluorescing mother and daughter cell followed by growth in YP +gal. (E) SEM image of a BSA protein structure containing high density *S. cerevisiae* cells. The pressure exerted by the dividing cells resulted in protrusion of the roof into a dome shape. Overall chamber dimensions: 25 × 25 μm in length and width; 10-12 μm in height. (F) SEM image of a BSA protein structure with roof retracted revealing interior with high density *S. aureus* cell population.

Once the target cell was confined, rich media (YP +2% gal.) was introduced to the bath solution and incubated at 30 °C for 28 hours. The isolated cell divided to form a dense clonal population (~2.5×10^{10} cells/mL) packing the protein microchamber (**Fig. 1C**). Under conditions of galactose metabolism (+) phenotype *s. cerevisiae* cells express YFP (see Methods). As shown in the **Fig. 1C**, the majority of progeny cells from the original (+) phenotype cell (**Fig. 1B**) exhibit YFP expression. Some cells, however, show little or no YFP fluorescence indicating that following several generations of growth in non-selective media that the plasmid copy number is reduced, with eventual complete loss of the plasmid. Isolation of a (-) phenotype mother and daughter cell (**Fig. 1D**) followed by incubation in YP +2% gal. at 30 °C for 28 hours also resulted in complete chamber packing of a clonal population that, as expected, exhibited no YFP fluorescence despite the presence of the galactose inducer.

A scanning electron microscopy (SEM) image of a protein structure packed with *s. cerevisiae* cells is shown in **Fig. 1E.** Apparent in this image are ridges in the structure walls associated with the 1 μm z-step employed during fabrication. Incubation and

growth of the entrapped cell(s) to extremely high densities can lead to significant deformation of the protein structure. Expansion of the thinnest and most elastic surface (the microchamber top) into a dome shape is observed (**Fig. 1E**), along with elliptical protrusions from individual *s. cerevisiae* cells.

***In situ* confinement of prokaryotic cells.**

In addition to selection and confinement of non-motile eukaryotic cells, this technique is also compatible with gram-negative and gram-positive bacteria. In **Fig. 1F** the top of a protein structure was retracted during sample preparation for SEM imaging, revealing the interior containing a high density *S. aureus* cell population.

E. coli cells engineered to switch between different states upon exposure to light[21], were confined *in situ* in protein microchambers (**Fig. 2**). These cells express the chimaeric photoreceptor Cph1 from cyanobacteria fused to an intracellular *e. coli* histidine kinase domain, allowing chromatic control of gene expression. The resultant construct yields red fluorescent protein (RFP) expression upon exposure to red light.

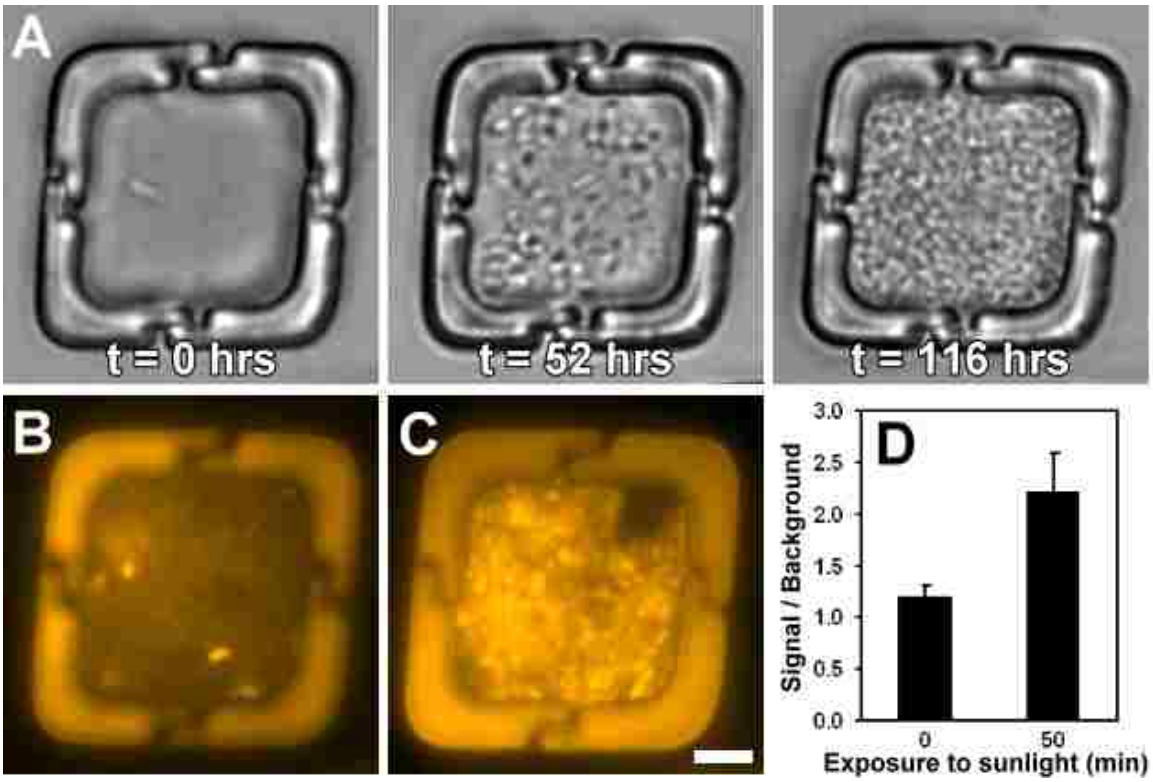

Figure 2. Bright field (A) and epifluorescence (B, C) images of photo responsive *e. coli*[21] following isolation and incubation in BSA protein structures. Image (B) was taken immediately prior to a 50 min exposure to indirect sunlight at 30 °C. Red light exposure initiates RFP expression (image C). (D) Fluorescence signal to background from images (B) and (C). Error bars are one standard deviation of 5-6 measurements within each structure. Scale = 5 μm.

Following *in situ* isolation, media containing heavy selection pressure (4 antibiotics) was introduced to the sample which was then incubated at 37 °C. Growth of a clonal, high density population (~2.5×10^{11} cells/mL) from a single *e. coli* cell is shown in **Fig. 2A**. The observed growth rate in the protein microchambers (t_d = 3.0 hrs) is similar to that observed for these cells under standard culture conditions, and is attributed to the high metabolic load imposed on the cells by the growth medium. Following nearly complete packing of the protein structure, the cells were exposed to indirect sunlight at

30 °C for 50 min. Fluorescence images taken immediately prior to (**Fig. 2B**) and after exposure (**Fig. 3C**) reveal that the cells remain accessible to external photo stimuli and retain the ability to control gene expression *via* photo regulation (**Fig. 2D**).

Impact of isolation, mass transfer, and population density on cell-to-cell signaling

Cell to cell communication amongst, for instance, bacterial cells can provide for coordinated gene expression at the population level. This 'quorum sensing' (QS) derives from the steady production of signaling molecules by individual cells and thus concentration beyond a particular threshold, can indicate a sufficient density of cells to allow for coordinated population behaviors such as virulence. Issues of mass transfer and spatial distribution of cells—which clearly affects signal concentration in 'real world' environments[22]—have proven challenging to address using standard experimental practices.

We explored confinement in protein microchambers on *s. aureus* cells engineered to report (QS). Protein structures typically fabricated throughout this work included chicanes in each of the four walls, providing regions of high diffusivity between the exterior and interior of the structure. To explore the impact of mass transfer on QS behavior, protein microchambers were also fabricated without chicanes resulting in structures with restricted diffusivity.

In *S. aureus*, P3 promotion of the QS-dependent accessory gene regulator *agr* operon RNAIII transcript results in repression of adhesion expression, and upregulation of hemolysins, toxins, degradatory enzymes, and metabolic pathways.[23] To optically monitor the onset of QS, *S. aureus* were engineered to express green fluorescent protein

(GFP) upon *agr* P3 promoter activation. Following confinement of a single *s. aureus* cell in a protein structure without chicanes, rich media (TSB) was introduced to the sample which was then incubated at 37 °C for 40 hours (**Fig. 3A**). Interestingly, no growth was observed over the course of the experiment; however, distinct changes to the cell morphology were observed, as shown by the septum formation following isolation (**Fig. 3A, insets**). Over the 40 hours experiment this single cell also expressed GFP indicating that QS pathways had been initiated.

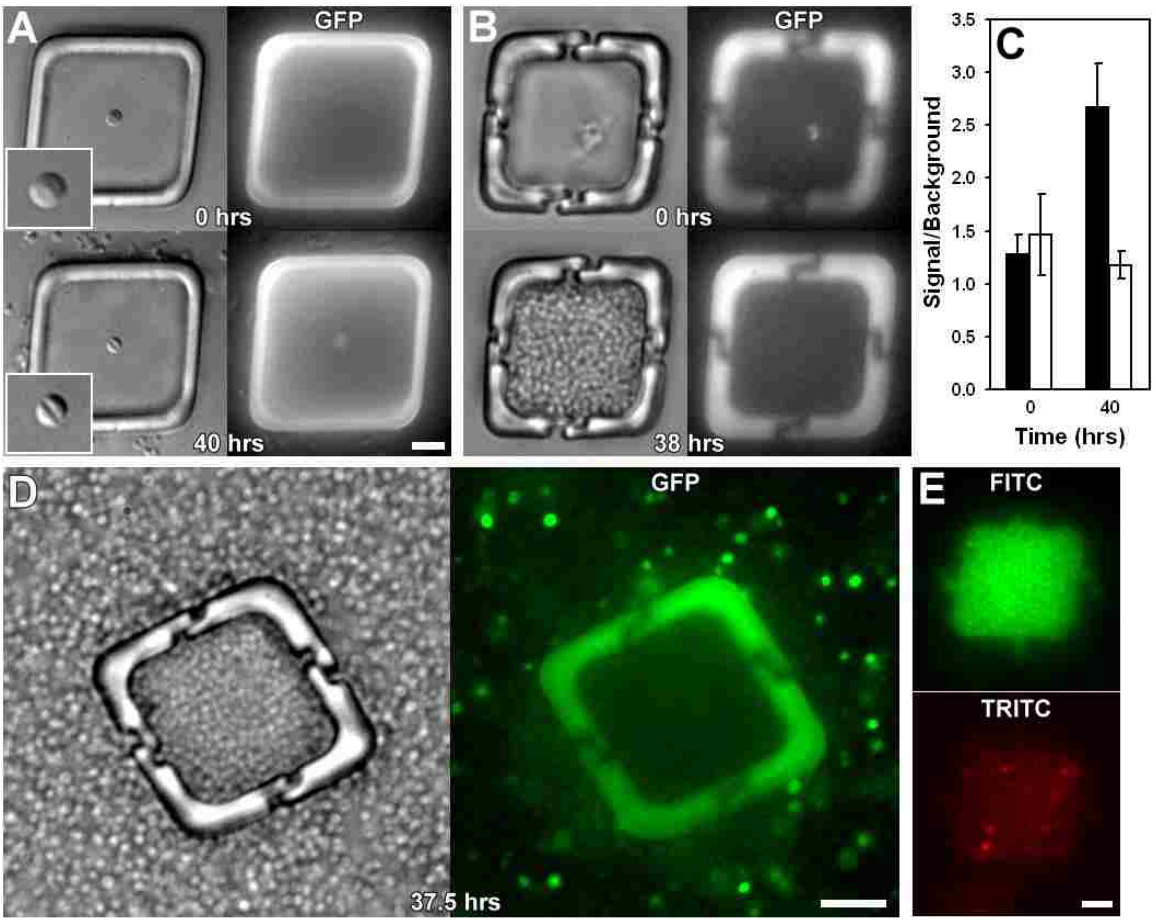

Figure 3. Quorum sensing behavior of *s. aureus* mutant 1743 isolated in protein structures with differing diffusivity properties. Activation of the quorum sensing pathway initiates GFP expression. (A) Images of a single *s. aureus* cell isolated and cultured in a protein structure with low diffusivity exhibiting arrested growth and reporting quorum sensing after 40 hrs. Insets show septum formation during culture. (B) Images of *s. aureus* cells isolated and cultured in a protein structure with high diffusivity resulting in growth to densities much greater than that required for activation of quorum sensing; however, no quorum sensing was reported. (C) Fluorescence signal to background ratio from *s. aureus* entrapped in low diffusivity (black) and high diffusivity (white) protein structures from panels (A) and (B), respectively. Error bars are one standard deviation of 4-6 measurements within each structure. (D) Protein structure 37.5 hrs from culture initiation. These transmission and GFP channel epifluorescence images were collected prior to rinsing and addition of fresh medium in preparation for collecting the 38 hr culture images shown in panel (B). Although at a lower density than *s. aureus* cells within the structure, *s. aureus* cells exterior to the structure report quorum sensing. (E) Epifluorescence images of viability dye assay performed following 48 hr culture. All cells stain green; non-viable cells stain red. Results demonstrate high viability and ready diffusion into and within the packed structure. Scales = 5 μm. Fluorescent images in panels (D) and (E) are false colored.

Protein microchambers with chicanes were also fabricated to isolate *s. aureus* cells, some of which were initially reporting active QS (**Fig. 3B**). In these structures growth proceeded rapidly, and in the case of the sample shown in **Fig. 3B,** a packed structure was observed over the 38 hour incubation. Surprising, even at this extremely high population density (~5.0×10^{11} cells/mL), QS was not observed as indicated by the lack of GFP expression (**Fig. 3C**). Under standard culture conditions, densities of 10^7 – 10^9 *s. aureus* cells/mL are sufficient to initiate QS behavior. This is clearly the case for *s. aureus* cells outside of the protein structure, as shown in **Fig. 3D.** (The image presented in **Fig. 3D** is of the sample structure presented in **Fig. 3B**, but taken approximately 30 minutes prior. Following collection of the images shown in **Fig. 3D**, the sample was rinsed with fresh media and then imaged as shown in **Fig. 3B**.) Although not at the extremely high density observed within the structure, *s. aureus* cells outside the structure report activation of QS pathways. Subsequent assay of packed protein structures with viability dyes indicated that the cells throughout the chamber remain accessible to small molecules (**Fig. 3E, FITC**), and the majority of the cells are viable (**Fig. 3E, TRITC**).

DISCUSSION

Use of MPL to entrap and study bacterial cells within 3D microchambers has been reported[24]. These studies, however, relied on the pre-fabrication of 'flytrap' protein structures, followed by the introduction of motile cells. This results in the eventual random entrapment of cells. The technique we introduce here provides the significantly enabling advantage of first selecting the cell that one desires to study, followed by its

isolation in a well-defined, tunable, biostructure. This advance holds significant implications for single cell and cellular heterogeneity studies. Additionally, we have shown that *in situ* protein microchamber fabrication allowed for the first entrapment of non-motile bacterial cells, and the first isolation of living eukaryotic cells, in microchambers produced by MPL.

Addressable capture and culture of bacterial and yeast cells in devices containing microchambers prepared using soft-lithography[12,16] and other conventional microfabrication techniques[13-15] have been reported. Loading of cells into these devices also relies on random entrapment, preventing isolation of a single target cell from a given population, and often preventing control over the number of cells isolated within a given chamber. Additionally, continuous solution flow to the microchambers through capillaries is required for efficient nutrient and waste exchange.

Advantages of protein MPL for cellular study over these devices include the ability to (i) select and isolate a target cell with desired properties from the heterogeneous population, (ii) rapidly and inexpensively prototype and fabricate new architectures, (iii) incorporate functional components within the protein structure that are chemically responsive[25], (iv) maintain cell cultures in relevant environments (i.e. forced solution flow or support microfluidics/pumps are not required), (v) tune the protein structure physical properties through grey scale control of the fabrication procedure (e.g. increasing/decreasing laser dwell time has allowed for control over the resulting protein structure stiffness/modulus[26]), and (vi) increase or decrease diffusion through the structure[27]. It may also be possible to tune the protein structure properties, possibly allowing for ‘size exclusion’ type filtering of molecules through the chamber walls. Such

control over molecular diffusion through the structure would hold significant opportunities for cell-to-cell signaling and host-pathogen interaction studies.

Our initial cell-to-cell signaling study using *s. aureus* isolated within protein microchambers with differing diffusion properties has shown that subtle changes in the physical properties of the structure can profoundly impact the cellular growth and signaling (**Fig. 3**). As current diffusion-sensing[28] and efficiency-sensing[29] models for QS implicate mass transfer and cell density as governing factors in the initiation of QS, it may be expected that a single cell in a confined structure may self-initiate QS pathways, as we have previous observed in a mesoporous lipid-silica system[30]. Our observation of this same phenomena in a more common culture environment adds credence to that earlier finding.

However, our observation that *s. aureus* cells do not QS when confined within a structure with high diffusivity, with growth to a density 2 – 4 orders of magnitude larger than that typically required for onset of QS, is surprising. These results have been replicated several times, and we can offer no definitive explanation for this observation at this time. We speculate that under these extremely packed conditions, where the majority of a given cell surface is pressed against the surface of other cells and/or the protein structure surface, many surface autoinducing cyclic peptide (AIP) receptors, AgrC, may be blocked. This may prevent docking of a sufficient number of AIP molecules to AgrC to initiate the phosphorylation cascade required to induce RNAIII expression and QS, although AIP is present at high concentrations.

References

1. Leslie, M. The power of one. *Science* **331**, 24–26 (2011).
2. Janes, K.A., Wang, C.-C., Holmberg, K.J., Cabral, K. & Brugge, J.S. Indentifying single-cell molecular programs by stochastic profiling. *Nat. Methods* 7, 311–317 (2010).
3. Chang, H.H., Hemberg, M., Barahona, M., Ingber, D.E. & Huang, S. Transcriptome-wide noise controls lineage choice in mammalian progenitor cells. *Nature* **453**, 544–547 (2008).
4. Elowitz, M.B., Levine, A.J., Siggia, E.D. & Swain, P.S. Stochastic gene expression in a single cell. *Science* **297**, 1183–1186 (2002).
5. De Souza, N. Supplement on single-cell analysis. *Nat. Methods* **8**, 307 (2011).
6. Wernet, M.F. *et al.* Stochastic spineless expression creates the retinal mosaic for color vision. *Nature* **440**, 174–180 (2006).
7. Paszek, P. *et al.* Population robustness arising from cellular heterogeneity. *Proc. Natl. Acad. Sci. USA* **107**, 11644–11649 (2010).
8. Shapiro, H.M. *Practical flow cytometry* 4th edn. (Wiley-Liss, New York, 2003).
9. Emmert-Buck, M.R. *et al.* Laser capture microdissection. *Science* **274**, 998–1001 (1996).
10. Kalisky, T. & Quake, S.R. Single-cell genomics. *Nat. Methods* **8**, 311–314 (2011).
11. Heinemann, M. & Zenobi, R. Single cell metabolomics. *Curr. Opin. Biotechnol.* **22**, 26–31 (2011).
12. Weibel, D.B., DiLuzio, W.R. & Whitesides, G.M. Microfabrication meets microbiology. *Nat. Rev. Microbiol.* **5**, 209–218 (2007).
13. Sims, C.E. & Allbritton, N.L. Analysis of single mammalian cells on-chip. *Lab Chip* **7**, 423–440 (2007).
14. El-Ali, J., Sorger, P.K. & Jensen, K.F. Cells on chips. *Nature* **442**, 403–411 (2006).
15. Khademhosseini, A., Langer, R., Borenstein, J. & Vacanti, J.P. Microscale technologies for tissue engineering and biology. *Proc. Natl. Acad. Sci. USA* **103**, 2480–2487 (2006).
16. Groisman, A. *et al.* A microfluidic chemostat for experiments with bacterial and yeast cells. *Nat. Methods* **2**, 685–689 (2005).
17. Kasko, A.M. & Wong, D.Y. Two-photon lithography in the future of cell-based therapeutics and regenerative medicine: a review of techniques for hydrogel patterning and controlled release. *Future Med. Chem.* **2**, 1669-1680 (2010).
18. Zhang, Y.-L., Chen, Q.-D., Xia, H. & Sun, H.-B. Designable 3D nanofabrication by femtosecond laser direct writing. *Nano Today* **5**, 435–448 (2010).
19. Nielson, R., Kaehr, B. & Shear, J.B. Microreplication and design of biological architectures using dynamic-mask multiphoton lithography. *Small* **5**, 120–125 (2009).
20. Verweij, H. & van Steveninck, J. Model studies on photodynamic cross-linking. *Photochem. Photobiol.* **35**, 265–267 (1982).
21. Tabor, J.J., Levskaya, A. & Voigt, C.A. Multichromatic control of gene expression in *Escherichia coli*. *J. Mol. Biol.* **405**, 315–324 (2011).
22. Horswill, A.R., Stoodley, P., Stewart, P.S. & Parsek, M.R. The effect of the chemical, biological, and physical environment on quorum sensing in structured microbial communities. *Anal. Bioanal. Chem.* **387**, 371-380 (2007).

23. Dunman, P.M. *et al.* Transcription profiling-based identification of *Staphylococcus aureous* genes regulated by the agr and/or sarA loci. *J. Bacteriol.* **183**, 7341-7353 (2001).
24. Kaehr, B. & Shear, J.B. High-throughput design of microfluidics based on directed bacterial motility. *Lab Chip* **9**, 2632-2637 (2009).
25. Kaehr, B. & Shear, J.B. Multiphoton fabrication of chemically responsive protein hydrogels for microactuation. *Proc. Natl. Acad. Sci. USA* **105**, 8850–8854 (2008).
26. Khripin, C.Y., Brinker, C.J. & Kaehr, B. Mechanically tunable multiphoton fabricated protein hydrogels investigated using atomic force microscopy. *Soft Matter* **6**, 2842-2848 (2010).
27. Connell, J.L. *et al.* Probing prokaryotic social behaviors with bacterial "lobster traps". *mBio* **1**, 1–8 (2010).
28. Redfield, R.J. Is quorum sensing a side effect of diffusion sensing? *Trends Microbiol.* **10**, 365–370 (2002).
29. Hense, B. *et al.* Does efficiency sensing unify diffusion and quorum sensing? *Nat. Rev. Microbiol.* **5**, 230–239 (2007).
30. Carnes, E.C. *et al.* Confinement-induced quorum sensing of individual *Staphylococcus aureus* bacteria. *Nat. Chem. Biol.* **6**, 41–45 (2010).

SUPPLEMENTAL METHODS

Materials

Methylene blue (M-4159), glucose (99%), and galactose (99%) were purchased from Sigma-Aldrich (St. Louis, MO). Bovine serum albumin (BSA, BAH64-0100) was supplied by Equitech-Bio (Kerrville, TX). LB and TSB were from Becton Dickinson and Company (Sparks, MD). Yeast extract was obtained from Fischer Scientific (Pittsburgh, PA). Bacto™ Peptone was from BD Biosciences (Franklin Lakes, NJ). *Bac*Light™ SYTO 9®/propidium iodide bacterial viability kit and GIBCO™ phosphate-buffered saline (PBS, 1×, pH 7.4) were purchased from Invitrogen (Carlsbad, CA). Aqueous solutions were prepared with 18 MΩ water using a Barnstead Nanopure water purifier (Boston, MA). All chemicals and were stored according to the supplier's specifications and used without further purification.

Cell strains

S. cerevisiae host strain S288C (*ura− his−*) contained the YFP gene under control of the *GAL1* promoter within the high-copy vector pYES2. Chromaticly responsive *E. coli* was provided by the Tabor Lab (Department of Bioengineering, Rice University, Huston, TX). *S. aureus* ALC1743 (*agr* group 1 RN6390 containing reporter *agr*: P3-gfp) was provided by the Cheung Lab (Department of Microbiology, Dartmouth Medical School, Hanover, NH).

In situ protein microchamber fabrication

Microchambers composed of photo-crosslinked protein were fabricated in the presence of living cells (from overnight culture) that were re-suspended in 0.5× PBS (pH 7.4) solutions containing BSA protein at 285 mg/mL, and methylene blue (6 mM) as a photosensitizer. This solution was then introduced onto an untreated no. 1 microscope cover slip onto which the protein structure was fabricated.

Microstructure geometries were defined using a dynamic mask-directed multiphoton lithography technique.[19] The output of a mode-locked titanium:sapphire laser (Tsunami, Spectra Physics, Mountain View, CA) operating at 750 nm, pulse width of 60 fs, and a repetition rate of 80 MHz, was raster scanned with an X/Y open frame scan head (Nutfield Technology, Hudson, NH) across a digital micromirror device (DMD, Texas Instruments, 0.55SVGA) within a partially dismantled business projector (Benq, MP510). The reflective surface of the DMD was an 848 × 600 array of 16 mm × 16 mm aluminum mirrors that could be switched individually between “on” and “off” states via rotation through a ±10° angle. Individual mirrors were controlled by the projector electronics, taking instructions from the graphics output of a personal computer. Focused laser light that scanned over approximately the central quarter of the DMD array was reflected into a beam block or directed further down the optical path according to the on/off state of the individual mirrors.

The laser output was adjusted by using optics to approximately fill the back aperture of an oil-immersion objective (Nikon 100× Fluar, 1.3 numerical aperture) situated on a Nikon inverted microscope. Laser power, obtained by attenuating the laser beam using a halfwave plate/polarizing beam-splitter pair, was approximately 30 mW at

the objective. Laser dwell time during fabrication was set by the frequency of the X-component (0.1 Hz) and Y-component (180 Hz) of the raster scan. This output defined the features of protein microstructures in the X/Y plane. Stepping the laser focus axially from the substrate (Z plane, 1 μm steps) using a motorized focus driver (Prior, H122) while changing the image on the DMD reflectance mask permitted fabrication of complex 3D protein structures.

Cell incubation in BSA microchambers

Following *in situ* microchamber fabrication the cover slip substrate was rinsed 3 times with 1 mL of 1× PBS, pH 7.4. The protein structures are very robust and adhere tightly to the glass substrate, withstanding even extremely vigorous washing. Following rinsing, the substrate was incubated in a 1 mL dish containing the appropriate culture medium at 30-32 °C (*S. cerevisiae*) or 37 °C (*E. coli* and *S. aureus*). The media was replaced every 24 hours with the exception of some *S. aureus* samples which were allowed to incubate for up to 72 hours for QS studies.

Fluorescence microscopy

Wide-field fluorescence imaging was performed on the Nikon inverted microscope which was equipped with a mercury-arc lamp and standard FITC and TRITC filter sets (Chroma, Rockingham, VT). Fluorescence emission was collected using the Fluar 100× objective and detected using a 12-bit 1392 x 1040 element CCD (Cool Snap HQ; Photometrics, Tucson, AZ). Data were processed using Image J image-analysis software.

Scanning electron microscopy (SEM)

Protein microstructures containing cells were fixed in 2.5% glutaraldehyde solution (Sigma) overnight at 4 °C, and dehydrated using 10 min sequential washes in: 3:1 H_2O/ethanol; 1:1 H_2O/ethanol; 1:3 H_2O/ethanol; twice in 100% ethanol; 1:1 ethanol/methanol; twice in 100% methanol (vol/vol). The sample was then allowed to air dry over several hours and sputter-coated with Au to a nominal thickness of 10 nm. SEM imaging was performed on a FEI Quanta series (**Fig. 1E**) or a JEOL 6701F (**Fig. 1F**) scanning electron microscope operating at 5kV.

Biocompatible microfabrication for targeted confinement of single cells and their progeny

Jason C. Harper, Susan M. Brozik, C. Jeffrey Brinker, & Bryan Kaehr

Supplementary figures and text:

Supplementary Note 1	**Optimization of MPL Conditions for Living Cell Isolation**
Supplementary Figure 1	**Viability of *S. cerevisiae*, *S. aureus*, and *E. coli* cells *vs.* Methylene Blue Concentration in BSA Solution**
Supplementary Movie 1	**Isolation of a single *S. cerevisiae* cell expressing YFP from a population of *s. cerevisiae* cells**

Supplementary Note 1 | Optimization of MPL Conditions for Living Cell Isolation

Conditions of MPL that were optimized allowing *in situ* cell isolation included photosensitizer and protein monomer concentrations, as well as laser power and dwell time. Methylene blue (MB), a redox active molecule which has been used as a viability indicator dye[31] and an electron mediator in cell cultures,[32] was chosen as photosensitizer due to its low cytotoxicty and high two-photon action cross-section at more biocompatible IR wavelengths (~740-800 nm). High purity bovine serum albumin (BSA) protein was selected as protein monomer due to its oxygen radical scavenger functionality.[33] The viability of *S. cerevisiae*, *S. aureus*, and *E. coli* cells incubated for 60 minutes at room temperature in BSA solutions with differing MB concentrations is presented in **Supplementary Figure 1**. All cells showed a slight decrease in viability with increasing MB concentration with *S. cerevisiae* (blue trace) and *S. aureus* (green trace) exhibiting a greater reduction in viability for MB concentrations 4 mM and greater. This trend was not a strong with *E. coli* cells (red trace).

To minimize the effects of exposure to the photosensizer, while allowing for low laser power and dwell time (data not shown), a concentration of 6 mM MB was chosen and exposure of cells to this solution was limited to 20 minutes or less. A concentration of 285 mg/mL BSA in the fabrication solution was selected based on solubility limit, high concentration for increased oxygen radical scavenging activity, the laser power and dwell time required to produce a well resolved structure, and cell tolerance to high BSA concentration. Under these conditions protein structures could be produced in very intimate proximity to living cells without significant loss of viability (measured as

reproductive capacity). However, direct exposure of cells to the rastering 2-photon beam often resulted in cell rupture.

REFERENCES

31. Austin, G.A., Watson, R.W.J. & D'Amore, T. Studies of on-line viable yeast biomass with a capacitance biomass monitor. *Biotechnol. Bioeng.* 43, 337–341 (1994).
32. Ganguli, R. & Dunn, B.S. Kinetics of anode reactions for a yeast-catalyzed microbial fuel cell. *Fuel Cells* 9, 44–52 (2009).
33. Dumoulin, M.J., Chahine, R., Atanasiu, R., Nadeaum, R. & Mateescu, M.A. Comparative antioxidant and cardioprotective effects of ceruloplasmin, superoxide dismutase and albumin. *Arzneimittel-Forsch.* 46, 855–861 (1996).

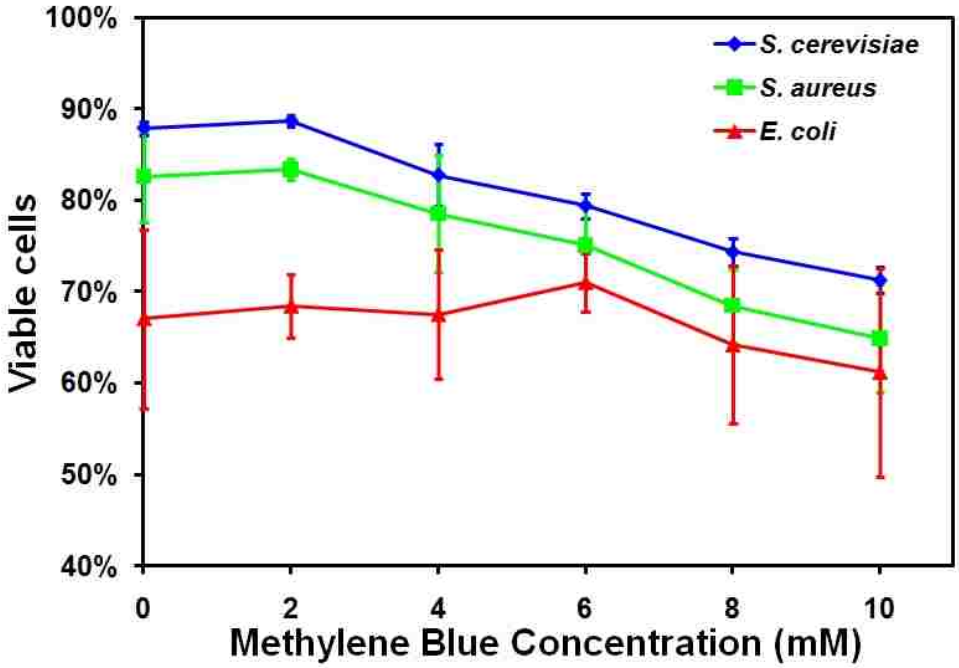

Supplementary Figure 1. | Viability of *S. cerevisiae*, *S. aureus*, and *E. coli* cells *vs.* Methylene Blue Concentration in BSA Solution

Viability of *S. cerevisiae*, *S. aureus*, and *E. coli* cells (measured by viability dyes) following a 60 min incubation at room temperature in 0, 2, 4, 6, 8, or 10 mM methylene blue with 200 mg/mL BSA, 0.5× PBS, pH 7.4. Error bars are one standard deviation of 3 measurements from each sample.

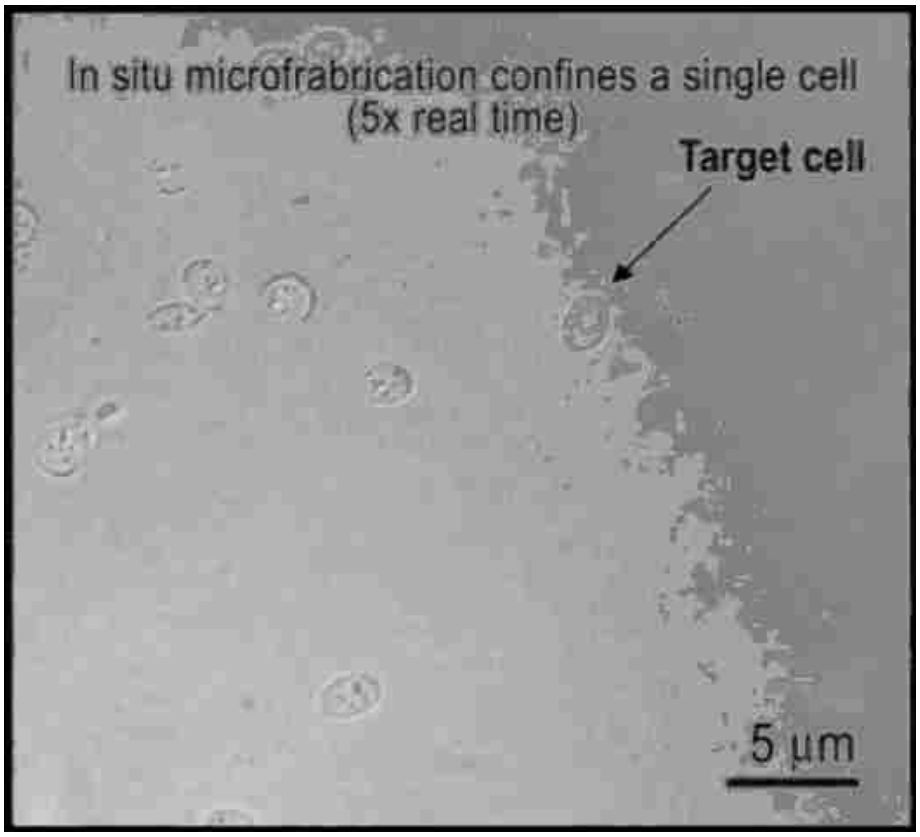

Supplementary Movie 1. | Isolation of a single *S. cerevisiae* cell expressing YFP from a population of *s. cerevisiae* cells

Movie of the selection and isolation of the *S. cerevisiae* cell expressing YFP shown in **Fig. 1B** and **Fig. 1C**, from a population of *s. cerevisiae* cells not expressing YFP. Fabrication solution: 285 mg/mL BSA, 6 mM MB, 0.5× PBS, pH 7.4. Movie speed: 5× real time.

SUMMARY AND FUTURE OUTLOOK

In summary, described herein are new techniques and new fundamental understanding that has allowed for the integration of bio with nano in unique and enabling ways, and the manipulation of cellular behavior at the individual cell level.

This work elucidated the mechanistic understanding of the biochemical and nanomaterial processes that govern cell directed assembly and integration. The mechanism responsible for introducing functional foreign membrane-bound proteins *via* proteoliposome addition to the silica-lipid-cell matrix was also determined. This new understanding was leveraged to extend 3D cellular immobilization capabilities using sol-gel matrices endowed with glycerol, trehalose, and media components. The effects of these additives and the effect of encapsulated cell metabolic activity on viability and gene expression were carefully studied. These results provided important insights towards design and development of effective cell-based biosensors. This enabled entrapment of prokaryote and eukaryote cells within a novel microfluidic platform capable of simultaneous colorimetric, fluorescent, and electrochemical detection of a single analyte, significantly improving confidence in the biosensor output. Finally, the selection and *in situ* isolation of a single target cell from a population of cells with mixed phenotypes, and the subsequent monitoring of its behavior, and that of its progeny, under well defined conditions, was demonstrating for the first time using biocompatible multiphoton lithographic fabrication of protein microstructures. This valuable new tool opens intriguing opportunities for studying single cell behaviors under well-defined conditions.

These integrated cellular systems have significant implications towards development of bioelectronics, photonics, microfluidics, smart prosthetics, advanced physiological sensors, portable medical diagnostic devices, platforms for fundamental cell studies, and the development of practical and robust devices that can sense the presence of harmful agents in real-time.

The initial motivation for this work was the need to stabilize the CANARY cell line beyond its current 2 day limit. This would permit the use of this mammalian b-cell based biosensor in less developed and stable regions, allowing detection of harmful agents in real-time, providing full situational awareness to the warfighter. We now have promising preliminary results from mammalian cell lines encapsulated in sol-gel matrices developed and studied over the course of this work. Cell lines encapsulated in silica matrices showing promising viability include bovine pulmonary artery endothelial cells, macrophage cells from mouse, and erythrophore cells from fish. Importantly, erythrophore cells encapsulated in sol-gel thin films within plastic laminate cartridges developed in this work remained viable and responsive to stimuli several days post encapsulation. This work, in collaboration with Luna Innovations, provides a basis to now purse encapsulation of CANARY cells. Interest in this pursuit was expressed by a member of the CANARY team at Lincoln Laboratories. The program manager at DTRA that oversaw and funded this work has also expressed a desire to continue funding this effort, specifically extending the project towards the stabilization of CANARY. This is one example of several exciting opportunities that have arisen from this study. Therefore, the future outlook and potential impact of this work is bright.